



THE HONG KONG  
POLYTECHNIC UNIVERSITY

香港理工大學

Pao Yue-kong Library

包玉剛圖書館

---

## Copyright Undertaking

This thesis is protected by copyright, with all rights reserved.

**By reading and using the thesis, the reader understands and agrees to the following terms:**

1. The reader will abide by the rules and legal ordinances governing copyright regarding the use of the thesis.
2. The reader will use the thesis for the purpose of research or private study only and not for distribution or further reproduction or any other purpose.
3. The reader agrees to indemnify and hold the University harmless from and against any loss, damage, cost, liability or expenses arising from copyright infringement or unauthorized usage.

If you have reasons to believe that any materials in this thesis are deemed not suitable to be distributed in this form, or a copyright owner having difficulty with the material being included in our database, please contact [lbsys@polyu.edu.hk](mailto:lbsys@polyu.edu.hk) providing details. The Library will look into your claim and consider taking remedial action upon receipt of the written requests.

**The Hong Kong Polytechnic University**  
Department of Electronic and Information Engineering

**Spin-Lattice Coupling in Molecular  
Dynamics Simulation of  
Ferromagnetic Iron**

by  
MA, Pui Wai

A thesis submitted in partial fulfilment of the requirements for  
the degree of Doctor of Philosophy

December 2007

## **CERTIFICATE OF ORIGINALITY**

I hereby declare that this thesis is my own work and that, to the best of my knowledge and belief, it reproduces no material previously published or written, nor material that has been accepted for the award of any other degree or diploma, except where due acknowledgement has been made in the text.

\_\_\_\_\_ (Signed)

MA, Pui Wai  
\_\_\_\_\_ (Name of student)

Dedicate to my parents

## Abstract

A model for magnetic iron where atoms are treated as classical particles with intrinsic spins is developed. The atoms interact *via* scalar many-body forces as well as *via* spin-dependent forces of the Heisenberg form. The coupling between the lattice and spin degrees of freedom is described by a coordinate-dependent exchange function, where the spin-orientation-dependent forces are proportional to the gradient of this function. A spin-lattice dynamics simulation approach extends the existing magnetic-potential treatment to the case where the strength of interaction between the atoms depends on the relative non-collinear orientations of their spins. An algorithm for integrating the linked spin-coordinate equations of motion is based on the 2<sup>nd</sup> order Suzuki-Trotter decomposition for the non-commuting evolution operators for both coordinates and spins. The notions of the spin thermostat and the spin temperature are introduced through the combined application of the Langevin spin dynamics and the fluctuation-dissipation theorem. We investigate several applications of the method, performing microcanonical ensemble simulations of adiabatic spin-lattice relaxation of periodic arrays of 180° domain-walls, and isothermal-isobaric ensemble dynamical simulations of thermally equilibrated homogeneous systems at various temperatures. The isothermal magnetization curve evaluated using the spin-lattice dynamics algorithm is well described by the mean-field approximation and agrees satisfactorily with the experimental data for a broad range of temperatures. The equilibrium time-correlation functions of spin orientations exhibit the presence of short-range magnetic order above the Curie temperature. Short-range order spin fluctuations

are shown to contribute to the thermal expansion of the material. Simulations on thermal expansion and elastic response of bulk bcc iron, and magnetization in bcc iron thin films are also performed and the results discussed. Our analysis illustrates the significant part played by the spin directional degrees of freedom in the dynamics of atomic motion in magnetic iron and iron-based alloys, and shows that the spin-lattice dynamics algorithm provides a viable way of performing realistic large-scale dynamical simulations of magnetic materials.

## **Publications arising from the thesis**

- [1] “Large-scale molecular dynamics simulation of magnetic properties of amorphous iron under pressure”, P. W. Ma, W. C. Liu, C. H. Woo and S. L. Dudarev, *J. App. Phys.*, **101**, 073908 (2007)
- [2] “Spin-lattice Dynamics Simulations of Ferromagnetic Iron”, P. W. Ma, C. H. Woo and S. L. Dudarev, in “*Proceedings of International Conference on Electron Microscopy and Multiscale Modeling (EMMM-2007)*” edited by A. S. Avilov, S. L. Dudarev and L. D. Marks. (AIP, New York, 2008)
- [3] “Large-scale simulation of the spin-lattice dynamics in ferromagnetic iron”, P. W. Ma, C. H. Woo and S. L. Dudarev, *Phys. Rev. B*, **78**, 024434 (2008)

## **Acknowledgements**

I felt an immense gratitude to my Chief Supervisor, Prof. C. H. Woo. Under his patient guidance, many suggestions and encouragements were given. His helps and advices are crucial for the completion of this thesis. Throughout these three years, he taught me many things which do not only relate to academics, but also moral. He lets me know how to behave as a good one by his own conduct.

I am also indebted to Dr. S. L. Dudarev. He is always with me to go across all the milestones. Discussions with him are inspiring. The chance of cooperating with him and visiting the Culham Science Center makes me open my eyes and understand my insufficient.

Thanks must also be given to Dr. Yue Zheng, Dr. Averil Liu and Dr. Yun Zhu. Their helps and suggestions are also significant to my works. They are good companions, especially when I am frustrated.

# Table of contents

CERTIFICATE OF ORIGINALITY .....	i
Abstract .....	iii
Publications arising from the thesis .....	v
Acknowledgements .....	vi
Table of contents .....	vii
List of figures .....	x
Chapter 1: Introduction .....	1
1.1 Motivations .....	1
1.2 Origin of Atomic Spins .....	2
1.3 DFT Spin Dynamics .....	5
1.4 DFT Spin-Lattice Coupling .....	7
1.5 Classical Spin Dynamics .....	9
1.6 MD for Magnetic Materials .....	12
1.7 Spin-Lattice Dynamics Simulation .....	15
1.8 Validation and Applications .....	17
Chapter 2: Molecular Dynamics .....	23
2.1 Background and History .....	23
2.2 Equations of Motion .....	25
2.3 Solution of the equation of motion: Integration Algorithms .....	27
2.4 Periodic Boundary Condition .....	30
2.5 Temperature Control .....	32
2.6 Applied Stresses .....	34

2.7	Magnetic Potential .....	38
Chapter 3:	Amorphous Iron at $T = 0\text{K}$ .....	44
3.1	Brief Introduction.....	44
3.2	Simulation Scheme .....	47
3.3	Topological Structure .....	48
3.4	Magnetic/non-magnetic Transition .....	52
3.5	Relationship between Local Structure and Magnetic Moment .....	57
3.6	Brief Conclusion .....	63
Chapter 4:	Spin-Lattice Dynamics.....	68
4.1	Brief Introduction.....	68
4.2	Hamiltonian.....	70
4.3	Exchange Function.....	73
4.4	Equations of Motion.....	75
4.5	Conservation Laws.....	78
4.6	Spin Temperature .....	81
4.7	Integration Algorithm.....	84
4.8	Brief Conclusion .....	91
Chapter 5:	Parallel Algorithms for Suzuki-Trotter Decomposition.....	95
5.1	Brief Introduction.....	95
5.2	Current Parallel Algorithms .....	96
5.3	Grouping Independent Atoms .....	98
5.4	Integrity of the Algorithm .....	101
5.5	Efficiency .....	102
5.6	Stability .....	107

5.7	Brief Conclusion .....	108
Chapter 6:	Equilibration Processes in a Microcanonical Ensemble .....	111
6.1	Brief Introduction.....	111
6.2	Equilibration Process – Part I (from Spin to Lattice).....	114
6.3	Equilibration Process – Part II (from Lattice to Spin) .....	129
6.4	Size Effects of the Simulation Box .....	132
6.5	Brief Conclusion .....	135
Chapter 7:	Spin Thermalization and Related Effects.....	139
7.1	Brief Introduction.....	139
7.2	Temperature-Dependent Spontaneous Magnetization .....	141
7.3	Correlation functions.....	148
7.4	Magnetization in Fe Thin Films .....	151
7.5	Magnetic Effects on Elastic Constants.....	155
7.6	Brief Conclusion .....	159
Chapter 8:	Summary and Conclusion .....	163

## List of figures

Figure 1.1 – The electron configuration of an individual iron atom containing seven d-electrons, according to Hund’s rule .....	3
Figure 1.2 – Density of states plot illustrating the occupation of the majority and minority 3d-bands in the ferromagnetic configurations of the bcc $\alpha$ -iron. (Reprinted from Ref. [7] with the premission from authors.) .....	4
Figure 1.3 – Schematic representation of a spin wave.....	5
Figure 1.4 – Schematic representation of the magnetization precession with damping, according to Gilbert equation.....	11
Figure 2.1 – Schematic picture of a 2-dimension periodic system .....	31
Figure 2.2 – Schematic picture to mismatch the boundary across the simulation box and its images.....	37
Figure 3.1 – Radial distribution function (RDF) $g(r)$ of amorphous iron with density = 7.88 g/cm <sup>3</sup> (a) at T = 0K and no. of atoms = 288 & no. of atoms = 16126. The blue bars represent the RDF of the corresponding perfect bcc lattice up to fifth nearest neighbors, with the density of first nearest neighbor normalized to one. (b) at T = 300K and no. of atoms = 16126 & experimental data from T. Ichikawa. ....	49
Figure 3.2 – Radial distribution function (RDF) $g(r)$ of amorphous iron at different densities. (a) 2 Å < r < 10 Å (b) 2.15 Å < r < 2.31 Å (c) 2.3 Å < r < 3.3 Å (d) 3.0 Å < r < 6.0 Å.....	50
Figure 3.3 – Percentage of atoms for various densities with at least one neighbor with a separation of less than 2.31 Å. ....	52

- Figure 3.4 – (a) Atomic configuration and magnetic moments for the 110 dumbbell configuration in bcc iron calculated using density functional theory and (b) the same configuration modeled using the magnetic interatomic potential. The differences between (a) and (b) are associated with the approximate treatment of interatomic forces and magnetic moments within the magnetic interatomic potential formalism. .... 53
- Figure 3.5 – (a) Magnetic moment density versus magnetic moment at different densities. (b) Percentage of nonmagnetic atoms versus density. .... 54
- Figure 3.6 – The mean (a) and standard deviation (b) of magnetic moment versus the number density including/excluding atoms with magnetic moment equals to zero. .... 55
- Figure 3.7 – (a) Magnetic moment versus Voronoi volume at different densities. (b) The magnetic moment fitted as a function of the Voronoi volume. The blue line represents fitting to all atoms and the red line represents fitting without the nonmagnetic atoms. .... 56
- Figure 3.8 – The mean of magnetic moment vs. number of neighbors for (a)  $r_{ij} < 3.21 \text{ \AA}$  (b)  $r_{ij} < 2.31 \text{ \AA}$  (c)  $2.31 \text{ \AA} < r_{ij} < 3.21 \text{ \AA}$  ..... 58
- Figure 3.9 – Average Voronoi volume vs. number of neighbors (a)  $r_{ij} < 3.21 \text{ \AA}$  (b)  $r_{ij} < 2.31 \text{ \AA}$  (c)  $2.31 \text{ \AA} < r_{ij} < 3.21 \text{ \AA}$  ..... 59
- Figure 3.10 – (a) The distribution of number of nearest neighbors at different densities. (b) The mean of the number of neighbors versus density. Red line is the linear fitting. .... 60
- Figure 3.11 – (a) The local magnetic moment versus the local fluctuation of the interatomic separations at different density; the yellow dot is the mean of

magnetic moment versus the average fluctuations of interatomic separations

$$\Delta^{1/2} = \left\langle (\delta R)^2 \right\rangle^{1/2} / \langle R \rangle$$

(b) The average fluctuations of interatomic distance

versus the number densities. .... 61

Figure 3.12 – Atomic structures and magnetic moments of atoms simulated using the magnetic potential for systems containing approximately 16 thousand atoms for different values of mass density. Darker color represents atoms with lower magnetic moments. The figure illustrates the gradual nature of the magnetic/non-magnetic transition occurring in amorphous iron under increased external pressure. .... 62

Figure 4.1 – Exchange function  $J_{ij}$  shown as a function of interatomic distance  $r_{ij}$  and compared with data taken from Ref. [16] and Ref. [17]. The assumed form for the exchange function is  $J_{ij}(r_{ij}) = J_0 (1 - r_{ij}/r_c)^3 \Theta(r_c - r_{ij})$ , where  $J_0 = 904.90177\text{meV}$  and  $r_c = 3.75 \text{ \AA}$ . .... 74

Figure 5.1 – Schematic picture of 1D spin chain containing 10 spins, where the Suzuki-Trotter decomposition is (top) sequential; (bottom) parallelized ..... 97

Figure 5.2 – A 2D system that is cut into 25 link-cells with periodic boundary condition. All the cells are allocated into group A to group H. .... 99

Figure 5.3 – The actual run-time of spin only system (top) versus number of threads with 16000, 54000, 128000, 250000 and 1024000 spins; (bottom left) versus number of spins with threads from 1 to 4; (bottom right) versus number of spins with threads from 5 to 8. .... 104

Figure 5.4 – The efficiency of spin only system (left) versus number of threads with 16000, 54000, 128000, 250000 and 1024000 spins; (right) versus number

of spins with threads from 1 to 8.....	104
Figure 5.5 – The actual run-time of spin-lattice system (top) versus number of threads with 16000, 54000, 128000, 250000 and 1024000 spins; (bottom left) versus number of spins with threads from 1 to 4; (bottom right) versus number of spins with threads from 5 to 8.....	105
Figure 5.6 – The efficiency of spin and lattice coupled system (left) versus number of threads with 16000, 54000, 128000, 250000 and 1024000 spins; (bottom) versus number of spins with threads from 1 to 8 .....	105
Figure 5.7 – The total energy per atom versus time for a microcanonical ensemble simulation of the dynamical relaxation of a 180° domain wall. Two algorithms, the $(S, F, P, F, S)$ and the $(S, P, F, P, S)$ , in both of which the parallel algorithm for STD is incorporated, are compared. The $(S, P, F, P, S)$ algorithms is found to be ~60% faster than the $(S, F, P, F, S)$ algorithm .....	107
Figure 6.1 – Schematic picture of the unrelaxed 180° domain wall system. All the spins in the left-hand side of the simulation cell ( $0 < x < 15a$ ) pointed upwards whereas the spins in the right hand side of the cell ( $15a < x < 30a$ ) pointed downwards. ....	115
Figure 6.2 – Projections of the unit vectors of atomic spins corresponding to the microcanonical ensemble simulation of the dynamical relaxation of a 180° domain wall system.....	120
Figure 6.3 – The collinearity $\xi_c$ of y-z planes at the $n^{\text{th}}$ lattice plane along the x direction as a function of time in logarithmic scale. ....	121
Figure 6.4 – Magnetic structure for various times after spin-spin relaxation. Each dot represents the direction of the unit vectors of atomic spins averaged over	

- the  $n^{\text{th}}$  lattice plane parallel to the initial sharp domain boundary. The projections of the unit vectors in the three Cartesian directions are also shown. The unfilled circles denoted the first and the last planes. The dark green arrows represent the increase of plane index along x direction. .... 123
- Figure 6.5 – The x-components of the deviations of atomic positions (i.e.  $\Delta x$ ) from their corresponding perfect lattice points along the x direction in the 10fs timescale..... 125
- Figure 6.6 – Time evolution of the kinetic, potential and the spin energy contributions determined in simulations of dynamical relaxation of a sharp  $180^\circ$  domain wall and shown in the (a) 0.1 ps, (b) 10 ps and (c) 1ns timescale. Figure (d) is the same as (c) but the x-axis is in  $\log_{10}$  scale. The velocities of all the atoms were initialized to zero at  $t=0$ . The curves show the variation of energy contributions with respect to their initial values. K.E. and L.E. respectively refer to the kinetic and the scalar (lattice) part of the potential energy defined by equation 4.5, whereas the spin energy S.E. refers to the Heisenberg spin-spin interaction energy (last term in equation 4.5). The sum of the lattice and the spin energies equals the total energy of the system..... 126
- Figure 6.7 – The phase trajectory of an atom (left) and the spin direction (right) in a 54000 atom microcanonical simulation, thermally equilibrated at  $T = 300\text{K}$ . .... 128
- Figure 6.8 – After the relaxation of the  $180^\circ$  domain wall system, the kinetic energy of the atoms is rescaled to 300K instantaneously. The time evolution of the kinetic (K.E.) and potential energies (L.E.) of the lattice and the spin energy (S.E.) are shown in (a) & (b) in timescales of 1 ps, and in (c) of 1ns,

respectively. (b) is the same as (a) but with the y-scale enlarged about 40 times to show the details of the K.E. and L.E. and the energy equipartition. The curves show the variation of various energy components with respect to their initial values..... 130

Figure 6.9 – (a) The time evolution of the kinetic + potential (scalar) and the spin energy terms are shown in 1ns timescale, where the kinetic energy is rescaled to 100K, 300K or 600K instantaneously after the relaxation of the 180° domain wall. The curves show the variation of energy terms with respect to their initial values. (b) The relationship between the half-life of the spin-lattice relaxation and the inverse of temperature. The half-life is obtained by fitting the curve of S.E. by the Boltzmann function that produces a sigmoidal curve.  $T_{\text{initial}} = 28\text{K}$  and  $T_{\text{final}} = 100\text{K}, 300\text{K}$  or  $600\text{K}$ . The grey line is the linear least square fit to the data with the y-intercept at 0.245ns. (c) the one that rescaled to 600K is shown as an example, where the red curve is the fitting line..... 132

Figure 6.10 – (a) Time evolution of the spin energy terms determined in simulations of dynamical relaxation of a 180° domain wall with the edge length of the simulation box being 16a, 20a and 30a. The curves show the variation of spin energy with respect to their equilibrium values. The (b) is the same as (a), but the x-axis is in linear scale and y-axis is in log scale. Those red lines are linear least square fit to the middle part of the curves. (c) The relationship between the volume of the simulation boxes and the half-lives, where the half-lives are the inverse of the slope of those red lines. The grey line is the linear least square fit to the data points with the y-intercept at 0.355ns. .... 134

- Figure 7.1 – Examples of dynamical simulations performed using the Langevin SLD algorithm for  $\eta = 10^{-3}$  for several temperatures of the thermostat..... 143
- Figure 7.2 – Examples of Langevin SLD simulation of thermal relaxation at T = 300K of the spin subsystem interacting with the thermostat, performed for two different values of the damping constant. .... 144
- Figure 7.3 – (a) Logarithm of the collinearity minus the minimum value of the curve as a function of time at 500K and 1300K. The red straight lines are linear least square fit to the flat part of the curves, where their slopes are approximately the negative of the inverse of the thermalization half-life times. (b) The thermalization half-life was presented as a function of temperature. The red line is a Lorentzian peak function fitted to data for the purpose of eyes guiding only. .... 145
- Figure 7.4 – The equilibrium magnetization curve showing the average atomic spin evaluated dynamically using canonical ensemble simulations for various temperatures. Experimental data were taken from Ref. [17] and the mean field approximation curve was evaluated using the method described in text. .... 146
- Figure 7.5 – The spin-spin spatial correlation functions shown as functions of absolute temperature for the 1<sup>st</sup>, 2<sup>nd</sup> ... 12<sup>th</sup> nearest neighbour atoms. .... 149
- Figure 7.6 – The time-dependent spin-spin on-site autocorrelation functions evaluated dynamically using microcanonical ensemble simulations performed for fully thermalized initial configurations. .... 150
- Figure 7.7 – The spin autocorrelation dephasing times for the curves shown in Figure 7.6. .... 151
- Figure 7.8 – The average of the magnitude of magnetic moment calculated

layer-by-layer for various temperatures and for (100), (110) and (111) surfaces.  
..... 152

Figure 7.9 – The collinearity calculated layer-by-layer for various temperature and  
for (100), (110) and (111) surfaces. .... 153

Figure 7.10 – The average of magnetic moment calculated layer-by-layer for  
various temperature and for (100), (110) and (111) surfaces..... 154

Figure 7.11 – Equilibrium zero pressure lattice constant of bcc iron evaluated using  
SLD simulations, conventional MD simulations performed for the Ackland  
potential [21], the magnetic DD potential [20], and experimental data taken  
from Nix and MacNair [22] shown for a range of temperatures..... 156

Figure 7.12 – Elastic constant of bcc iron evaluated using SLD simulations,  
conventional MD simulations performed for the Ackland potential [21], the  
magnetic DD potential [20], and experimental data taken from Dever [16]  
shown for a range of temperatures. .... 158

# Chapter 1: Introduction

## 1.1 Motivations

Magnetic materials are playing increasingly important roles in engineering developments of the 21<sup>st</sup> century. Applications involving materials properties governed by the magnetic nature of electron spin are quickly becoming an essential ingredient in the more advanced technologies in many important areas of engineering. These applications range from the direct exploitation of the spin degree of freedom of the electron in the storage, recovery, transportation, manipulation and processing of information, to quantum computing, to issues arising from the magnetic nature of the irradiation damage-resistant ferritic-martensitic steels, a prime candidate material for the structures of both advanced fission and fusion reactors.

In the field of advanced fission and fusion materials, modeling the dynamical processes occurring in steels at high temperature or/and under irradiation is one of the major mathematical challenges. Steels are very unusual systems in that their properties are determined by the magnetism of iron and solute (e.g. chromium or nickel) atoms or, in other words, by the effects of electron exchange and correlations. Probably the most convincing argument confirming the pivotal role played by the exchange and correlation effects comes from the fact that the body-centred cubic (bcc) crystal structure of iron itself is *anomalous*. A simple examination of the Periodic Table shows that in the absence of magnetism, iron would adopt the hexagonal closed packed (hcp) structure, and hence the

stabilization of its bcc structure is a magnetic phenomenon [1]-[3]. The structure of radiation defects in transition metals also reflects this magnetic anomaly, with a self-interstitial defect in iron adopting the  $\langle 110 \rangle$  dumbbell configuration, whereas in all the non-magnetic bcc metals a self-interstitial defect is a  $\langle 111 \rangle$  crowdion [4],[5].

The main challenge associated with the modeling of steels is the fact that their structural and mechanical properties are determined by magnetism. This requires developing new physical approximations and mathematical algorithms capable of describing the entire complexity of phenomena resulting from the interplay between magnetism and elastic deformations, phase transformations, the finite temperature effects, excitation of spin waves and magnon-phonon interactions, and the presence of magnetic solute atoms and impurities. In this thesis, the first step is made towards addressing this complexity by implementing a new method for the treatment of the dynamics that has to link the kinematics of atoms and the precession of their spins.

## 1.2 Origin of Atomic Spins

In a transition metal, the angular moments (spins) of atoms, and the associated magnetic moments, are formed due to the exchange interaction between intra-atomic  $d$ -electrons in the partially filled atomic  $d$ -shells. According to Hund's rule, for an isolated atom with a given number of  $d$ -electrons, the adopted electronic configuration is the one that maximizes the total magnetic moment. For

example, an individual iron atom containing seven  $d$ -electrons (Figure 1.1) has a magnetic moment of  $3\mu_B$  in agreement with the fact that the difference between the number of electrons in the full spin-up sub-shell, containing five  $d$ -electrons, and the number of electrons in the spin-down sub-shell, containing the remaining two electrons, equals three.

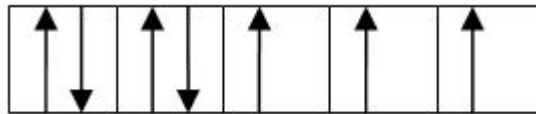


Figure 1.1 – The electron configuration of an individual iron atom containing seven  $d$ -electrons, according to Hund's rule

In a metal, on the other hand, the  $d$ -electrons (or, more precisely,  $s$ - and  $d$ -electrons) are hybridized and their  $s$ -character allows them to become itinerant, hopping or tunneling from one lattice site to another, while their  $d$ -character governs their localization near the atomic nuclei [6]. This kind of collective behavior for strongly interacting electrons is the main cause of magnetism. The saturation magnetization can be determined from the difference of the Fermi energy of the majority and minority spin sub-bands (Figure 1.2), the formation of which is to minimize the total energy as governed by the Stoner instability [7]. The interplay between the intra-atomic exchange and inter-atomic quantum hopping affects both the magnitudes and directions of the moments, which accordingly adopt a ferromagnetic, antiferromagnetic, or a complex non-collinear magnetic configuration. The concept of a localized “atomic spin” is thus justified for itinerant magnets, a simple example of which is given, in a tight-binding treatment, by the single-band Hubbard model [6]. An effective interatomic spin-spin

interaction of the Heisenberg form can also be introduced using the concept of an effective intersite exchange coupling function. Dudarev and Derlet [8] showed that a more sophisticated tight-binding multi-band Hamiltonian could be mapped into a semi-empirical potential with scalar and vector parts, which resemble the embedded atom method (EAM) form and Heisenberg form respectively.

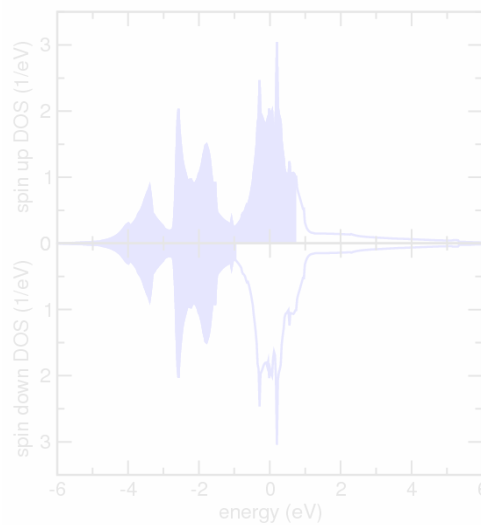


Figure 1.2 – Density of states plot illustrating the occupation of the majority and minority  $3d$ -bands in the ferromagnetic configurations of the bcc  $\alpha$ -iron. (Reprinted from Ref. [7] with the permission from authors.)

Due to the simultaneously localized and itinerant nature of the hybridized electrons in a transition metal, the directions and magnitudes of the atomic spins are both variable quantities [9]. In the ferromagnetic ground state of  $\alpha$ -Fe (bcc iron), all the atomic spins are aligned in the same direction and with saturation magnetization  $2.2\mu_B$  [10]. Any deviation from this perfect alignment caused, for example, by thermal agitation, propagates through the material in the form of a spin wave *via* the exchange coupling between spins [11] (Figure 1.3). The spin wave theory corrects the inadequacy of the Stoner model treatment of magnetization at relatively low temperatures [11]-[13] by supplying the missing low-energy

many-body excited states.

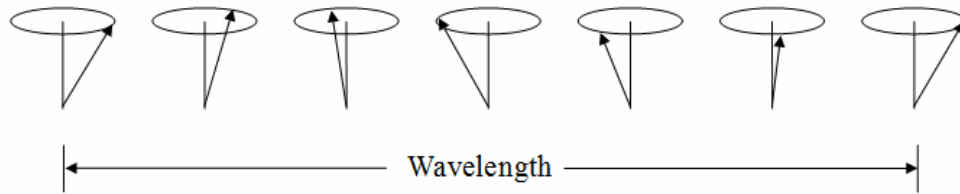


Figure 1.3 – Schematic representation of a spin wave

### 1.3 DFT Spin Dynamics

Density functional theorem (DFT) [14] is a popular method to investigate the ground state of many-body systems. It is rooted on the Hohenberg-Kohn (H-K) theorem and Kohn-Sham (K-S) method. The H-K theorem proved that the ground state wave-function of a many-body system is a unique functional of the ground state electron density, and the ground state electron density minimizes the total energy. The K-S method formally replaced the many-body problem by non-interacting electrons moving in an effective potential, but the effective potential contains the exchange and correlation interaction, which is in an unknown form. In practice, an approximate functional form of the effective potential must be introduced, e.g. local density approximation (LDA) and generalized gradient approximation (GGA). Within the framework of DFT, an enormous amount of studies has been performed by using the adiabatic treatment of non-collinear magnetic ground states and spin dynamics (SD), investigating spin configurations [15],[16], spin wave spectra [17],[18], the dynamical spin susceptibility [19], etc.

Based on the full-potential linearized augmented plane wave (FLAPW) method, Kurz *et al.* [15] introduced a non-collinear *ab-initio* method for the investigation of the magnetic ground state, metastable state and magnetic phase diagram, with examples on Cr,  $\alpha$ -Fe and  $\gamma$ -Fe (fcc iron). Grotheer *et al.* [16] presented a tight-binding linear-muffin-tin-orbital (LMTO) method, which explicitly included the intra-atomic non-collinearity, to calculate the ground state spin configuration of  $\alpha$ -Fe, in the presence of a small transverse external field. They concluded that the atomic-sphere approximation (ASA) for the spin directions may lead to errors proportional to the external field. They [17] also calculated the adiabatic spin wave spectra of Fe, Co, Ni, Ni<sub>3</sub>Fe and CoFe by frozen magnon and transverse susceptibility method. Using the LMTO+ASA method, Morán *et al.* [18] investigated the spin wave spectrum of  $\alpha$ -Fe. They showed the anomalous behavior of the exchange parameters with respect to the lattice constant and the distances between the 1<sup>st</sup>, 2<sup>nd</sup>, 3<sup>rd</sup> and 4<sup>th</sup> nearest neighbors. Savrasov [19] employed the time dependent (TD) DFT with LDA and GGA to calculate the dynamical spin susceptibilities of Fe, Ni and Cr. Capelle *et al.* [20] also performed TDDFT calculations on the SD and spin current. Tawil and Callaway [21] did energy band calculations of iron by employing the tight-binding method with a basis set consisted of atomic wave functions expressed as linear combination of Gaussian-type orbitals determined from the self-consistent potential. Singh *et al.* [22] advanced such method to include the spin-orbit interaction. Autès *et al.* [23] investigated the magnetic anisotropy energy of the surface and monatomic wire of iron by using a parameterized tight-binding model. Many-body excited states such as due to the excitation of magnons (spin waves) are not considered in these

calculations.

While most of the DFT calculations only concern the ground state behavior at 0K, Lichtenstein *et al.* [24] attempted to introduce temperature effects by quantum Monte Carlo (MC) technique. They combined the LDA and the dynamical mean field theory (DMFT), and calculated the magnetization curves, magnitudes of magnetic moments and Curie temperatures  $T_c$  of Fe and Ni. However, their  $T_c$  are 100% overestimated. Kakehashi [25] commented that the overestimation is due to the use of an Ising type Hamiltonian which neglected the transverse exchange coupling. Based on the dynamical coherent potential approximation (DCPA) with single-site approximation (SSA), Kakehashi [25] treated spin and charge fluctuations associated with the electron correlation. The effect of spin waves was included statistically by using MC technique [25],[26], or the harmonic approximation [27]. The equilibrium magnetization evaluated as a function of temperature agrees well with the experiment. Kakehashi *et al.* [28] also introduced the so-called “Molecular Dynamics approach” to model the high temperature behavior of magnetic moments. However, the dynamics of the lattice was not really addressed, despite the name molecular dynamics (MD).

## 1.4 DFT Spin-Lattice Coupling

The occurrence of magnetic anisotropy, magneto-elasticity, and magnetostriction provides evidence that coupling exists between atomic spin orientations and the symmetry of the lattice. For example, coupling between the

spin waves and phonons was explicitly included in the thermodynamic treatment of the ferromagnetic free energy in the early work by Kittel and Abrahams [29]. However, the coupling between the spin and the lattice subsystems, although taken into account, is not treated with full self-consistency. Thus, only the spin-wave would affect the behavior of the lattice subsystem, but not the other way round. In the works of Kakehashi and his colleagues [25]-[28] mentioned in the foregoing subsection, although the magnetic moments was treated dynamically, the lattice was only treated statically, and the full dynamics of the system does not follow.

The non-interacting spin-phonon approximation is often applied to treat low temperature cases where the densities of both the phonons and spin waves are low [11]. The oscillation of the crystal field can be treated as a perturbation that leads to electronic excitations, e.g. the transition from  $3d$  to  $4p$  in iron. This facilitates momentum transfer by creation or annihilation of spin waves  $\mathbf{q}$ ,  $\mathbf{q}'$  and phonons  $\mathbf{k}$ ,  $\mathbf{k}'$ , with  $\mathbf{k} + \mathbf{q} = \mathbf{k}' + \mathbf{q}'$ . The one-phonon and two-phonon processes are known as the direct and Raman processes respectively [30]. The mechanism that furnishes energy transfer from one normal mode to another is caused by the coupling of the anharmonic terms [31]. Sabiryanov and Jaswel [32] studied the magnons and magnon-phonon interactions of bcc and fcc iron using the magnon dispersion curves with and without phonon excitation. Unfortunately, this approximation fails at higher temperatures where the elementary excitations due to the spin and lattice vibrations can no longer be treated as independent, and where full dynamical simulations describing the interacting spin waves (magnons) and lattice waves (phonons) [11] have to be implemented.

Antropov *et al.* [33] made the first attempt to deal with the coupled spin and lattice subsystems at finite temperature about ten years ago. They combined *ab-initio* SD with *ab-initio* MD to take into account spin-lattice interactions. Although both the stochastic (based on the Fokker-Planck equation) and deterministic (based on the Nose-Hoover thermostat) methods were noted as possible ways of treating the finite temperature case, no finite temperature calculations had actually been performed. Stocks *et al.* [34] further criticized that since the method proposed by Antropov *et al.* [33] was based on the local spin density approximation (LSDA), it was only valid for the ground state of the system, and hence the non-collinear states treated in the simulations were not sufficiently well defined. Stocks *et al.* [34] proposed a constrained local moment model for the *ab-initio* spin dynamics. They introduced a constraint field to the LSDA by Lagrange multipliers, which ensured the iterative output of the local magnetization is in the same direction of the prescribed direction that is calculated from the classical equation of spin motion. Later on, Stocks *et al.* [35] introduced an empirical dissipative term and applied the new simulation scheme to the treatment of magnetism at surfaces and in nanostructures. Nevertheless, a full treatment of the temperature effects has yet to be developed.

## 1.5 Classical Spin Dynamics

In cases where the transfer of energy and angular momentum in and out of the spin subsystem has to be considered in the non-adiabatic context, the Landau-Lifshitz (LL) or the Gilbert equations [36] have been applied to treat spin

dynamics within the classical approximation, where interaction with the thermal reservoir is simulated *via* a model dissipative force. In the literature, the LL (equation 1.1) and Gilbert equations (equation 1.2) are usually written in the form for magnetization of a small volume [36],[37]:

$$\frac{\partial \mathbf{M}}{\partial t} = -\gamma \mathbf{M} \times \mathbf{H}_{eff} - \frac{\alpha \gamma}{M} \mathbf{M} \times (\mathbf{M} \times \mathbf{H}_{eff}) \quad (1.1)$$

$$\frac{\partial \mathbf{M}}{\partial t} = -\gamma' \mathbf{M} \times \mathbf{H}_{eff} + \frac{\alpha}{M} \mathbf{M} \times \frac{\partial \mathbf{M}}{\partial t} \quad (1.2)$$

where  $\gamma > 0$  is the gyromagnetic ratio,  $\gamma' = \gamma(1 + \alpha^2)$ ,  $\mathbf{M}$  is the magnetization per unit volume,  $\mathbf{H}_{eff} = -\frac{\delta H}{\delta \mathbf{M}}$  is the effective field and  $H$  is the Hamiltonian. The magnitude of the dimensionless damping constant  $\alpha > 0$  characterizing the rate of dissipation can be estimated from the ferromagnetic resonance (FMR) absorption linewidth [38]-[43]. Theoretical and experimental arguments suggest that the damping constant depends on the temperature [39],[40], composition [41],[42] and topological symmetry [42],[43] of a particular system. For example, the damping constant shows a slow increase in Co and Fe when temperature increases [39]. In the  $\text{Fe}_x\text{Co}_{1-x}$  alloy films [41], the damping constant is almost constant from  $x = 0.5$  to 1, but gradually increases as the cobalt-content increases. Furthermore, the equations of spin motion derived from DFT suggest that a tensor representation reflecting the symmetry of the crystal may be needed to provide a more accurate treatment of the dissipation [44].

At this point, it is to be noted that classical approximation may inhibit some

quantum behaviors especially at low temperatures. Since the formation of magnetic moments or atomic spins are due to the strong electron interaction that is of quantum nature, observables calculated in the classical limit and those measured experimentally may differ quantitatively, but the qualitative trend should not differ. Moreover, both the original LL and Gilbert equations are purely dissipative (Figure 1.4). Thus, if one follows the spin dynamics equations and assumes a constant dissipation rate, all the atomic spins will eventually become stationary and collinear as the spin subsystem relaxes towards the ground-state configuration.

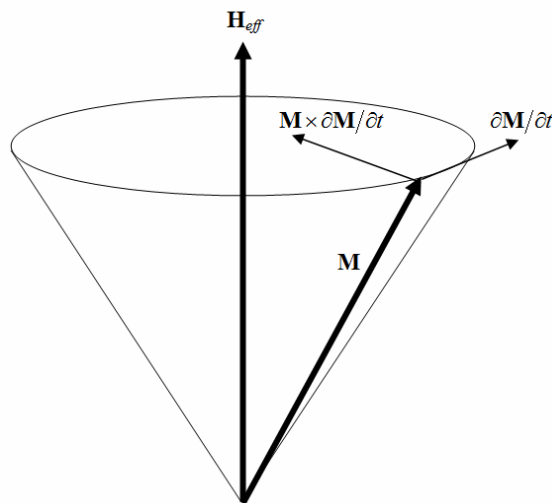


Figure 1.4 – Schematic representation of the magnetization precession with damping, according to Gilbert equation

Therefore, the LL and Gilbert equations do not describe the thermal equilibration of the spin subsystem. If one defines the spin temperature  $T_s$  and assumes that the heat flow in and out of the spin subsystem is proportional to the temperature difference  $\Delta T$  between the spin and the reservoir [45], the dissipation rate can be taken as being proportional to  $\Delta T$  and hence can be positive or negative, driving the transfer of energy and angular momentum in and out of the spin

subsystem. However, defining the spin temperature proves to be a subtle problem because spin dynamics is described by a set of first order differential equations. The notion of the kinetic energy cannot be introduced to define the temperature as it is normally done in conventional MD.

In order to tackle the subtlety of spin temperature, Brown [46] proposed a stochastic method based on the fluctuation-dissipation theorem (FDT) [47],[48] for classical spin systems, through which the spin temperature can be defined by matching the solution of the corresponding Fokker-Planck equation to the Gibbs distribution. Due to the constraint imposed on the fluctuation and dissipation terms, the system is driven to an equilibrium state with respect to the desired temperature. In this way, FDT may provide, for example, the definition of the temperature of a Brownian particle interacting with its environment [48]. García-Palacios and Lázaro [49] used the stochastic Gilbert equation to evaluate the susceptibility of interacting spin waves and the dynamics of magnetic nano-particles, whereas Fähnle *et al.* [50] implemented the stochastic classical spin dynamics equation to speed up *ab-initio* calculations in a combination of atomistic and micro-magnetic approaches. In fact, the works by Brown also form part of the foundation of the current thesis. The FDT for classical spins will be discussed in more detail in a later chapter of this thesis.

## 1.6 MD for Magnetic Materials

The treatment of dynamical processes in a many-body system at a finite

temperature requires treating excited many-body electronic states, for which the effectiveness of *ab-initio* calculations is limited. At present, much of the understanding of finite temperature properties of materials is derived from MD simulations. As opposed to an electronic structure based order- $N^3$  approach, an MD simulation is an order- $N$  method, making it possible to investigate processes on the scale that is many orders of magnitude greater. The evolution of an atomic system at a finite temperature is modeled by integrating, starting from a certain initial configuration, the equations of motion for classical particles interacting *via* a certain interatomic potential. Compliance with thermodynamic equilibrium/quasi-equilibrium conditions is achieved by imposing some appropriate statistical mechanical constraints.

Similarly, at a fundamental level the behavior of a magnetic material is completely determined by their spin-dependent electronic structure. The *ab-initio* approaches to the treatment of electronic structure are, with current computation power, only able to describe very small systems containing no more than  $\sim 1000$  atoms. However, central to the capability to foretell material performance and device functionality is a good understanding of the involved dynamic processes. At the same time, simulating the dynamics of formation and migration of defects, dislocations, magnetic domains and grain boundaries, phase transformations, fracture toughness, plasticity and collision cascades initiated by incident energetic particles requires treating mega-systems containing in excess of a million atoms. A realistic simulation must also be able to describe various saddle-point configurations and the many-body excited states associated with those processes. Also, it has to describe energy dissipation and entropy production due to scattering

of interacting phonons and magnons. There is as yet no atomistic simulation method comparable with MD that would provide a mathematical framework suitable for this purpose.

Within the embedded atom method (EAM) formalism [51]-[53], one can construct semi-empirical many-body potential for MD simulations by fitting to an unending list of properties that can be obtained from experiments and *ab-initio* calculations, e.g. elastic constants, vacancy and interstitial formation energies, surface relaxation and etc. Nevertheless, in magnetic materials, e.g.  $\alpha$ -Fe, magnetism does contribute to the structural stability. The coupling between the spins of neighboring atoms must be taken into account in the treatment of interactions between atoms. Formalisms aimed at including magnetic effects in the interatomic potentials were discussed by Dudarev and Derlet [54] and by Ackland [55]. The magnetic potential developed for iron by the former authors (the DD potential) is based on a combination of the Stoner ‘local band’ treatment of ferromagnetism and the Ginzburg-Landau model, relating the strength of inter-atomic interaction to the magnitude of the local atomic magnetic moment. The size of the system that can be simulated using the magnetic potential is many orders of magnitude larger than that accessible to DFT. For example, large-scale MD simulation based on the DD potential made it possible to investigate magnetic/non-magnetic transformations occurring in amorphous iron under pressure at 0K [56]. Various applications of the DD potential to the treatment of defects and dislocations in magnetic iron in the limit of large system size were reviewed in Ref. [7]. Recently, Björkas and Nordlund [57] adjusted the short range part of the DD potential and compared cascade damage simulations in Fe using

three different potentials. They showed that all of the potentials produce concurrent results on the defect production within statistical uncertainty.

## 1.7 Spin-Lattice Dynamics Simulation

The magnetic interatomic potentials of Dudarev and Derlet [7] and Ackland [54] treats magnetism as a 0K phenomenon, with magnetic moments evaluated using total energy minimization, assuming perfectly collinear atomic spins. The complication of non-collinear spin configurations is not considered. The fundamental dynamics problem associated with coupled motions of the atoms and their spins that should be taken into account at a finite temperature remains unsolved. As opined in the foregoing, the challenge comes from the interaction between the spin waves (magnons) and lattice vibrations (phonons), which require an explicit consideration of the directional spin degrees of freedom. Omitting these degrees of freedom prevents a conventional MD simulation from balancing the flow of energy between the lattice and the spin subsystems, and restricts its application to the limit of weak spin-lattice coupling, or low temperatures. The currently available atomistic models of iron based on the magnetic potential formalism do not consider the directions of magnetic moments as independent variables, and hence do not capture the effects of the thermal orientational disorder of magnetic moments on the interatomic forces.

Recently, Kadau *et al.* [58] considered a classical Hamiltonian for the coupled lattice and spin degrees of freedom, and investigated the phase stability of the

lattice. The simulation is a combination of MD and MC techniques. The Hamiltonian consists of a Lennard-Jones pair potential and a Heisenberg term. The lattice part is governed by the equations of motion and simulated by MD, while the temperature excitation of the spin part was simulated using MC. The Invar effect and the antiferromagnetic ordering of spins in a FeNi alloy were successfully simulated, confirming the significant effect of the spin degrees of freedom on the lattice stability and elastic properties of the material. However, though they employed a coordinate-dependent exchange function, they used an Ising model which neglected the spin wave excitation. Moreover, the MC approach cannot really reproduce the dynamics of the interacting lattice and spin subsystems.

The goal of this thesis is to develop a reformulation of MD that includes the spin degrees of freedom on an equal footing with the degrees of freedom of the lattice. The coupled spin and lattice excitations are treated within a unified simulation framework, taking the positions of atoms and orientations of atomic spins as independent variables. The equations of motion for spins are derived from a generalized Heisenberg Hamiltonian, where the exchange coupling function is fitted to the *ab-initio* data. The scalar part of the inter-atomic interaction is given by the magnetic DD potential [8],[54]. These equations form the basis for the Spin-Lattice Dynamics (SLD) algorithm. They are integrated using the symplectic 2<sup>nd</sup> order Suzuki-Trotter decomposition (STD) [59]-[63] technique for the non-commuting evolution operators for the lattice and the spin degrees of freedom. The position of each atom and the orientation of its spin are determined at each simulation time step. The coordinate dependence of the exchange coupling function links evolutions of the spin and the lattice subsystems, and is responsible

for the spin-orientation-dependent part of inter-atomic forces. The “spin temperature” is introduced using the stochastic Langevin dynamics formulation proposed by Brown [46] combined with the fluctuation-dissipation theorem (FDT). Since it is not feasible to work on large-scale systems without parallel programming, a special parallel algorithm for the STD is developed. Several applications will then be addressed, which show the importance of including spin degrees of freedom in the dynamics simulations.

## 1.8 Validation and Applications

As mentioned in the foregoing, both the direction and magnitude of the magnetic moment of each atom are changing during the simulation. To gain the necessary experience, a conventional MD simulation was performed to study the magnetic properties of  $\mu$ -Fe (amorphous iron) under pressure by using the DD potential at 0K, in which the spin direction does not change with time. As the density increases the magnitude of the average magnetic moment reduces, accompanied by the transformation of an increasing proportion of atoms from a magnetic to a non-magnetic configuration. It shows the relationship between the magnitude of magnetic moment and the local environment. Then, the directions of spins are incorporated by the newly developed SLD method. It is tested in a simulation of adiabatic relaxation of a periodic array of  $180^\circ$  domain-walls in ferromagnetic  $\alpha$ -Fe. Transient processes involving non-equilibrium spin-spin and spin-lattice relaxations are investigated. Sound wave is produced during the decay of domain walls. The relaxation time for energy equilibration between the spin and

lattice subsystem obtained from our simulation is in good agreement with experimental result.

One may note that for an isolated system, conservation of energy and angular momentum have to be satisfied. For this reason, it is impossible to introduce temperature in the spin subsystem because of the associated change in angular momentum. The FDT is employed to generalize the SLD simulation scheme to provide the option of treatment for a system that can exchange energy and angular momentum with a physically meaningful thermostat. Using this scheme, isothermal-isobaric ensemble simulations of spin-lattice relaxation at various temperatures can be performed to investigate equilibrium magnetic properties of the material. The equilibrium magnetization curve so calculated follows closely the mean-field classical approximation, and agrees satisfactorily with experimental data all the way up to the Curie temperature. The equilibrium time-correlation function of spin orientations, which can only be observed in a dynamics system, is also investigated. The lattice constants and elastic constant for bulk  $\alpha$ -Fe as a function of temperature are calculated. They are compared with experiment and EAM potentials without spin degrees of freedom. A strong magneto-mechanical effect is found for temperatures higher than  $\sim 600\text{K}$ . The observed anomaly of the elastic constants in experiments is reproduced only when the spin degree of freedoms is incorporated. In the case of surfaces and thin films, the magnitude and direction of magnetic moment is shown to compete with each others. It explains the change of magnetization profile across the thin film according to temperature, and the difference between DFT calculations and experimental results.

**REFERENCE:**

- [1] D. G. Pettifor, *Bonding and Structure of Molecules and Solids* (Oxford University Press, Oxford, 1995).
- [2] M. Friák, M. Šob, and V. Vitek, *Phys. Rev. B* **63**, 052405 (2001).
- [3] H. C. Herper, E. Hoffmann, and P. Entel, *Phys. Rev. B* **60**, 3839–3848 (1999).
- [4] D. Nguyen-Manh, A. Horsfield, and S. L. Dudarev, *Phys. Rev. B* **73**, 020101 (2006).
- [5] P. M. Derlet, D. Nguyen-Manh, and S. L. Dudarev, *Phys. Rev. B* **76**, 054107 (2007)
- [6] J. Hubbard, *Proc. Roy. Soc. London Ser. A* **276**, 238 (1963)
- [7] P. M. Derlet, S. L. Dudarev, *Prog. Mater. Sci.* **52**, 299 (2007)
- [8] S. L. Dudarev and P. M. Derlet, *J. Computer-Aided Mater. Des.* **14**, 129 (2007)
- [9] J. Hubbard, *Phys. Rev. B*, **19**, 2626 (1979); J. Hubbard, *Phys. Rev B* **11**, 4584 (1979)
- [10] E. P. Wohlfarth, *Ferromagnetic Materials: A handbook on the properties of magnetically ordered substances, Volume 1, Chapter 1* (Elsevier North-Holland, INC., 1980)
- [11] J. Van Kranendonk and J. H. Van Vleck, *Rev. Mod. Phys.* **30**, 1 (1958)
- [12] J. H. Van Vleck, *Rev. Mod. Phys.* **17**, 27 (1945)
- [13] B. E. Argyle, S. H. Charap and E. W. Pugh, *Phys. Rev.* **132**, 2051 (1963)
- [14] M. C. Payne, M. P. Teter, D. C. Allan, T. A. Arias and J. D. Joannopoulos, *Rev. Mod. Phys.* **64**, 1045 (1992)
- [15] Ph. Kurz, F. Förster, L. Nordström, G. Bihlmayer and S. Blügel, *Phys. Rev. B* **69**, 024415 (2004)

- [16] O. Grotheer, C. Ederer and M. Fähnle, *Phys. Rev. B* **62**, 5601 (2000)
- [17] O. Grotheer, C. Ederer and M. Fähnle, *Phys. Rev. B* **63**, 100401 (2001)
- [18] S. Morán, C. Ederer and M. Fähnle, *Phys. Rev. B* **67**, 012407 (2003)
- [19] S. Y. Savrasov, *Phys. Rev. Lett.* **81**, 2570 (1998)
- [20] K. Capelle, G. Vignale and B. L. Györfy, *Phys. Rev. Lett.*, **20**, 206403 (2001)
- [21] R. A. Tawil and J. Callaway, *Phys. Rev. B*, **7**, 4242 (1973)
- [22] M. Singh, C. S. Wang and J. Callaway, *Phys. Rev. B*, **11**, 287 (1975)
- [23] G. Autè, C. Barreteau, D. Spanjaard and M. Desjonquères, *J. Phys.: Condens. Matter*, **18**, 6785 (2006)
- [24] A. I. Lichtenstein, M. I. Katsnelson and G. Kotliar, *Phys. Rev. Lett.*, **87**, 067205 (2001)
- [25] Y. Takehashi, *Phil. Mag.* **86**, 2603 (2006)
- [26] Y. Takehashi, *Adv. Phys.* **53**, 497 (2004)
- [27] Y. Takehashi and J. H. Samson, *Phys. Rev. B* **33**, 298 (1986)
- [28] Y. Takehashi, S. Akbar and N. Kimura, *Phys. Rev. B* **57**, 8354 (1998)
- [29] C. Kittel and E. Abrahams, *Rev. Mod. Phys.* **25**, 233 (1953)
- [30] K. P. Sinha and U. N. Upadhyaya, *Phys. Rev.*, **127**, 432 (1962)
- [31] J. H. Van Vleck, *Phys. Rev.*, **59**, 730 (1941)
- [32] R. F. Sabiryanov and S. S. Jaswal, *Phys. Rev. Lett.* **83**, 2062 (1999)
- [33] V. P. Antropov, M. I. Katsnelson, M. van Schilfgaarde and B. N. Harmon, *Phys. Rev. Lett.* **75**, 729 (1995); V. P. Antropov, M. I. Katsnelson, B. N. Harmon, M. van Schilfgaarde and D. Kusnezov, *Phys. Rev. B* **54**, 1019 (1996)
- [34] G. M. Stocks, B. Ujfalussy, X. Wang, D. M. C. Nicholson, W. A. Shelton, Y. Wang, A. Canning and B. L. Györfy, *Phil. Mag. B* **78**, 665 (1998)
- [35] G. M. Stocks, M. Eisenbach, B. Ujfalussy, B. Lazarovits, L. Szunyogh and P.

- Weinberger, *Prog. Mater. Sci.* **52**, 371 (2007)
- [36] T. L. Gilbert, *IEEE Trans. Magn.* **40**, 3443 (2004)
- [37] J. Miltat, G. Albuquerque and A. Thiaville, “An Introduction to Micromagnetics in the Dynamics Regime” in “Spin Dynamics in Confined Magnetic Structures I”, Edited by B. Hillebrands and K. Ounadjela (Springer, 2002)
- [38] S. M. Bhagat, J. R. Anderson and L. L. Hirst, *Phys. Rev. Lett.* **16**, 1099 (1966);  
S. M. Bhagat, J. R. Anderson and Ning Wu, *Phys. Rev.* **155**, 510 (1967)
- [39] S. M. Bhagat and P. Lubitz, *Phys. Rev. B* **10**, 179 (1974)
- [40] J. F. Cochran, J. M. Rudd, W. B. Muir, G. Trayling and B. Heinrich, *J. Appl. Phys.* **70**, 6545 (1991)
- [41] F. Schreiber, J. Pflaum, Z. Frait, Th. Mühge and J. Pelzl, *Solid State Comm.* **93**, 965 (1995)
- [42] C. Scheck, L. Cheng, I. Barsukov, Z. Frait and W. E. Bailey, *Phys. Rev. Lett.* **98**, 117601 (2007)
- [43] R. Urban, G. Woltersdorf and B. Heinrich, *Phys. Rev. Lett.* **87**, 217204 (2001)
- [44] D. Steiauf and M. Fähnle, *Phys. Rev. B* **72**, 064450 (2005)
- [45] J. H. Van Vleck, *Phys. Rev.* **57**, 426 (1940)
- [46] W. F. Brown Jr., *Phys. Rev.* **130**, 1677 (1963)
- [47] S. Chandrasekhar, *Rev. Mod. Phys.* **15**, 1 (1943)
- [48] R. Kubo, *Rep. Prog. Phys.* **29**, 255 (1966)
- [49] J. L. García-Palacios and F. J. Lázaro, *Phys. Rev. B* **58** 14937 (1998)
- [50] M. Fähnle, R. Drautz, R. Singer, D. Steiauf and D. V. Berkov, *Comp. Mater. Sci.* **32**, 118 (2005)
- [51] M. W. Finnis and J. E. Sinclair, *Phil. Mag.* **50**, 45 (1984)

- [52] M. S. Daw and M. I. Baskes, *Phys. Rev. Lett.* **50**, 1285 (1983)
- [53] M. S. Daw and M. I. Baskes, *Phys. Rev. B* **29**, 6443 (1984)
- [54] S. L. Dudarev and P. M. Derlet, *J. Phys.: Condens. Matter* **17**, 7097 (2005)
- [55] G. J. Ackland, *J. Nucl. Mater.* **351**, 20 (2006)
- [56] P. W. Ma, W. C. Liu, C. H. Woo and S. L. Dudarev, *J. Appl. Phys.* **101**, 073908 (2007)
- [57] C. Björkas, K. Nordlund, *Nucl. Instr. and Meth. in Phys. Res. B* **259**, 853 (2007)
- [58] K. Kadau, M. Gruner, P. Entel and M. Kreth, *Phase Trans.* **76**, 335 (2003)
- [59] I. P. Omelyan, I. M. Mryglod and R. Folk, *Phys. Rev. Lett.* **86**, 898 (2001)
- [60] I. P. Omelyan, I. M. Mryglod and R. Folk, *Phys. Rev. E* **64**, 016105 (2001)
- [61] I. P. Omelyan, I. M. Mryglod and R. Folk, *Phys. Rev. E* **66**, 026701 (2002)
- [62] S. H. Tsai, M. Krech and D. P. Landau, *Brazil. J. Phys.* **34**, 382 (2004)
- [63] S. H. Tsai, H. K. Lee and D. P. Landau, *Am. J. Phys.* **73**, 615 (2005)

# Chapter 2: Molecular Dynamics

## 2.1 Background and History

Although 50 years is about the mean half-life of human beings (where vampire is not counted), it is just a blip compared to the history of magnetism since its recorded use by Huang Di (黃帝) to direct his army to victory more than 5000 years ago. Molecular Dynamics (MD) [1] only has 50 years of history, but it has already become an almost indispensable tool in a wide range of research areas. Briefly, MD is a computer simulation method that models the dynamics of an ensemble of atoms or molecules, and hence its collective properties under a given set of thermodynamic driving forces and boundary conditions, as a collection of classical particles interacting *via* classical interatomic forces. Although it is based on the deterministic solution of Newton's equations of motion, the stochastic nature of the atomic motion is taken into account *via* the constraints of thermodynamics and statistical mechanics. MD was first introduced in 1957 by Alder and Wainwright [2] in their work on a system of hard spheres moving at constant speed between perfect elastic collisions. Rahman [3] successfully carried out in 1964 the MD simulation of a collection of argon atoms treated as Lennard-Jones particles. More realistic than hard spheres, the forces between Lennard-Jones particles change continuously as the particles move.

During the last decade, the size of ensembles that can be treated by MD simulation has increased rapidly with the fast expansion of computing power. In 1964, Rahman [3] could only work with a model of 864 atoms. Four decades

afterwards, in year 2006, Buehler and Gao [4] reported results of investigation of crack-tip propagation obtained from MD simulations with 4 millions atoms. Indeed, works on pushing the MD simulation to the scale of billion [5] or multi-billion [6] atoms are on going, but the computer resource requirements are tremendous. This rapid expansion, of course, cannot occur without the confidence gained by successful applications experienced by many users. In this regard, MD simulation does not only provide insight into what actual happens in the atomic scale, but more importantly, the connection between the often hypothesized microscopic world and the macroscopic one, where experiments cannot be preformed. In statistical mechanics, most problems are not directly solvable except for a small number of idealized models (e.g. perfect gas) and non-trivial problems (e.g. 2D Ising model). In this regard, MD simulation is privileged in its capability to provide essentially exact solutions, or at least insights, to otherwise unsolvable problems in statistical mechanics.

The statistical nature of MD is justified by the ergodic hypothesis, which states that the statistical ensemble averages are equal to the time averages of the system. Moreover, it is reasonable to assume that an experimental observable, say  $A_{obs}$ , is equal to its time average. i.e.:

$$A_{obs} = \langle A \rangle_{time} = \langle A \rangle_{ens} \quad (2.1)$$

where

$$\langle A \rangle_{time} = \frac{1}{\tau} \int_{t_0}^{t_0+\tau} dt A(\{\mathbf{p}_i(t)\}, \{\mathbf{r}_i(t)\}) \approx \frac{1}{M} \sum_{n=1}^M A(\{\mathbf{p}_i(t_n)\}, \{\mathbf{r}_i(t_n)\}) \quad (2.2)$$

and

$$\langle A \rangle_{ens} = \frac{\int d\mathbf{p}_i^N d\mathbf{r}_i^N A(\{\mathbf{p}_i\}, \{\mathbf{r}_i\}) \exp\left[-H(\{\mathbf{p}_i\}, \{\mathbf{r}_i\})/k_B T\right]}{\int d\mathbf{p}_i^N d\mathbf{r}_i^N \exp\left[-H(\{\mathbf{p}_i\}, \{\mathbf{r}_i\})/k_B T\right]} \quad (2.3)$$

where  $\mathbf{p}_i$  and  $\mathbf{r}_i$  are linear momentum and position respectively. It is to be noted that such assumption only holds when the probability density function for the ensemble is stationary, i.e. when the system is at equilibrium or steady-state.

The simulation results, therefore, may provide us with information of materials and systems well beyond the limits of experimentation. Indeed, from the utilization point of view, MD can provide information where exceptionally hostile operational environment prevails, involving extreme temperatures, stresses, electric, magnetic, and neutron fields, etc, well beyond human experience. MD is also helpful in revealing details of the system behavior at the atomic and molecular level, far beyond what is achievable by the finest equipment available to this date. If more details are desired beyond what can be provided by the brief outline in this thesis, the reader may consult the authoritative book by Allen and Tildesley [1] for an excellent comprehensive picture on the origin, derivation and implementation of MD. At the same time, a brief description of MD will be presented in the following.

## 2.2 Equations of Motion

Within an inertial reference frame, the state of a closed system of classical

particles is expected to be describable as a function of the positions  $\{\mathbf{r}_i\}$  and momentums  $\{\mathbf{p}_i\}$  of all the particles, the values of which are independent of time progression. The Hamiltonian  $H$ , which is proven to be equal to the total energy [7], is such a state function, provided that it does not contain any explicit time dependence, and has potential and kinetic energies independent of each other. The Hamiltonian of a classical system is usually written in the following form:

$$H = \sum_i \frac{\mathbf{p}_i^2}{2m_i} + U(\{\mathbf{r}_i\}) \quad (2.4)$$

where  $m_i$  is the mass of atom  $i$ . In terms of the Hamiltonian, the motions of atoms can be described through the following set of differential equations [5].

$$\begin{cases} \dot{\mathbf{p}}_i = -\frac{\partial H}{\partial \mathbf{r}_i} = -\frac{\partial U}{\partial \mathbf{r}_i} \\ \dot{\mathbf{r}}_i = \frac{\partial H}{\partial \mathbf{p}_i} = \frac{\mathbf{p}_i}{m_i} \end{cases} \quad (2.5)$$

By solving the set of equations 2.5, we may obtain all the information of the classical system, i.e. positions, momentums and forces. In principle, the system is now deterministic and predictable. Comparing the Hamiltonian's equations with Newtonian dynamics yields:

$$\mathbf{F}_i = m_i \mathbf{a}_i = m_i \dot{\mathbf{v}}_i = \dot{\mathbf{p}}_i \quad (2.6)$$

where  $\mathbf{F}_i$  is the force and  $\mathbf{a}_i$  the acceleration. In Newtonian dynamics, motion is a result of external forces, while in Hamiltonian dynamics, motion occurs to preserve the total Hamiltonian.

## 2.3 Solution of the equation of motion: Integration

### Algorithms

The forces acting on an ensemble of atoms are continuously changing during its motion. However, numerically it is obvious that only the forces on the atoms at discrete times can be calculated, from which the positions and velocities of the particles over a certain discrete time-interval (step) can be predicted subjected to some numerical error depending the size of the time-interval. Normally, a time-step that is two orders of magnitude smaller than the typical atomic vibration cycle of  $\sim 0.1$  picosecond ( $10^{-13}$  s) is sufficiently small to avoid significant discretization errors. However, MD may still accumulate fatal numerical errors due to energy and momentum non-conservation as a result of the enormous number of time steps. Energy and momentum conservations are therefore important issues in the selection of integration scheme. A suitable algorithm can enhance the overall accuracy and performance significantly.

The set of simultaneous equations in equation 2.5 can be recast into the following form [8]:

$$\begin{aligned} \frac{d}{dt} \begin{pmatrix} \mathbf{p}(t) \\ \mathbf{r}(t) \end{pmatrix} &= \begin{pmatrix} -\frac{\partial}{\partial \mathbf{r}} U(\mathbf{r}) \\ \frac{\partial}{\partial \mathbf{p}} K(\mathbf{p}) \end{pmatrix} = \begin{pmatrix} 0 & -\hat{U} \\ \hat{K} & 0 \end{pmatrix} \begin{pmatrix} \mathbf{p}(t) \\ \mathbf{r}(t) \end{pmatrix} \\ &= (\mathcal{K} + \mathcal{V}) \begin{pmatrix} \mathbf{p}(t) \\ \mathbf{r}(t) \end{pmatrix} = \mathcal{H} \begin{pmatrix} \mathbf{p}(t) \\ \mathbf{r}(t) \end{pmatrix} \end{aligned} \quad (2.7)$$

where  $\mathbf{r} = (\mathbf{r}_1, \mathbf{r}_2, \mathbf{r}_3, \dots, \mathbf{r}_N)$ ,  $\mathbf{p} = (\mathbf{p}_1, \mathbf{p}_2, \mathbf{p}_3, \dots, \mathbf{p}_N)$ ,  $K(\mathbf{p})$  is the kinetic energy,

$U(\mathbf{r})$  is the potential energy,  $\hat{K}$  and  $\hat{U}$  are their corresponding operators, such

$$\text{that } \hat{K}\mathbf{p}(t) = \frac{\partial}{\partial \mathbf{p}} K(\mathbf{p}), \quad \hat{U}\mathbf{r}(t) = -\frac{\partial}{\partial \mathbf{r}} U(\mathbf{r}), \quad \text{and } \mathcal{K} \equiv \begin{pmatrix} 0 & 0 \\ \hat{K} & 0 \end{pmatrix}, \quad \mathcal{U} \equiv \begin{pmatrix} 0 & -\hat{U} \\ 0 & 0 \end{pmatrix}.$$

The formal solution of this first order differential equation is [8]:

$$\begin{pmatrix} \mathbf{p}(\Delta t) \\ \mathbf{r}(\Delta t) \end{pmatrix} = e^{\mathcal{H}\Delta t} \begin{pmatrix} \mathbf{p}(0) \\ \mathbf{r}(0) \end{pmatrix} \quad (2.8)$$

Exponential operator is usually hard to handle. A straightforward way is to diagonalize the Hamiltonian operator  $\mathcal{H}$ . However, the kinetic component  $\mathcal{K}$  can only be diagonalized in the momentum space, whereas the potential component  $\mathcal{U}$  is only diagonalizable in the coordinate space. These two terms are non-commutative, which makes the Hamiltonian operator intractable. Perturbation approximation may be introduced for small  $\Delta t$  by expanding the exponential operator in a Taylor series.

$$e^{\mathcal{H}\Delta t} = I + \mathcal{H}\Delta t + \frac{1}{2} \mathcal{H}^2 \Delta t^2 + O(\Delta t^3) \quad (2.9)$$

The positions and momentums can then be updated as follows [8]:

$$\begin{pmatrix} \mathbf{p}(t+\Delta t) \\ \mathbf{r}(t+\Delta t) \end{pmatrix} \approx (I + \mathcal{H}\Delta t) \begin{pmatrix} \mathbf{p}(t) \\ \mathbf{r}(t) \end{pmatrix} = \begin{pmatrix} \mathbf{p}(t) - \frac{\partial U}{\partial \mathbf{r}} \Delta t \\ \mathbf{r}(t) + \frac{\partial K}{\partial \mathbf{p}} \Delta t \end{pmatrix} \quad (2.10)$$

Higher order terms can also be included, but the infinite tail must be truncated.

Since the evolution is an approximate solution, the volume of phase space does not

conserve. This kind of approximation necessarily introduces dissipative perturbations to the Hamiltonian system, which causes the total energy to deviate from the starting value.

Therefore, it is necessary to find another approximation scheme that has symplecticity, i.e., conserves the volume in phase space [8]. The Suzuki-Trotter decomposition (STD) is an approximation method that provides a way to achieve this goal. Its 2<sup>nd</sup> order form is expressed as follows:

$$e^{(A+B)\Delta t} = e^{A(\Delta t/2)} e^{B\Delta t} e^{A(\Delta t/2)} + O(\Delta t^3) \quad (2.11)$$

where  $A$  and  $B$  are arbitrary operators. It is easy to prove the validity of equation 2.11 by expanding both sides. If  $A=\mathcal{U}$  and  $B=\mathcal{K}$ , since  $\mathcal{U}^2 = \mathcal{K}^2 = 0$ , all the higher order terms vanish, and

$$\begin{cases} e^{\mathcal{U}\Delta t} \equiv I + \mathcal{U}\Delta t \\ e^{\mathcal{K}\Delta t} \equiv I + \mathcal{K}\Delta t \end{cases} \quad (2.12)$$

The evolution of the positions and momentums can be calculated one by one according to the sequence as expressed in equation 2.11. The kinetic and potential operators are treated exactly, except for trajectory and machine errors. The symplecticity is attained. No dissipation and approximation is introduced in each operation.

In this scheme, the equation of motion, i.e., equation 2.8, becomes

$$\begin{aligned}
\begin{pmatrix} \mathbf{p}(t + \Delta t) \\ \mathbf{r}(t + \Delta t) \end{pmatrix} &= e^{v\Delta t/2} e^{\kappa\Delta t} e^{v\Delta t/2} \begin{pmatrix} \mathbf{p}(t) \\ \mathbf{r}(t) \end{pmatrix} + O(\Delta t^3) \\
&= \begin{pmatrix} \mathbf{p}(t) + m \frac{\mathbf{a}(t) + \mathbf{a}(t + \Delta t)}{2} \Delta t \\ \mathbf{r}(t) + \frac{\mathbf{p}(t)}{m} \Delta t + \mathbf{a}(t) \frac{\Delta t^2}{2} \end{pmatrix} + O(\Delta t^3)
\end{aligned} \tag{2.13}$$

which is indeed equivalent to the velocity Verlet algorithm [1]:

$$\begin{aligned}
\mathbf{x}_i(t + \Delta t) &= \mathbf{x}_i(t) + \mathbf{v}_i(t) \Delta t + \frac{1}{2} \mathbf{a}_i(t) \Delta t^2 \\
\mathbf{v}_i(t + \Delta t) &= \mathbf{v}_i(t) + \frac{\mathbf{a}_i(t) + \mathbf{a}_i(t + \Delta t)}{2} \Delta t
\end{aligned} \tag{2.14}$$

This shows that the velocity Verlet algorithm is symplectic, and is superior to other algorithms in the context of energy conservation. An example in Ref. [8] shows that the perturbation method (equation 2.10) leads to numerical energy dissipation in closed systems for long runs. On the other hand, using the symplectic method, the total energy only fluctuates around the starting value, despite the 2<sup>nd</sup> order accuracy.

## 2.4 Periodic Boundary Condition

The size of the simulation box is usually limited by the storage capacity and execution speed of the host computer. MD simulations with tens or maybe a hundred millions of atoms would be the current upper limit of most research groups, far below the Avogadro's number ( $\sim 6.02 \times 10^{23}$ ). Due to this limitation, surface effects will normally overwhelm bulk properties easily. To mimic an infinite bulk

lattice, the periodic boundary condition [1] is often used.

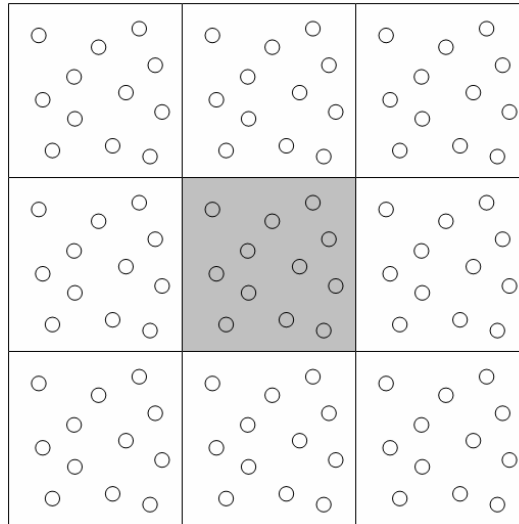


Figure 2.1 – Schematic picture of a 2-dimension periodic system

In principle, the periodic boundary condition is to attach the simulation box to its own images side by side. A schematic picture of a 2-dimension periodic system is shown in Figure 2.1. The center part in grey is the entire simulation box. The remaining white boxes are images. When an atom leaves the simulation box, its image enters the box at the same time, crossing the boundary on the opposite side. It remedies at least part of the problem caused by the small surface to volume ratio for bulk samples, as surfaces are eliminated in such an arrangement. In the 3-dimensional case, the only difference is the number of images, 26 instead of 8.

Nevertheless, the question of how well this infinite periodic system represents a real bulk sample is still nontrivial. In general, if the simulation box is large enough, most artifacts due to the boundary condition may be avoided resulting in a meaningful simulation of equilibrium thermodynamics properties [1]. However, several other issues still require attention. Firstly, the simulation box must be

sufficiently large to avoid the interaction of the simulation cell with its own images. Secondly, the periodicity of the simulation cells sets a limit to the permissible wavelengths of phonons or magnons according to the cell dimensions. For example, phonons or magnons with wavelengths longer than the cell dimensions will be cut off. This may suppress or change the order of some phase transitions that requires the participation of macroscopic fluctuations.

## 2.5 Temperature Control

In the real world, closed system seldom occurs. A system always interacts with its environment. In the microscopic view, energy and momentum exchange occurs among particles *via* scatterings and collisions. Eventually, an open system attains thermodynamic equilibrium with its environment and maintains constant temperature and/or pressure. Therefore, computer simulations must be able to mimic conditions that would be encountered in real experiments. In statistical mechanics, the nature of a system is usually classified by the ensemble it belongs to, namely, the micro-canonical (NVE), canonical (NVT), grand-canonical ( $\mu$ VT) and isothermal-isobaric (NPT) ensemble, where the symbols N,  $\mu$ , V, P, E and T mean constant number of atoms, chemical potential, volume, pressure, energy and temperature, respectively.

In order to control temperature, various types of thermostats have been developed, e.g. Berendsen [9], Nosé-Hoover [10],[11] and Langevin [12] thermostats. The Berendsen thermostat is a kind of rescaling method that adjusts

the temperature by multiplying a factor to the velocities of atoms directly. Sometime, the factor may contain a relaxation time. Nové-Hoover thermostat introduces additional degrees of freedom into the Lagrange equation of motion, which drive the system to the desired temperature by a fictitious force.

In this thesis, the Langevin thermostat based on the fluctuation-dissipation theorem (FDT) [12] is adopted. In this approach, the stochastic nature of atomic motion is explicitly taken into account, and the deterministic equation of motion is replaced by a stochastic equation of motion:

$$m \frac{d\mathbf{v}}{dt} = \mathbf{p} = -\frac{\partial U}{\partial \mathbf{r}} - \gamma \mathbf{v} + \xi(t) \quad (2.15)$$

where  $\gamma$  is the coefficient of dissipative friction characterizing the “viscosity” of the system and  $\xi(t)$  is a delta-correlated random thermal force,

$$\langle \xi(t) \cdot \xi(t') \rangle = \mu \delta(t-t') \quad (2.16)$$

where  $\mu$  is a constant. Equation 2.15 mimics the stochastic motion of atoms in the sea of electrons. In addition to the deterministic forces from the potential field, the motion of the atoms is also driven by dissipative random forces due to the scattering of electrons. Two assumptions are made [12]. Firstly, the random forces are Gaussian distributed, in accordance with the central limit theorem. Secondly, the impact time is short compare with the timescale of atomic motion and successive impacts are delta correlated.

In the present model, the dissipative and random natures of electron scattering

are responsible for transforming the energy of the system into or from heat of the reservoir. There should be a relationship between the viscosity characterized by  $\gamma$ , the energy dissipated in the form of heat flow into the reservoir, related to  $T$  and the strength  $\mu$  of the random forces. Indeed, under thermodynamic equilibrium, the Gibbs distribution

$$W = W_0 \exp\left(-\frac{E}{k_B T}\right) \quad (2.17)$$

is given by the probability density function governed by the Fokker-Planck equation [10]. Substituting the Gibbs distribution into the Fokker-Planck equation yields the relationship:

$$\mu = 6\gamma k_B T, \quad (2.18)$$

where the temperature  $T$ , the coefficient of dissipative friction  $\gamma$  and the strength of the random forces  $\mu$ , are explicitly related. In this model, the deterministic atomic motion is perturbed by frictional and random forces, driving the whole system to the Gibbs distribution at the desired temperature. It is effectively switching the system between micro-canonical ensembles.

## 2.6 Applied Stresses

To specify the applied stress in the simulation, several methods have been proposed [9],[13]-[15]. The Anderson method [13] considers the volume as an

external variable and couples the system with a piston that has mass. The simulation box can be expanded or shrunk isotropically. Parinello-Rahman [12] extended the Anderson method to allow the change of the box-shape. The Constraint method [15] maintains the constant pressure by introducing the Lagrange multiplier into the equation of motions, where the volume is also considered as a variable. In this thesis, a generalized form of the Berendsen [9] method is adopted.

Firstly, we can start from considering the local stress tensor on an atom  $i$ , which is defined by the decomposed virial theorem [1],[16]-[18]:

$$\sigma_{\alpha\beta}^i = \frac{1}{V_i} \left( m_i v_\alpha v_\beta + \frac{1}{2} \sum_{j \neq i} f_{ij\alpha} r_{ij\beta} \right) \quad (2.19)$$

where  $\alpha, \beta$  denotes the Cartesian components. The 1<sup>st</sup> term comes from the kinetic nature of atoms according to the ideal gas law, while the 2<sup>nd</sup> term corresponds to the traction exerted by the interatomic forces.

In this thesis, stresses in simulations are applied *via* normal forces on the orthogonal surfaces of the simulation cell. The rectangular co-ordinate system in which the surface normals form the co-ordinate axes is the principal co-ordinate system in which the stress tensor is diagonal. The stress component  $s_{\alpha\alpha}$  (where  $\alpha = x, y$  or  $z$ ) is the force per unit normal area along the  $\alpha$  direction. The equilibrium configuration of the simulation cell under the applied stress  $s_{\alpha\alpha}$  is obtained by adjusting its dimensions  $\{L_\alpha\}$  gradually, until the average atomic stress balances the external applied stress, i.e.  $s_{\alpha\alpha} = \langle \sigma_{\alpha\alpha}^i \rangle$ . On each time step  $\Delta t$ ,

the  $L_\alpha$  and coordinates of all atoms are rescaled,

$$\begin{cases} L_\alpha' = \chi_\alpha L_\alpha \\ x_i' = \chi_x x_i \\ y_i' = \chi_y y_i \\ z_i' = \chi_z z_i \end{cases} \quad (2.20)$$

where the  $\chi_\alpha = 1 - \frac{\beta_C}{3} \frac{\Delta t}{t_R} (s_{\alpha\alpha} - \langle \sigma_{\alpha\alpha}^i \rangle)$ , which is the rescaling parameter that slightly deviate from 1. Both  $t_R$  and  $\beta_C$  are adjustable parameters, where  $t_R$  is the relaxation time,  $\beta_C$  is the compressibility. Physically, it is equivalent to coupling the system to a “stresses bath”.

As an example, suppose the sample is under a hydrostatic stress, i.e.  $s_{xx} = s_{yy} = s_{zz}$ , equation 2.20 becomes,

$$\begin{cases} V' = \chi V \\ \mathbf{r}_i' = \chi^{1/3} \mathbf{r}_i \end{cases} \quad (2.21)$$

where  $V = L_x L_y L_z$  is the volume of the simulation cell,  $\mathbf{r}_i = \{x_i, y_i, z_i\}$  is the position vector of atom  $i$ ,  $\chi_x \chi_y \chi_z = \chi = 1 - \beta_C \frac{\Delta t}{t_R} (P - \mathcal{P})$  using the approximation of  $(1+x)^{1/3} \approx 1 + \frac{x}{3}$ , the desired pressure  $P = s_{\alpha\alpha}$  and the instantaneous internal

pressure  $\mathcal{P}$  is equivalent to the internal hydrostatic stress  $\mathcal{P} = \sum_i \frac{\sigma_{xx}^i + \sigma_{yy}^i + \sigma_{zz}^i}{3}$ .

Then, equation 2.20 reduced back the original Berendsen [7] method, i.e. equation 2.21.

The lattice configuration in the simulation box may not always have the same symmetry axes as the simulation box. In such cases, the co-ordinate axes are not in the principal directions and the Cartesian stress-tensor is not diagonal. This obviously complicates simulations involving external stresses on non-cubic crystals. Even in cubic crystals, the deformation strain field due to thermal expansion, phase transition, point defects and dislocations, or a general applied stress, etc., may not have the same principal axes along the co-ordinate axes of the simulation cell. In such cases, we also need to deal with the non-diagonal shear terms of the stress tensor. The most sophisticated method to relax the pure shear stresses is changing the shape of simulation box, but a simpler scheme is adopted here. The boundary across the simulation box and its images is mismatched [1] (Figure 2.2).

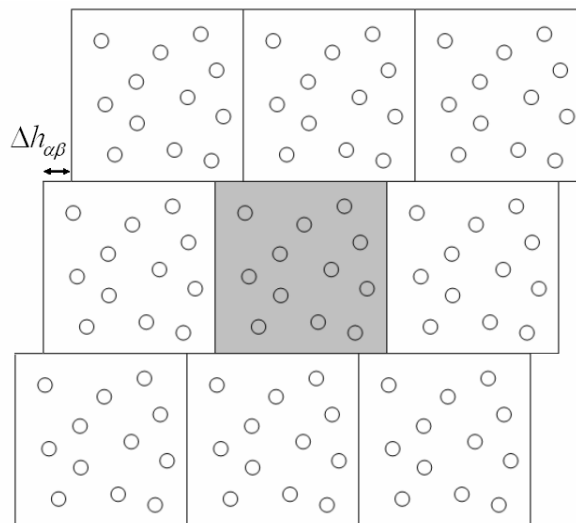


Figure 2.2 – Schematic picture to mismatch the boundary across the simulation box and its images.

The mismatch length  $\Delta h_{\alpha\beta}$  is enhanced or reduced according to the  $\langle \sigma_{\alpha\beta}^i \rangle$ . Then, the coordinate of atoms are relocated in the new positions. Using the  $x - y$  direction

as an example, if  $s_{xy} - \langle \sigma_{xy}^i \rangle \neq 0$ ,

$$\begin{aligned} x'_i &= x_i + \frac{y_i}{L_y} \frac{\Delta t}{t_R} \beta_D (s_{xy} - \langle \sigma_{xy}^i \rangle) \\ \Delta h'_{xy} &= \Delta h_{xy} + \frac{\Delta t}{t_R} \beta_D (s_{xy} - \langle \sigma_{xy}^i \rangle) \end{aligned} \quad (2.22)$$

where the  $\beta_D$  is a constant representing the deformability. Applying the scheme to  $x - y$ ,  $x - z$  and  $y - z$  directions simultaneously, one can deal with all the non-diagonal shear terms.

## 2.7 Magnetic Potential

The inter-atomic potential is an essential component of an MD simulation, with which energies and forces are calculated. The construction of a reliable potential model may require a very substantial effort. First of all, the functional form of the potential is guessed according to certain physical behavior. For example, a pair potential mimics both the attractive and repulsive behavior between two atoms. Then, a basket of simulations would be performed with some preliminary parameters. Parameters or even the functional form is further refined to best fit the *ab-initio* and/or experimental data. This process would iterate several times, until the predictions of the model are within acceptable tolerance.

The functional form base on the embedded atom method (EAM) [16]-[18] is commonly used in the construction of empirical many-body potential. The EAM potential is superior to the pair potential in the context of elastic constants. It has

the following functional form:

$$U = \sum_i^N F[\rho_i] + \frac{1}{2} \sum_{i,j,i \neq j}^N V(r_{ij}) \quad (2.23)$$

where  $F[\rho] = -A\sqrt{\rho}$  and  $\rho = \sum_{j,i \neq j} f(r_{ij})$ . In addition to the repulsive term  $V(r)$ , the model also has a bonding term that is the square root of the effective electron density, which has its origin from the many-atoms interaction. In addition,  $f(r)$  is the pairwise electron-density radial function that describes the magnitude of the hopping integrals.

Generally, EAM potentials for transition metals can be constructed [19] with good agreement to *ab-initio* calculations and experiments. However, the situation becomes complicated in the case of ferromagnetic iron. The presence of magnetism stabilizes the bcc phase of iron at low temperature [20]. The strong coupling between the magnetic moments of neighboring atoms due to exchange and correlation interaction of their shared electrons presents non-trivial problems. Although semi-empirical potentials for iron [21]-[23] have been derived within EAM formalism, they may not always be useful in the study of magnetic properties, since the magnetic contribution to the total energy of interaction between atoms may not be separable. Ackland [24] discussed the inclusion of magnetic effects in a potential for a *d*-band magnetic metal, but never did practice his proposed scheme in an actual magnetic potential. By using a combination of the Stoner ‘local band’ treatment of ferromagnetism and the Ginzburg-Landau model, Dudarev and Derlet (DD) [25],[26] developed a many-body ‘magnetic’ interatomic potential for iron, in

which the total potential energy of  $N$  atoms is written in the same form as equation 2.23, except that,

$$F[\rho] = -A\sqrt{\rho} - \frac{B}{\ln 2} \left( 1 - \sqrt{\frac{\rho}{\rho_c}} \right) \ln \left( 2 - \frac{\rho}{\rho_c} \right) \Theta(\rho_c - \rho) \quad (2.24)$$

Here  $A$  and  $B$  are constants;  $\Theta(x)$  is the Heaviside step function;  $\rho_c$  is the critical electron density at which magnetism vanishes. In addition to the usual many-body contribution (i.e., the first term in equation 2.24) describing the collective interaction of an atom with its environment, this potential explicitly takes into account the local magnetic structure of the environment of a given atom and relates it to the effective local electron density (the second term in equation 2.24), and includes the magnetic contribution to the total energy in the determination of the local atomic configuration. We may understand the physical meaning of such a functional form *via* the regular band model, where the energy per atom can be written as [25],[26]:

$$\begin{aligned} E &= E_{\uparrow} + E_{\downarrow} - I \zeta^2 / 4 \\ &= -\frac{W}{2n} N(n - N) + \frac{1}{2} \left( \frac{W}{n} - \frac{I}{2} \right) \zeta^2 \end{aligned} \quad (2.25)$$

The  $E_{\uparrow}$  and  $E_{\downarrow}$  are the energies of spin up and spin down sub-bands respectively;  $I$  is the Stoner parameter;  $\zeta$  is the magnetic moment;  $W$  is the width of the band;  $n$  is the total number of  $d$  orbitals per atoms;  $N$  is the total number of electrons. It can be seen that the energy is minimized in the non-magnetic state ( $\zeta = 0$ ) when  $I < 2W/N$  and in fully saturated magnetic state when  $I > 2W/N$ .

Similarly, the magnetic effect represented by the second term in equation 2.24 vanishes for  $\rho > \rho_c$ , when the electron correlation is suppressed. It should be noted that both equations 2.24 and 2.25 are only valid for  $T = 0\text{K}$ , when all the atomic spins are collinear and total magnetic moment is either zero or fully saturated. At finite temperatures, the atomic spins are non-collinear. In that case, the interatomic interaction and the degree of non-collinearity are mutually dependent, a point we shall consider in detail in Chapter 4.

To facilitate fast evaluation of forces, the interatomic interaction in the DD potential takes a convenient functional form following the EAM formalism. The magnitude of the local magnetic moment can be explicitly calculated using a simple power law:

$$\zeta = C \left( 1 - \sqrt{\frac{\rho}{\rho_c}} \right)^\gamma,$$

where  $C$  and  $\gamma$  are parameters fitted to the relationship between the magnetic moment and the average volume of bcc iron. Thus, when the system is compressed, the effective electron density increases and the local magnetic moment decreased.

**REFERENCE**

- [1] M. P. Allen and D. J. Tildesley, *Computer Simulation of Liquids*, (Oxford University Press, 1987)
- [2] B. J. Alder and T. E. Wainwright, *J. Chem. Phys.* **27**, 1208 (1957)
- [3] A. Rahman, *Phys. Rev.* **136**, A405 (1964)
- [4] M. J. Buehler and H. J. Gao, *Nature* **439**, 307 (2006)
- [5] F. F. Abraham, R. Walkup, H. Gao, M. Duchaineau, T. Diaz and M. Seager, *Proc. Natl. Acad. Sci.* **99**, 5783 (2002)
- [6] K. Kadau, T. C. Germann and P. S. Lomdahl, *Inter. J. Mod. Phys.* **15**, 193 (2004)
- [7] J. B. Marion and S. T. Thornton, *Classical Dynamics of Particles and systems*, 4<sup>th</sup> Ed. (Harcourt, Inc. 1995)
- [8] N. Hatano and M. Suzuki, *Lect. Notes Phys.* **679**, 37 (2005)
- [9] H. J. C. Berendsen, J. P. M. Postma, W. F. Van Gunsteren, A. Di Nola and J. R. Haak, *J. Chem. Phys.* **81**, 3684 (1984).
- [10] S. Nosé, *Mol. Phys.* **52**, 255 (1984).
- [11] W. G. Hoover, *Phys. Rev. A* **31**, 1695 (1985).
- [12] R. Kubo, *Rep. Prog. Phys.* **29**, 255 (1966)
- [13] H. C. Andersen, *J. Chem. Phys.* **72**, 2384 (1980)
- [14] M. Parrinello and A. Rahman, *Phys. Rev. Lett.* **45**, 1196 (1980); *J. Appl. Phys.* **52**, 7182 (1981); *J. Chem. Phys.* **76**, 2662 (1982)
- [15] D. J. Even and G. P. Morriss, *Chem. Phys.* **77**, 63 (1983)
- [16] M. W. Finnis and J. E. Sinclair, *Phil. Mag.* **50**, 45 (1984)
- [17] M. S. Daw and M. I. Baskes, *Phys. Rev. Lett.* **50**, 1285 (1983)

- [18] M. S. Daw and M. I. Baskes, *Phys. Rev. B* **29**, 6443 (1984)
- [19] P. M. Derlet, D. Nguyen-Manh, S. L. Dudarev, *Phys. Rev. B* **76**, 054107 (2007)
- [20] M. Friák, M. Sob, and V. Vitek, *Phys. Rev. B* **63**, 052405 (2001)
- [21] M. W. Finnis, *Interatomic Forces in Condensed Matter* (Oxford University Press, New York, 2003)
- [22] G. J. Ackland, D. J. Bacon, A. F. Calder and T. Harry, *Phil. Mag. A* **75**, 713 (1997)
- [23] M. I. Mendeleev, S. Han, D. J. Srolovitz, G. J. Ackland, D. Y. Sun and M. Asta, *Phil. Mag.* **83**, 3977 (2003)
- [24] G. J. Ackland, *J. Nucl. Mater.* **351**, 20 (2006)
- [25] S. L. Dudarev and P. M. Derlet, *J. Phys.: Condens. Matter* **17**, 7097 (2005).
- [26] P. M. Derlet and S. L. Dudarev, *Prog. Mater. Sci.* **52**, 299 (2007); UKAEA Fusion Report **530** (2006) available on [www.fusion.org.uk](http://www.fusion.org.uk)

## Chapter 3: Amorphous Iron at $T = 0K$

### 3.1 Brief Introduction

Amorphous materials are produced under non-equilibrium conditions inhibiting crystallization, such as rapid quenching from the melt [1],[2]. The topological disorder constitutes a major factor that dominates properties of such materials. For example, amorphous magnets are soft magnetic materials which show easy magnetization due to the lack of long-range order and magneto-crystalline anisotropy [2]. Due to their non-crystalline structure they exhibit high electrical resistivity, high elastic limit, high magnetic permeability and attractive corrosion resistance [2],[3], which make them useful for many applications, such as high-frequency devices, power distribution transformers, magneto-mechanical transducers and magneto-acoustic devices [3]. However, fabricating pure amorphous iron ( $\mu$ -Fe) samples presented a number of practical challenges, and the properties of  $\mu$ -Fe were extrapolated from those of amorphous systems with very high iron concentration [4]-[6]. The results often proved ambiguous due to the presence of other components in the system. Pure  $\mu$ -Fe only in powder form can now be prepared by the sono-chemical technique [7]-[10].

In the theoretical aspect, magnetism in the ground state of  $\mu$ -Fe was studied almost exclusively using the electronic structure based methods. Kakehashi *et al.* [11]-[17] developed a treatment based on the degenerate-band Hubbard model and proposed that the ground state of  $\mu$ -Fe was a spin-glass. Kakehashi *et al.* investigated the magnetic phase diagram of  $\mu$ -Fe as a function of temperature  $T$  and

the  $d$ -electron occupation number  $N$ . The phase diagram shows a paramagnetic, a collinear ferromagnetic, a non-collinear ferromagnetic and a spin glass state. Turek and Hafner [18] performed electronic structure based molecular dynamics (MD) simulations using interatomic forces calculated using a method that combines the nearly-free-electron and tight-binding-bond approximations. They also performed density functional calculations using 64-atoms supercells in the linear-muffin-tin-orbital (LMTO) approximation. Upon compression, a sample of  $\mu$ -Fe transforms from an inhomogeneous ferromagnetic state into an antiferromagnetic state and then further into a spin-glass state. Krauss and Krey [19] and Krey *et al.* [20] used a LCAO approach combining the Slater-Koster parameterization of the hopping matrix elements of a tight-binding Hamiltonian with the Hartree-Fock treatment of on-site interaction between electrons, and generated the spin configurations for an amorphous cluster containing 54 atoms of iron. Initially, they adopted the conventional spin-up and spin-down approximation and discovered an inhomogeneous ferromagnetic state. Subsequently they generalized the treatment to non-collinear magnetic structures, and found asperomagnetic or speromagnetic energetically favourable configurations. Lorenz and Hafner [21], using tight-binding parameterization of the Hubbard Hamiltonian, showed that as the density of the material increases,  $\mu$ -Fe transforms from the ferromagnetic state into an asperomagnetic state and then into a speromagnetic state. Liebs *et al.* [22],[23] performed *ab-initio* calculations using supercells with 16 or 32 atoms. At low density, the system remained ferromagnetic. At higher density, calculations showed the formation of non-collinear magnetic structures.

All the above calculations were based on density functional theory and/or the

tight-binding Hubbard Hamiltonian. With more than a hundred energy states per atom, the treatment of this Hamiltonian is computationally very demanding and in practice it proves difficult to investigate systems containing more than a few hundred atoms. Thus, the extension of *ab-initio* approaches to the treatment of  $\mu$ -Fe beyond the few hundred atoms scale is problematic. In the DD potential [24],[25], the expression for the energy of interaction between atoms takes a convenient functional form similar to that of the embedded atom method (EAM) [26]-[28] formalism, hence enabling fast evaluation of interatomic forces as well as the magnitude of the local magnetic moment of an atom in a large-scale MD simulation. Using the magnetic DD potential, the relationship between the local topological structure, and magnetic properties of large samples of  $\mu$ -Fe, and the magnetic/non-magnetic transformation occurring under the applied external pressure are investigated. Within the DD approximation, one can investigate how the magnitude of the local magnetic moment (but not its direction) depends on the parameters characterizing the structure, such as the local Voronoi volume of an atom and the number of the nearest neighbors. At this point, let us point out that the calculations in this chapter are only valid at zero temperature, at which the spins are perfectly collinear as the bcc Fe crystal at its many-body ground state. To model the crystal at finite temperatures, the increased internal energy means that the many-body excited state with interacting phonons and magnons must be considered in addition to the interacting atoms. This requires the treatment of the Spin-Lattice Dynamics (SLD) simulation that will be presented in the following chapters.

### 3.2 Simulation Scheme

The DD potential allows calculating the local magnetic moment of an atom (in units of  $\mu_B$ ) as well as the forces acting on it. Both quantities depend on the local environment of the atom. In the following simulations, samples of  $\mu$ -Fe of eight different densities were prepared by rapidly quenching atomic configurations from the melt. MD simulations of the heating and the subsequent quenching process were performed using canonical ( $NVT$ ) ensembles for eight different mass densities, namely  $7.04 \text{ g/cm}^3$ ,  $7.46 \text{ g/cm}^3$ ,  $7.88 \text{ g/cm}^3$ ,  $7.92 \text{ g/cm}^3$ ,  $8.41 \text{ g/cm}^3$ ,  $8.95 \text{ g/cm}^3$ ,  $9.53 \text{ g/cm}^3$  and  $10.2 \text{ g/cm}^3$ . The density of  $7.88 \text{ g/cm}^3$  corresponds to the stress-free equilibrium configuration of bcc iron. By varying the density of the material we simulate the effect of applied hydrostatic stress. In each case, the system consists of approximately 16 thousand atoms initially placed in a regular bcc lattice corresponding to a chosen value of mass density. The size of the simulation cell was approximately  $60 \text{ \AA} \times 60 \text{ \AA} \times 60 \text{ \AA}$  in the  $\langle 111 \rangle$ ,  $\langle \bar{2}11 \rangle$  and  $\langle 0\bar{1}1 \rangle$  directions, respectively. Periodic boundary conditions were applied in all three directions.

To simulate the formation of an amorphous structure by quenching a sample of liquid iron, two complementary methods were used. The first method is to follow Ref. [18] and fast quench the system from the melt at the rate of  $10^{15} \text{ K/s}$  to  $50 \text{ K}$ , and then slowly quenched it to  $4 \text{ K}$ , and continued further to  $0 \text{ K}$ . In the second method, the velocity of each atom is equated to zero repeatedly at every time step of an MD simulation and effectively followed the steepest descent trajectory in the phase space for the entire duration of the simulation of the order of  $1 \text{ ns}$ . A better relaxed configuration is achieved by using the second method, with the maximum

remnant force reduced to less than  $10^{-4}$  eV/Å, which is an order of magnitude lower than that found using the first method. The results obtained using the two methods are very similar, and in what follows only those structures simulated using the second method will be described.

### 3.3 Topological Structure

The topological structure of the atomic arrangement in an amorphous material is generally explained in terms of dense random packing [29],[30] and is best described by the radial distribution function (RDF)  $g(r)$ . Experimentally, the RDF of  $\mu$ -Fe has only been investigated for thin films and powder samples. It is probably one of the most significant and interesting properties of pure  $\mu$ -Fe studied both experimentally [9],[29],[30] and by computer simulation [31],[32].

A typical plot of the RDF obtained in the simulations is shown in Figure 3.1 for the density of  $7.88$  g/cm<sup>3</sup>. The blue bars represent the RDF of the corresponding perfect bcc lattice up to the fifth nearest neighbor, with the density of the first nearest neighbor normalized to one. It can be seen that instead of discrete values found for a perfect crystal lattice, distances between neighboring atoms in an amorphous metal are statistically distributed and showed up as broadened peaks. As indicated, the peaks in the RDF of  $\mu$ -Fe are labeled 1a, 1b, 1c, 2a and 2b. Their presence is independent of the size of the simulation cell. The 1a peak is below  $2.31\text{\AA}$ , the 1b and 1c peaks are between  $2.31\text{\AA}$  and  $3.21\text{\AA}$ . The three peaks merge at 300K (Figure 3.1 (b)) showing good agreement with experimental data. The

splitting of the 2<sup>nd</sup> peak (2a & 2b), with 2a peak higher than the 2b peak was proposed to serve as evidence for the formation of an amorphous state [29].

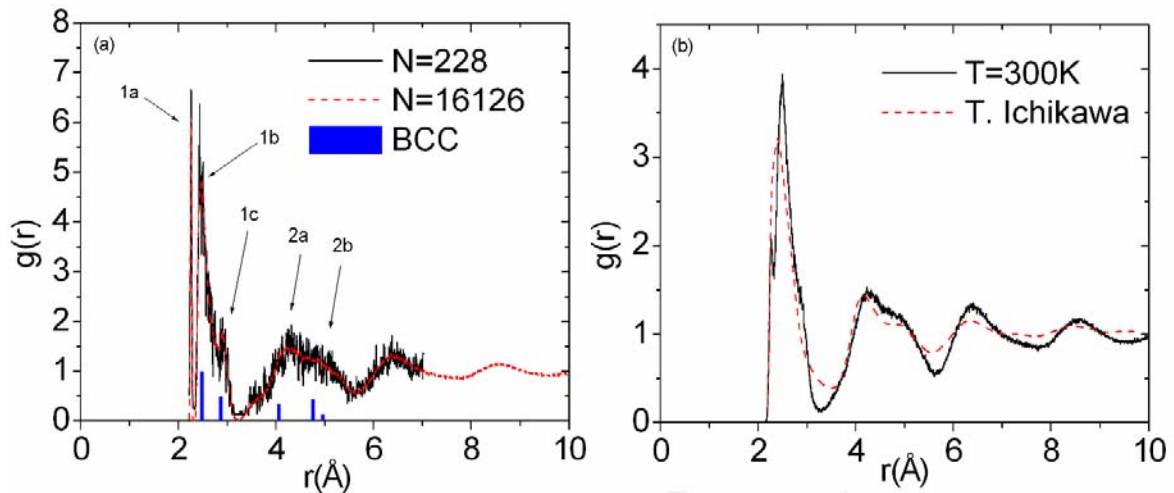


Figure 3.1 – Radial distribution function (RDF)  $g(r)$  of amorphous iron with density =  $7.88 \text{ g/cm}^3$  (a) at  $T = 0K$  and no. of atoms = 288 & no. of atoms = 16126. The blue bars represent the RDF of the corresponding perfect bcc lattice up to fifth nearest neighbors, with the density of first nearest neighbor normalized to one. (b) at  $T = 300K$  and no. of atoms = 16126 & experimental data from T. Ichikawa.

One can observe good correlation between the positions of the 1b, 1c, 2a, 2b peaks in  $\mu\text{-Fe}$  and those of bcc-Fe. On the other hand, there is no such correspondence for the 1a peak. Due to the difficulty with resolving such a narrow peak in finite temperature data, it may be experimentally undetectable even if it existed. Maeda and Takeuchi [31] reported a similar observation of a narrow peak in the RDF, but attributed their finding to an artifact of the Johnson potential. In another calculation using *ab-initio* MD [18], the resulting RDF of  $\mu\text{-Fe}$  did not show the 1a peak. At the same time, that simulation did not show the splitting of the 2<sup>nd</sup> peak either, whereas this should be expected to occur in a real amorphous structure. The relatively low level of resolution of RDF found in *ab-initio* MD

simulations is likely attributable to the small size of the simulation cell. The RDF calculated for other amorphous metals [33]-[36] also show only a single broad peak, without the sharp 1a peak. The fact that *ab-initio* calculations of self-interstitial defect structures in crystalline bcc iron (see below) show that atoms in the core of a defect approach each other as close as 1.95 Å suggests that clusters of atoms separated by very small distances may actually form in amorphous iron.

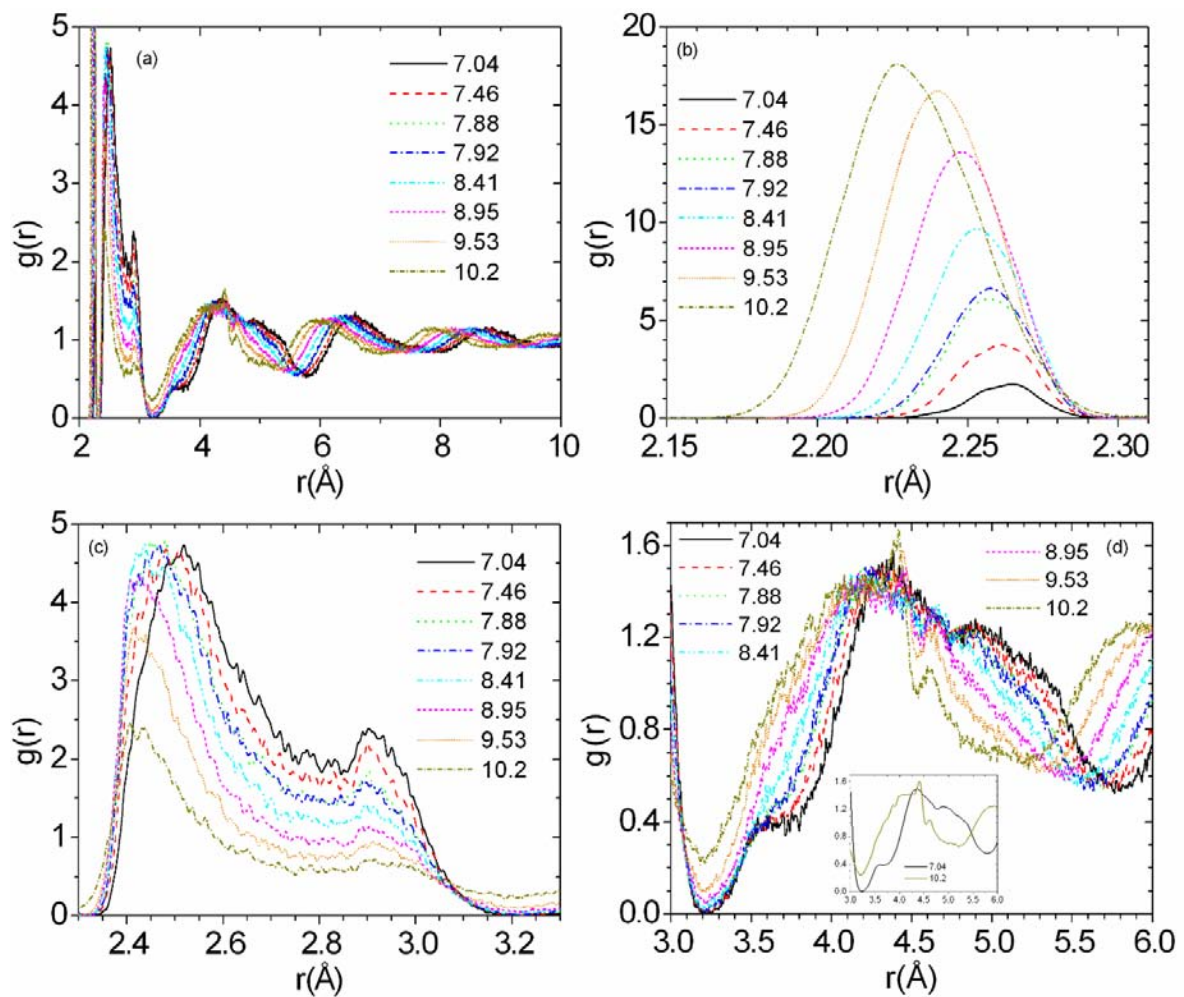


Figure 3.2 – Radial distribution function (RDF)  $g(r)$  of amorphous iron at different densities. (a)  $2 \text{ \AA} < r < 10 \text{ \AA}$  (b)  $2.15 \text{ \AA} < r < 2.31 \text{ \AA}$  (c)  $2.3 \text{ \AA} < r < 3.3 \text{ \AA}$  (d)  $3.0 \text{ \AA} < r < 6.0 \text{ \AA}$

Figure 3.2(a) and (b) show the RDFs and changes in the structure of the 1a

peak for a range of varying densities. The most prominent feature that should be noted is the small width ( $< \sim 0.01$  nm) of the 1a peak, which remains sharp independently of the changes in the density of the material. This probably indicates that neighboring atoms corresponding to this peak are linked into clusters by bonds with a well-defined bond length. As the density increases, the 1a peak grows taller and shifts toward shorter interatomic separation distances, suggesting that the proportion of clustered atoms increases. The increase in the density does not alter the low cutoff value of the RDF that still remains at  $2.31\text{\AA}$ . Figure 3.2(c) shows the corresponding behavior of the 1b and 1c peaks, both of which shrink as the density increases. Figure 3.2(b) and (c) together show that as the density increases, there is a reduction in the proportion of atoms with the neighboring environment of an approximate bcc structure, to feed the simultaneous growth of the proportion of clustered iron atoms. Figure 3.2(d) shows the behavior of the 2a and 2b peaks. Despite similar positions (see Figure 3.1(a)), these peaks do not correspond to the 3<sup>rd</sup> to 5<sup>th</sup> nearest neighbors of the bcc lattice. Indeed, these peaks can be well explained in terms of conventional dense random packing [29],[30]. As the density increases, there is a general shift of the 2a and 2b peaks to smaller interatomic separations, accompanied by changes in the peak structure. It evolves from a structure formed by a superposition of two broad peaks to the one with a single broad peak and two superimposing sharp peaks located at around  $4.40\text{\AA}$  and  $4.61\text{\AA}$ . Smoothened lines for  $7.04\text{g/cm}^3$  and  $10.2\text{ g/cm}^3$  are shown in the insert of Figure 3.2(d). According to Figure 3.2, the effect of an applied hydrostatic stress on the topological structure of the atomic environment of  $\mu$ -Fe extends at least to the 5<sup>th</sup> nearest neighbor distance. Figure 3.3 shows that the percentage of atoms with at

least one neighbor at interatomic separation smaller than  $2.31\text{\AA}$  increases monotonically as a function of density.

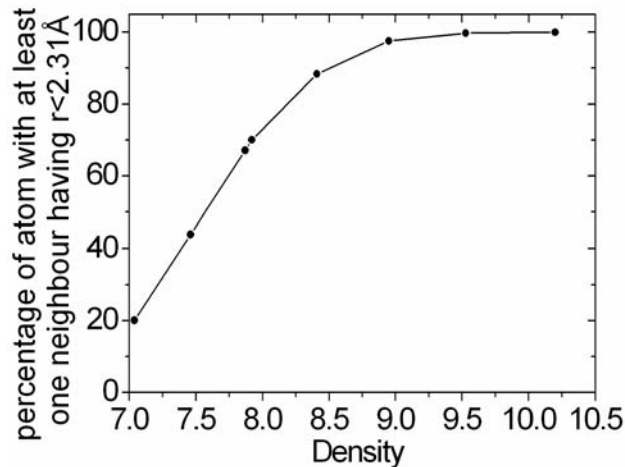


Figure 3.3 – Percentage of atoms for various densities with at least one neighbor with a separation of less than  $2.31\text{\AA}$ .

### 3.4 Magnetic/non-magnetic Transition

To assess the accuracy of simulations performed using the DD potential against *ab-initio* calculations, the structure and the magnitude of magnetic moments are calculated using density functional calculations [37] (Figure 3.4(a)) and compared with the one evaluated using the DD potential (Figure 3.4(b)). Comparison of structures in Figure 3.4(a) and (b) shows that the positions of atoms, as well as the magnitude of magnetic moments predicted by the DD potential agree satisfactorily with those found in *ab-initio* calculations. The self-interstitial  $\langle 110 \rangle$  dumbbell configuration shown in Figure 3.4 represents the most energetically stable, as well as one of the most strongly distorted structures occurring in bcc iron.

The fact that this structure is well described by the semi-empirical magnetic potential used in this work, suggests that the structures and magnetic configurations described below are representative of those of  $\mu$ -Fe.

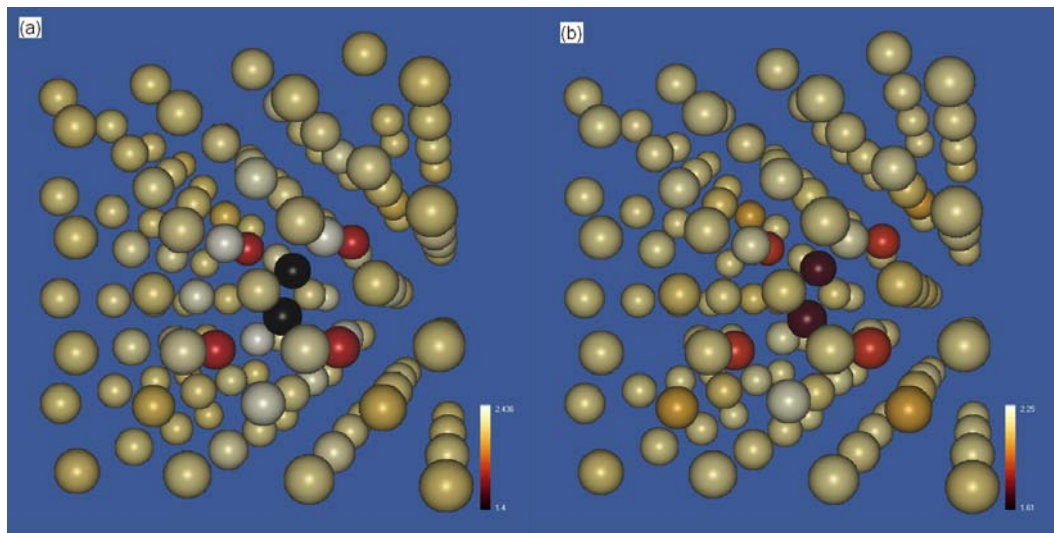


Figure 3.4 – (a) Atomic configuration and magnetic moments for the 110 dumbbell configuration in bcc iron calculated using density functional theory and (b) the same configuration modeled using the magnetic interatomic potential. The differences between (a) and (b) are associated with the approximate treatment of interatomic forces and magnetic moments within the magnetic interatomic potential formalism.

The calculated probability distribution of magnetic moments (MMD) shown in Figure 3.5(a) exhibit a reduction in the mean magnetic moment and broadening of its probability distribution as a function of mass density of  $\mu$ -Fe. This trend agrees very well with results reported in the literature (see e.g. Figure 2 of Ref. [18]). The large scale simulations allow better statistical representation of data and offers clearer view of the trend relating the density of the material and the magnitude of the magnetic moment. Figure 3.5(b) shows the proportion of non-magnetic iron atoms plotted as a function of density, indicating that  $\mu$ -Fe remains magnetic at 0K until the density reaches  $8.41 \text{ g/cm}^3$ , beyond which the

proportion of non-magnetic atoms increases sharply and the sample progressively loses its magnetic properties. At the density of  $10.2 \text{ g/cm}^3$ , practically all the atoms become non-magnetic, completing the magnetic/non-magnetic transition driven by the increasing hydrostatic pressure. The corresponding pressure is shown in the inset of Figure 3.5(b). The pressure is calculated according to virial theorem. At the density of  $8.95 \text{ g/cm}^3$ , the pressure is  $\sim 12.7 \text{ GPa}$ . One can also observe a linear regime in the pressure-density relationship for smaller pressures before the sample gradually loses its magnetism.

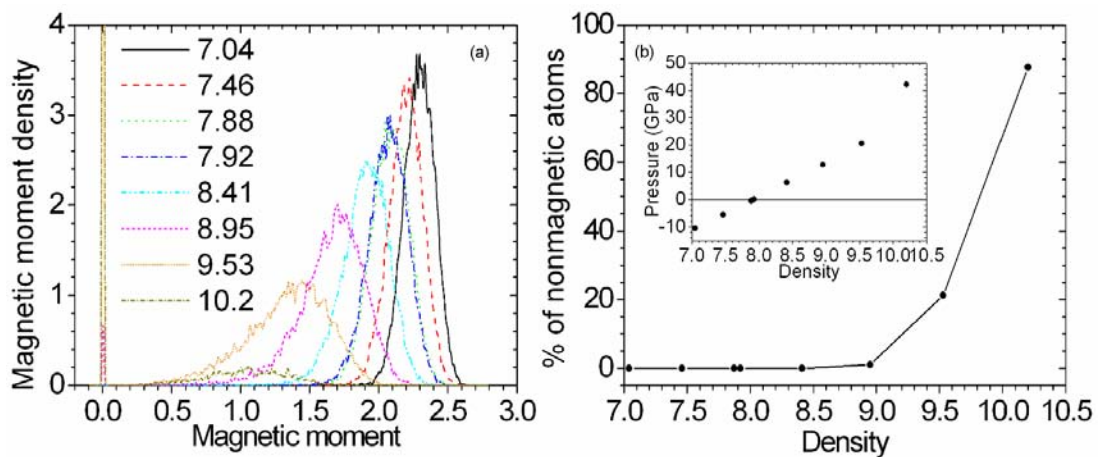


Figure 3.5 – (a) Magnetic moment density versus magnetic moment at different densities. (b) Percentage of nonmagnetic atoms versus density.

Figure 3.6(a) and (b) show the mean and the standard deviation of the MMD as a function of mass density. The figures show plots comparing cases where the non-magnetic atoms were included or excluded from statistical analysis. We see that although there is an overall reduction in the magnetic moment of iron atoms as a function of density, the disappearance of magnetism with increasing density is primarily the result of the sharp increase in the fraction of non-magnetic atoms. The corresponding standard deviation of the MMD in Figure 3.6(b) shows a turning

point at the density of  $9.53 \text{ g/cm}^3$ , where the proportion of magnetic and nonmagnetic atoms is comparable, and it drops again at the density of  $10.2 \text{ g/cm}^3$  where the majority of atoms are non-magnetic. Figure 3.6 shows that  $\mu\text{-Fe}$  loses its magnetic properties gradually as the hydrostatic pressure increases. Similarly to the situation occurring in the core of the self-interstitial defect shown in Figure 3.4(a), the origin of the magnetic/non-magnetic transition is driven by mechanical effects (increase of hydrostatic pressure) and is dissimilar to the temperature-driven order-disorder transition occurring in a ferromagnetic material at the Curie temperature.

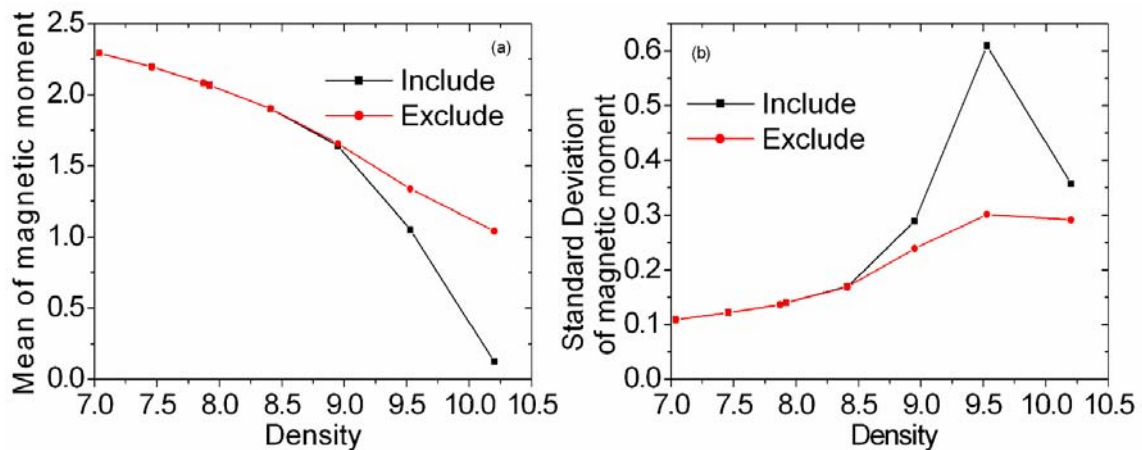


Figure 3.6 – The mean (a) and standard deviation (b) of magnetic moment versus the number density including/excluding atoms with magnetic moment equals to zero.

In Figure 3.7, the magnitude of the magnetic moment of an atom is plotted against its Voronoi volume. The positive correlation seen for all densities does not fully agree Turek and Hafner's result [18] suggesting that the correlation between local volume and magnetic moment ceases to exist in the high density limit. However, only a reduction is observed in this correlation at high pressure, hence making the simulations more consistent with the picture proposed by Krauss and

Krey [19]. The relation between the absolute value of magnetic moment  $M$ , and the Voronoi volume  $V$  in Figure 3.7 can be represented by a best-fit equation  $M = a \ln(V - c) + b$ . The blue line is fitted using all the atoms in the simulation cell. The fitted values are  $a = 0.59147 \pm 0.00125$ ,  $b = 1.42286 \pm 0.00132$ ,  $c = 9.00275 \pm 0.00054$ , and value of the correlation coefficient is 0.80172. The orange line is fitted with the nonmagnetic atoms excluded, and the corresponding fitting parameters are  $a = 0.48479 \pm 0.00084$ ,  $b = 1.65911 \pm 0.00086$ ,  $c = 9.3355 \pm 0.00054$  with the correlation coefficient of 0.82168. The magneto-volume relation for  $\mu$ -Fe is close to that for the antiferromagnetic state in fcc iron, which is consistent with the close-packed structure of this phase [11]. At the same time, one should notice that volume is not the only factor that determines the magnitude of magnetic moment. This is evident from the spatial fluctuations of magnitudes of magnetic moments of individual atoms, which can be very large, particularly near the Voronoi volume of  $9.5 \text{ \AA}^3$  per atom. In this case even for atoms occupying the same Voronoi volume, the magnetic moment can vary from  $0 \mu_B$  to nearly  $2 \mu_B$ .

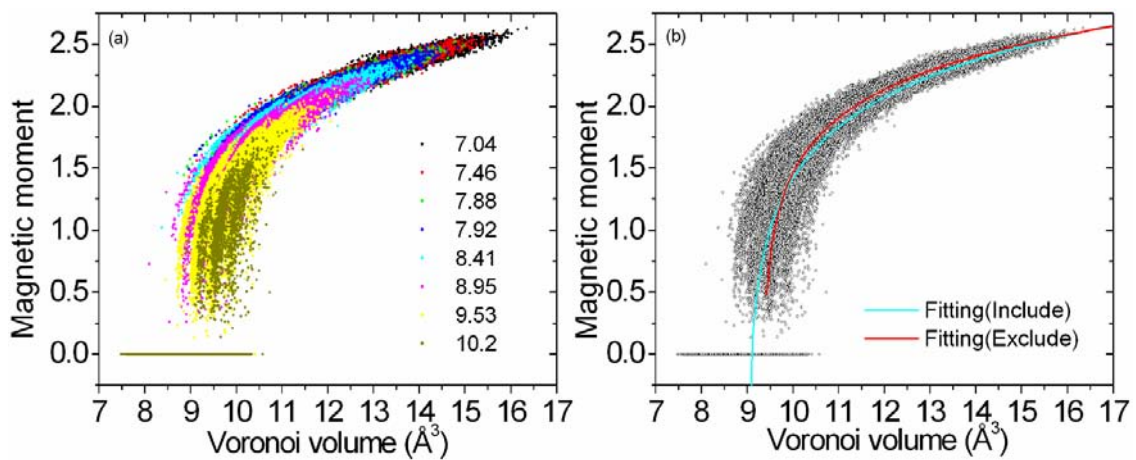


Figure 3.7 – (a) Magnetic moment versus Voronoi volume at different densities. (b) The magnetic moment fitted as a function of the Voronoi volume. The blue line represents

fitting to all atoms and the red line represents fitting without the nonmagnetic atoms.

### 3.5 Relationship between Local Structure and Magnetic Moment

To analyze the effect of local environment on the magnitude of magnetic moment further, Figure 3.8 plotted the mean value of the local magnetic moment as a function of the number of neighbors within the radius of  $3.21\text{\AA}$ . Intuitively, one would expect that as the number of neighbors increases, the mean magnetic moment would decrease due to the higher electron density on an atom. However, Figure 3.8 shows a surprising increase in the mean magnetic moment as the number of neighbors increases. A further examination is done on the respective situations in the 1a, 1b&1c peaks separately, and find that in the 1a peak, the magnetic moment indeed decreases as the number of neighbors increases. In the 1b&1c peaks, on the other hand, the magnetic moment increases with the increasing number of neighbors. Thus, this forced us to also consider the relationship between the Voronoi volume and the number of neighbors of a given atom to arrive at a consistent picture of the magnetic/non-magnetic transition.

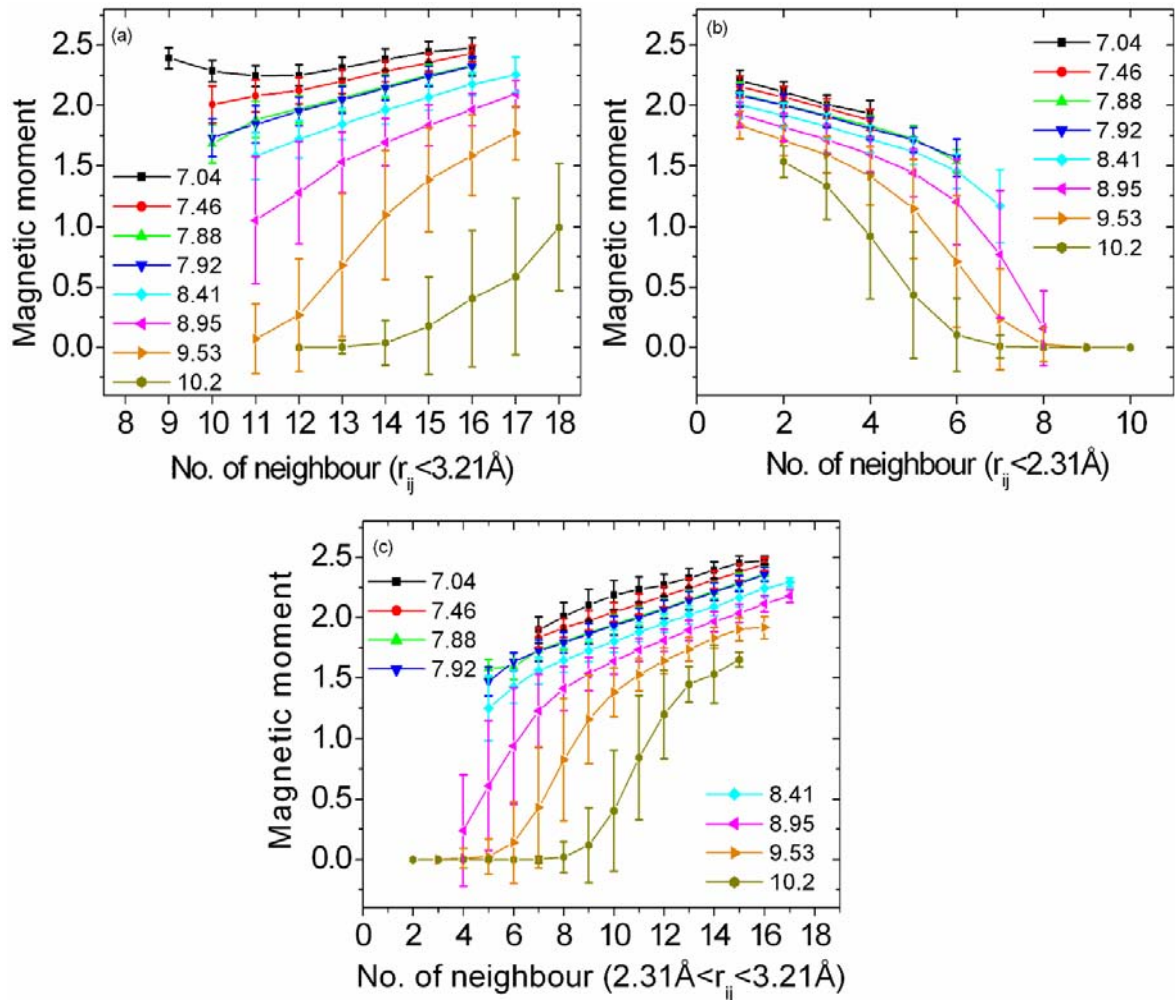


Figure 3.8 – The mean of magnetic moment vs. number of neighbors for (a)  $r_{ij} < 3.21 \text{ \AA}$  (b)  $r_{ij} < 2.31 \text{ \AA}$  (c)  $2.31 \text{ \AA} < r_{ij} < 3.21 \text{ \AA}$

In Figure 3.9, the number of neighbors is plotted versus the Voronoi volume. The figure shows the expected decrease in the Voronoi volume as a function of the number of neighbors in the 1a peak, and the opposite trend for the 1b&1c peaks. It is supposed that owing to their small interatomic separation, iron atoms forming the 1a peak develop local structures characterized by a specific bond length, so that as the number of neighbors increases, the volume occupied by each atom is reduced. On the other hand, atoms in the 1b&1c peak are more loosely bonded *via* the usual metallic bonding mechanism. Atomic positions here are more flexible, i.e. they are

energetically less sensitive to the exact positions of atoms. An additional atom keeping its atomic volume tends to repel other atoms and this causes the Voronoi volume of the centre atom to increase, resulting in a larger size of the local magnetic moment.

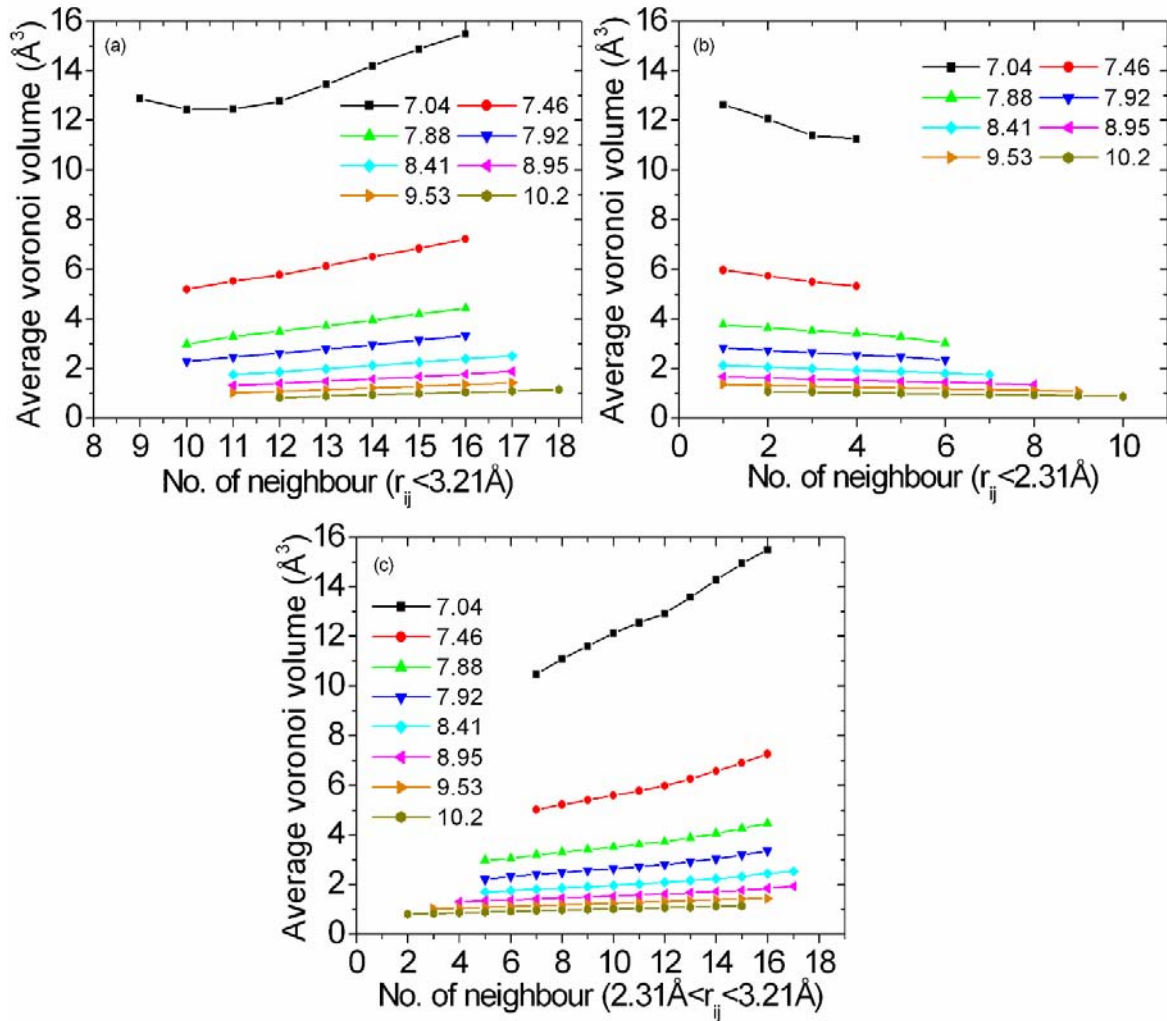


Figure 3.9 – Average Voronoi volume vs. number of neighbors (a)  $r_{ij} < 3.21 \text{ \AA}$  (b)  $r_{ij} < 2.31 \text{ \AA}$  (c)  $2.31 \text{ \AA} < r_{ij} < 3.21 \text{ \AA}$

Figure 3.10(a) shows the statistical distribution of the number of neighbors corresponding to various densities. The curves represent the best fit to Gaussian distributions. The close-to-perfect correlation means that the distribution of the

number of neighbors in amorphous iron is random. The mean number of neighbors versus density shown in Figure 3.10(b) exhibits a linear relationship  $\bar{N} = a + b\rho$  between the mean number of neighbor  $\bar{N}$  and the density  $\rho$ , with  $a = 8.45666 \pm 0.17889$ ,  $b = 0.58613 \pm 0.02109$ , and the correlation coefficient of  $R^2 = 0.99614$ . Using the Johnson's potential, Srolovitz *et al.* [32] observed that structures with 13 neighbors form the largest part of the population. This is similar to our results shown in Figure 3.10(a).

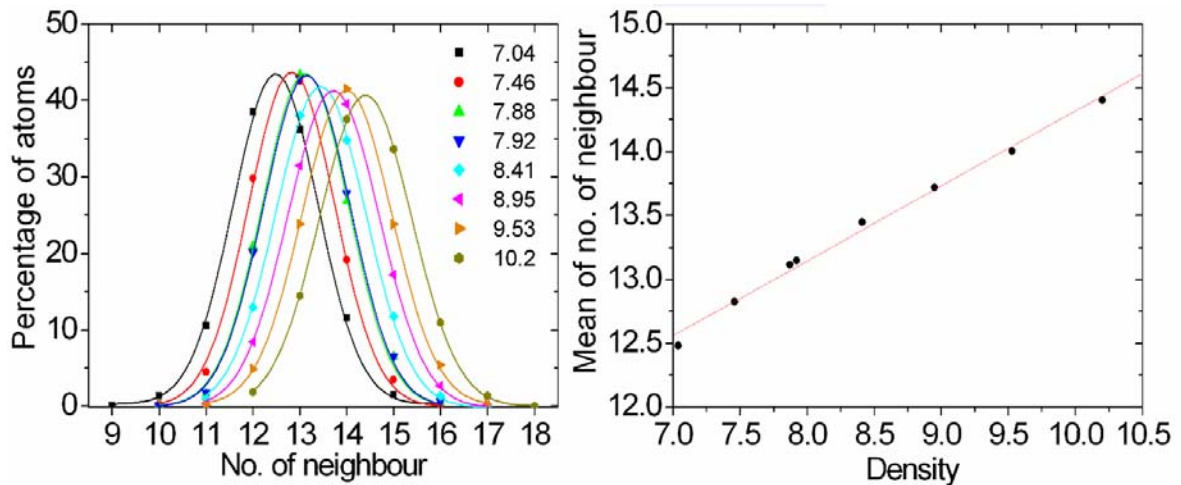


Figure 3.10 – (a) The distribution of number of nearest neighbors at different densities. (b) The mean of the number of neighbors versus density. Red line is the linear fitting.

Figure 3.11(a) shows the magnitude of magnetic moment as a function of the percentage fluctuation of the interatomic separation  $\Delta^{1/2}$ . In comparison with Figure 5 of Ref. [14], the fluctuation of our result is about twice the value reported there. According to the results shown in Figure 3.11(b) the fluctuation varies almost linearly as a function of density.

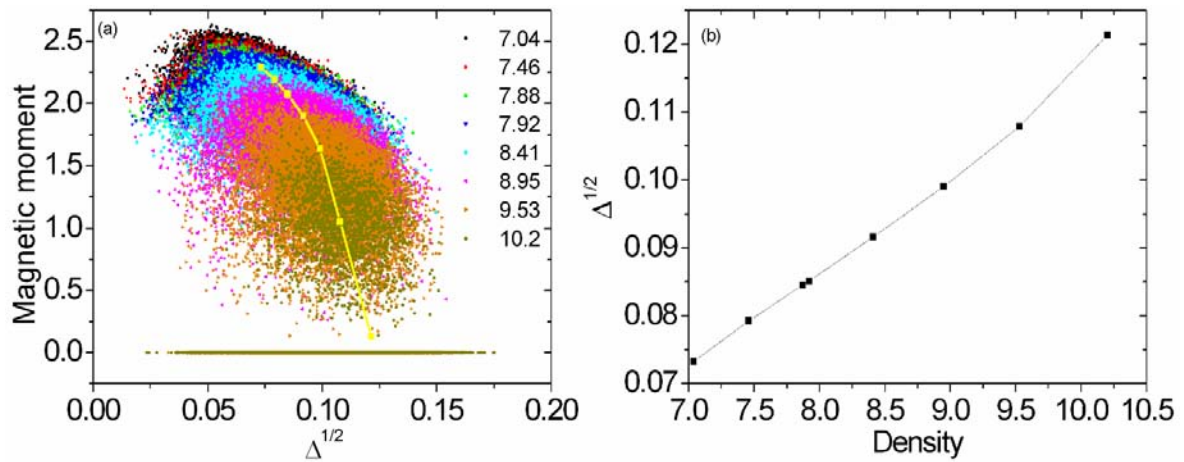


Figure 3.11 – (a) The local magnetic moment versus the local fluctuation of the interatomic separations at different density; the yellow dot is the mean of magnetic moment versus the average fluctuations of interatomic separations  $\Delta^{1/2} = \left\langle (\delta R)^2 \right\rangle^{1/2} / \langle R \rangle$ . (b) The average fluctuations of interatomic distance versus the number densities.

Figure 3.12 shows atomic structures and color-coded magnetic moments of atoms in the simulation cell displayed for several values of the mass density of the material. As the density increases, the number of nonmagnetic (dark) atoms increases and beyond a critical value of mass density the material completely loses its magnetic properties. The structures shown in Figure 3.12 illustrate the fairly complex nature of the magnetic/non-magnetic transition occurring in  $\mu$ -Fe under applied pressure. The origin of the transition from a magnetic to a non-magnetic state is associated with the local widening of the electronic  $d$ -band due to the increase of the local hopping integrals, and the resulting violation of the local Stoner criterion for magnetism [24],[25]. The increase of the amplitude of the local hopping integrals is due to the local deformation of atomic structure such as that occurring in the core region of a self-interstitial atom defect shown in Figure 3.4. In this regard the mechanism of the magnetic/non-magnetic transition observed in the current simulations is entirely different from that of the order-disorder

ferro/paramagnetic transition occurring in crystalline bcc iron at the Curie temperature.

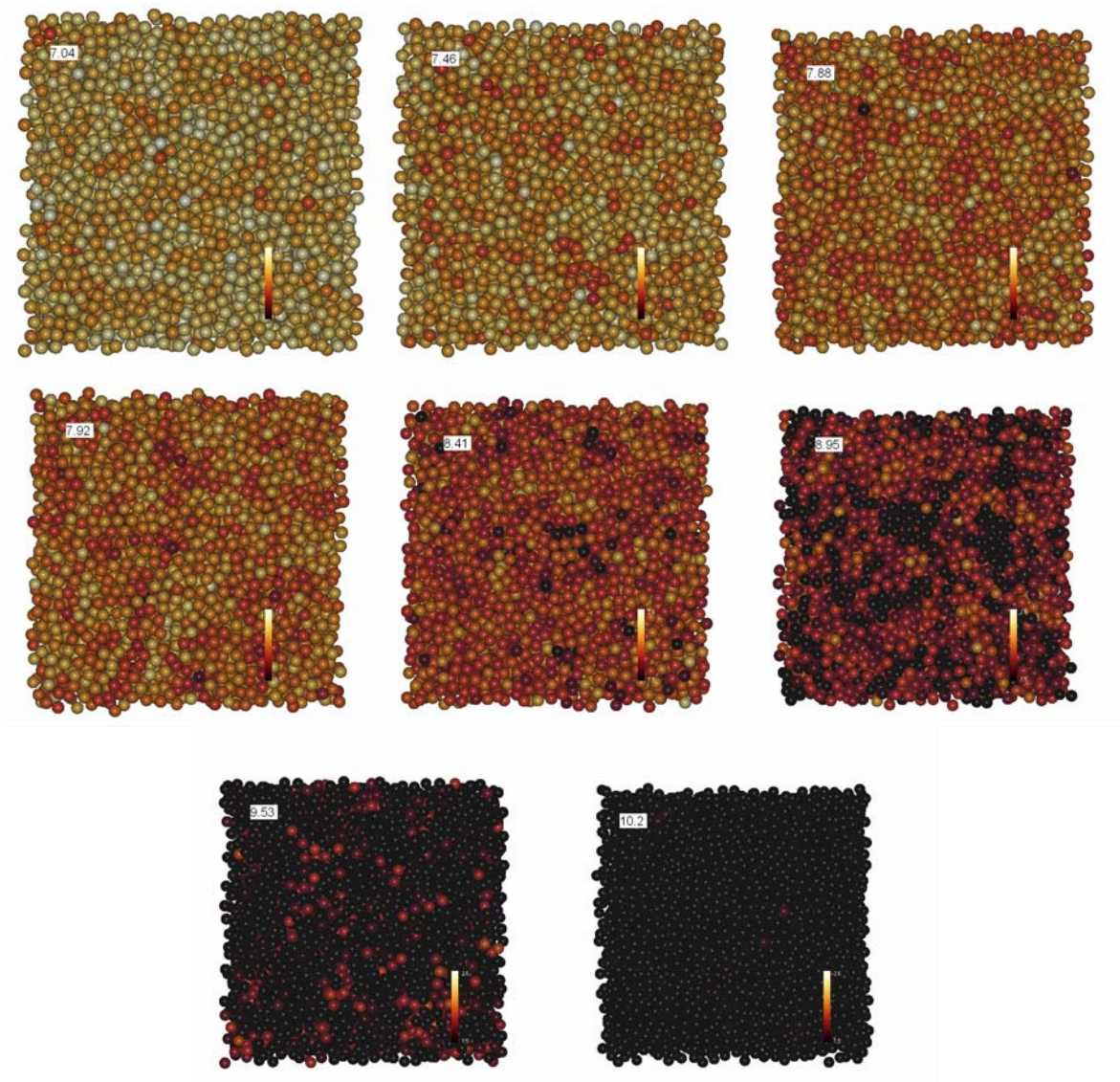


Figure 3.12 – Atomic structures and magnetic moments of atoms simulated using the magnetic potential for systems containing approximately 16 thousand atoms for different values of mass density. Darker color represents atoms with lower magnetic moments. The figure illustrates the gradual nature of the magnetic/non-magnetic transition occurring in amorphous iron under increased external pressure.

There are two possible scenarios for the magnetic/non-magnetic transition, namely that it occurs either *via* inhomogeneous nucleation and growth of a small

number of non-magnetic clusters of atoms, or *via* homogeneous nucleation driven by the uniform increase in the fraction of nonmagnetic atoms in the simulation cell. Those results presented here offer support to the second scenario. Examination of three-dimensional magnetic structure of simulated configurations show that the non-magnetic atoms form largely disconnected clusters, with the loss of magnetic properties driven by local mechanical distortions. To verify this conclusion, a non-magnetic fifteen-atom cluster is added at the centre of the computational cell, and found that this cluster did not grow. Magnetism did not vanish through the growth of nonmagnetic islands, and remained a fluctuating entity throughout the simulation. To what extent this picture is affected by the correlation between magnetic moments driven by inter-atomic exchange remains to be investigated.

### 3.6 Brief Conclusion

Large-scale molecular dynamics simulations were performed to investigate magnetic properties of amorphous iron under external pressure. The simulations were performed using the recently developed magnetic DD interatomic potential. It is found that as the density of the material increased, an increasing fraction of atoms became nonmagnetic. Above a critical density the fraction of nonmagnetic atoms increased sharply, yet homogeneously. The magnetic/non-magnetic transition occurred continuously and homogeneously, and did not involve nucleation and growth of individual non-magnetic clusters. The local magnetic moment density is correlated with the Voronoi volume per atom, and the relation between the two follows a logarithmic law. Evidence was found for the significant

role played by the local atomic environment. However, all the current calculations are limited to zero temperature only. At finite temperature, phonons alone cannot account for all the elementary excitations in a magnetic material. The excitation of magnons and their interactions with the phonons must also be considered. Moreover, the current methodology cannot be used to treat the order/disorder ferro/paramagnetic transition that has a completely different physical origin from the magnetic/non-magnetic transition considered in this chapter. There is as yet no simulation scheme in the literature that can deal with the simultaneous presence of phonons, magnons and their interactions in a unified manner. The usefulness of the MD scheme provides us with the perfect reason to develop a more general simulation scheme that also includes the spin degree of freedom. In the following chapter, a rigorous reformulation of the molecular dynamics simulation for this purpose will be presented, which is entitled Spin-Lattice Dynamics (SLD) simulation.

**REFERENCES**

- [1] T. Kaneyoshi, *Amorphous magnetism*, Chapter 1 & 2 (CRC Press, Inc., United States, 1984)
- [2] R. C. O'Handley, *Modern magnetic materials: principles and applications*, Chapter 10 & 11 (John Wiley & Sons, Inc., United States of America, 2000)
- [3] T. Egami, *Rep. Prog. Phys.* **47**, 1601 (1984)
- [4] G. Xiao and C. L. Chien, *Phys. Rev. B* **35**, 8763 (1987)
- [5] G. Xiao and C. L. Chien, *J. Appl. Phys.* **61**, 3246 (1987)
- [6] D. H. Ryan, L. X. Liao and Z. Altounian, *Sol. Stat. Comm.* **66**, 339 (1988)
- [7] K. S. Suslick, S.-B. Choe, A. A. Cickhowlas and M. W. Grinstaff, *Nature(London)* **353**, 414 (1991)
- [8] M. W. Grinstaff, M. B. Salamon and K. S. Suslick, *Phys. Rev. B* **48**, 269 (1993)
- [9] R. Bellissent, G. Galli, M. W. Grinstaff, P. Migliardo and K. S. Suslick, *Phys. Rev. B* **48**, 15797 (1993)
- [10] G. J. Long, D. Hautot, Q. A. Pankhurst, D. Vandormael, F. Grandjean, J. P. Gaspard, V. Briois, T. Hyeon and K. S. Suslick, *Phys. Rev. B* **57**, 10716 (1998)
- [11] M. Yu and Y. Takehashi, *Phys. Rev. B* **49**, 15723 (1994)
- [12] Y. Takehashi and M. Yu, *Phys. Rev. B* **50**, 6189 (1994)
- [13] Y. Takehashi and M. Yu, *J. Mag. Mag. Mater.* **140**, 255 (1995)
- [14] Y. Takehashi, T. Uchida and M. Yu, *Phys. Rev. B* **56**, 8807 (1997)
- [15] Y. Takehashi, S. Akbar and N. Kimura, *Phys. Rev. B* **57**, 8354 (1998)
- [16] Y. Takehashi and T. Uchida, *J. Phys: Condens. Matter* **12**, 8683 (2000)
- [17] T. Uchida and Y. Takehashi, *Phys. Rev. B* **64**, 054402 (2001)

- [18] I. Turek and J. Hafner, *Phys. Rev. B* **46**, 247 (1992).
- [19] U. Krass and U. Krey, *J. Magn. Magn. Mater.* **98**, L1 (1991).
- [20] U. Krey, U. Krauss and S. Krompiewski, *J. Magn. Magn. Mater.* **103**, 37 (1992)
- [21] R. Lorenz and J. Hafer, *J. Mag. Mag. Mater.* **139**, 209 (1995)
- [22] M. Libes, K. Hummler and M. Fähnle, *Phys. Rev. B* **51**, 8664 (1995)
- [23] M. Libes, and M. Fähnle, *Phys. Rev. B* **53**, 14012 (1996)
- [24] S. L. Dudarev and P. M. Derlet, *J. Phys.: Condens. Matter* **17**, 7097 (2005).
- [25] P. M. Derlet and S. L. Dudarev, *Prog. Mater. Sci.* **52**, 299 (2007); UKAEA Fusion Report **530** (2006) available on [www.fusion.org.uk](http://www.fusion.org.uk)
- [26] M. W. Finnis and J. E. Sinclair, *Phil. Mag.* **50**, 45 (1984)
- [27] M. S. Daw and M. I. Baskes, *Phys. Rev. Lett.* **50**, 1285 (1983)
- [28] M. S. Daw and M. I. Baskes, *Phys. Rev. B* **29**, 6443 (1984)
- [29] T. Ichikawa, *Phys. Stat. Sol. (a)* **19**, 707 (1973).
- [30] G. Shen, M. L. Rivers, S. R. Sutton, N. Sata, V. B. Prakapenka, J. Oxley, K. S. Suslick, *Phys. Earth Planet. Inter.* **143**, 481 (2004)
- [31] K. Maeda and S. Takeuchi, *J. Phys. F: Metal Phys.* **8**, L283 (1978)
- [32] D. Srolovitz, K. Maeda, S. Takeuchi, T. Egami and V. Vitek, *J. Phys. F: Metal Phys.* **11**, 2209 (1981)
- [33] B. E. Clements and D. C. Wallace, *Phys. Rev. E* **59**, 2955 (1999)
- [34] A. Posada-Amarillas, I. L. Garzón, *Phys. Rev. B* **53**, 8363 (1996)
- [35] Q. X. Pei, C. Lu and M. W. Fu, *J. Phys.: Condens. Matter* **16**, 4203 (2004)
- [36] J. L. Feldman, N. Bernstein, D. A. Papaconstantopoulos and M. J. Mehl, *J. Phys.: Condens. Matter* **16**, S5165 (2004)

[37] D. Nguyen-Manh, private communication

# Chapter 4: Spin-Lattice Dynamics

## 4.1 Brief Introduction

The ground state of most materials prefers a non-magnetic state, i.e. the number of spin up electrons is equal to the number of spin down electrons. In the treatment of these materials, the spin character of electrons is usually neglected and does not have significant effect. The eigenvalues  $E_\alpha$  of the corresponding Hamiltonian, which is obtained by solving the Schrödinger equation, would be independent of spins, and so is the density of states

$$D(E) = \sum_{\alpha} \delta(E - E_{\alpha}) \quad (4.1)$$

Here the summation is performed over all the eigenstates  $\{\alpha\}$  of the system. The energy of this system can be trivially evaluated by integrating the density of states up to the Fermi energy.

$$E_{total} = 2 \int^{\varepsilon_F} D(E) dE \quad (4.2)$$

where  $\varepsilon_F$  is the Fermi energy, and the factor of 2 comes from summation over spins. In this case, the only practical problem associated with the evaluation of  $E_{total}$  and with the development of a numerical scheme for MD simulations is in establishing a suitable approximation for  $D(E)$ . This may be accomplished for example by using the tight-binding approximation and the Green's functions approach [1].

However, some materials would prefer magnetic ground state, where magnetism is a collective effect of interacting electrons. In ferromagnetic iron, it is the interacting *d*-character electrons that are mainly responsible for its magnetic nature. For magnetic materials, the treatment in the foregoing presents a much more difficult problem and hence “*few subjects in science are more difficult to understand than magnetism*”<sup>1</sup> [2]. A phenomenological approach is to introduce in the Hamiltonian a Stoner term, specifying the contribution of energy due to the appearance of the atomic magnetic moment [3],[4].

To model the microscopic behavior of iron at a finite temperature, one must include in the treatment not only the interactions between atoms, as usually done in MD, but also those between the electrons in terms of their spins. As mentioned in earlier chapters, the interaction between the electron spins in the case of an itinerant magnetic material like ferromagnetic iron can be taken into account *via* the concept of atomic spins. In this context, ferromagnetic iron can be modeled on the basis of an ensemble of interacting classical particles with interacting intrinsic spins.

In this chapter, a simulation scheme is proposed where the lattice dynamics (or molecular dynamics) and spin dynamics are unified into a single simulation scheme, and hence the name Spin-Lattice Dynamics (SLD). The atoms of ferromagnetic iron, modeled as classical particles with intrinsic spins, interact *via* scalar many-body forces as well as *via* spin-dependent forces of the Heisenberg form. At the same time, the spins interact *via* a coordinate-dependent exchange function. This extends the existing magnetic-potential treatment to the case where

---

<sup>1</sup> Encyclopedia Britannica, 15th Edition, 1989

the strength of interaction between the atoms depends on the relative orientations of their non-collinear spins, and couples the spin and lattice subsystems. Instead of only treating close systems, the spin temperature is introduced *via* the fluctuation-dissipation theorem (FDT). Following the framework established by Brown [5], one can derive the relationship between the dissipative coefficient and random forces, as in the case of the lattice (equation 2.18). The integration algorithm for SLD would also be presented. Similar to the case without spins, the 2<sup>nd</sup> order Suzuki-Trotter decomposition (STD) is adopted, in order to minimize numerical energy dissipation.

## 4.2 Hamiltonian

For a system of  $N$  magnetic atoms, the total “potential” energy is a function of positions  $\{\mathbf{R}_k\}$  of atoms and their vector magnetic moments  $\{\mathbf{M}_k\}$ . Since the quantum mechanical Hamiltonian of the system is invariant with respect to the choice of the spin quantization axis, the energy must also be invariant with respect to the choice of this axis. A sufficiently general expression satisfying this invariance principle is [4]

$$\begin{aligned}
 E(\{\mathbf{R}_k\}, \{\mathbf{M}_k\}) &= E^{(0)}(\{\mathbf{R}_k\}) + \sum_i E^{(1)}(\{\mathbf{R}_k\}) \mathbf{M}_i^2 \\
 &\quad + \sum_i E^{(2)}(\{\mathbf{R}_k\}) (\mathbf{M}_i^2)^2 \\
 &\quad + \sum_{i,j} E^{(3)}(\{\mathbf{R}_k\}) \mathbf{M}_i \cdot \mathbf{M}_j + L
 \end{aligned} \tag{4.3}$$

The first three terms in the above expansion can be grouped together and

incorporated into a single many-body potential term, which can be treated as a “scalar” component of the energy, independent of the orientations of the atomic spins. The last term is the lowest-order exchange coupling term. By minimizing the energy with respect to the magnitude of the magnetic moments, eliminating in this way the high-energy part of the spectrum of electronic excitations, and by retaining only the lowest order exchange coupling term, the above equation can be written in as [4]:

$$E(\{\mathbf{R}_k\}, \{\mathbf{e}_k\}) = U(\{\mathbf{R}_k\}) - \frac{1}{2} \sum_{i,j} J_{ij}(\{\mathbf{R}_k\}) \mathbf{e}_i \cdot \mathbf{e}_j \quad (4.4)$$

where  $\mathbf{e}_k$  is a unit vector of atomic spin direction, and the magnitude of the magnetic moments is absorbed in the definition of the exchange function  $J_{ij}(\{\mathbf{R}_k\})$ .

The corresponding effective classical Hamiltonian can now be written as [6]-[9]:

$$H = \sum_i \frac{\mathbf{p}_i^2}{2m_i} + U - \frac{1}{2} \sum_{\substack{i,j \\ i \neq j}} J_{ij} \mathbf{e}_i \cdot \mathbf{e}_j \quad (4.5)$$

This classical Hamiltonian treats the lattice and spin degrees of freedom as coupled subsystems. The third term describes the coupling between atomic spins due to the exchange interaction, which can be considered as an inter-atomic potential depending on the relative spin-orientation [10]. Low-energy elementary excitations of a system of interacting classical particles arranged in a crystal lattice take the form of lattice waves or phonons, originating from the atomic vibrations about their

zero-temperature positions. Similarly, low-energy excitations in a system of atomic spins take the form of spin waves or magnons, originating from the oscillation of the atomic spins directions about their zero-temperature collinear directions. Thus, low-energy excitations of a ferromagnetic crystal like bcc-iron must include the interaction among the phonons and magnons, i.e., the interacting lattice and spin waves, as governed by the spin-lattice dynamics. This picture explains the problems of the mean-field Stoner model [11] that does not include the low-energy collective magnetic excitations. It also highlights the limitations of models in which the lattice dynamics and the spin dynamics are taken as independent and linearly additive.

To facilitate discussion, the third term of equation 4.5 is given the name spin-potential, as opposed to the usual many-body inter-atomic potential  $U$  describing the “scalar” interaction between the atoms. The dynamics of the system is now 8-dimensional, since in addition to the 6 degrees of freedom per atom in the coordinate and linear momentum space, we now have two additional degrees of freedom (i.e.  $\theta$  and  $\phi$ ) for the direction of its spin. One can note that the spin-potential is a function of the relative spin orientation, and in a general case it is also a many-body function of atomic positions. Since an accepted method to derive the functional form of this potential from a many-body quantum Hamiltonian is not yet available [4], the following approximation is used:

$$\begin{aligned}
 H &= \sum_i \frac{\mathbf{p}_i^2}{2m_i} + H_{DD} + (H_{spin} - H_{spin}^{ground}) \\
 &= \sum_i \frac{\mathbf{p}_i^2}{2m_i} + H_{DD} - \frac{1}{2} \sum_{i,j} J_{ij} (\mathbf{e}_i \cdot \mathbf{e}_j - 1)
 \end{aligned} \tag{4.6}$$

where the first term is the kinetic energy of the atoms,  $H_{DD}$  is the DD magnetic potential [12],  $H_{spin} = -(1/2) \sum_{i,j} J_{ij} \mathbf{e}_i \cdot \mathbf{e}_j$  is the spin Hamiltonian, and  $H_{spin}^{ground}$  is the ground state energy for the collinear spin subsystem at 0K. Using this notation, one can write  $U = H_{DD} + (1/2) \sum_{i,j} J_{ij}$ . The functional form of Hamiltonian in equation 4.6 ensures that the energy and the atomic forces are correctly defined at 0K.

### 4.3 Exchange Function

In fixed lattice models, i.e., when lattice vibrations are neglected, the exchange function  $J_{ij}$  is given by a set of discrete values corresponding to a fixed set of inter-atomic distances for a particular lattice [10],[13]. In the current formulation, it is treated as a continuous function of atomic positions [9],[14]. Here  $J_{ij}$  is expressed as a pairwise function of inter-atomic separations and treated as a mid- to long-range part of the Bethe-Slater curve [15]. Using *ab-initio* calculations, Morán *et al.* [16] and Sabiryanov *et al.* [17] investigated how the exchange function varied as a function of inter-atomic distance. The parameterization of  $J_{ij}$  in this work is obtained by fitting to the data given in Table 1 of Ref. [16] and in Figure 2 of Ref. [17].

Our fitting strategy followed the convention where the dependence of the potential on the distance between the atoms  $r_{ij} = |\mathbf{R}_i - \mathbf{R}_j|$  is described by a sum of third-order polynomials:

$$f(r_{ij}) = \sum_{n=1}^N f^n (1 - r_{ij}/r_c)^3 \Theta(r_c^n - r_{ij}) \quad (4.7)$$

where  $r_c^n$  is the cut-off distance for the  $n^{\text{th}}$  polynomial,  $f^n$  is the  $n^{\text{th}}$  polynomial expansion coefficient, and  $\Theta(r_c^n - r_{ij})$  is the Heaviside step function. Given the approximate nature of the fit and the pairwise representation for the exchange function, only a single polynomial is used, so that

$$J_{ij}(r_{ij}) = J_0 (1 - r_{ij}/r_c)^3 \Theta(r_c - r_{ij}) \quad (4.8)$$

The cut-off radius  $r_c = 3.75 \text{ \AA}$  is chosen to locate between the second and the third nearest neighbor distance for bcc iron.

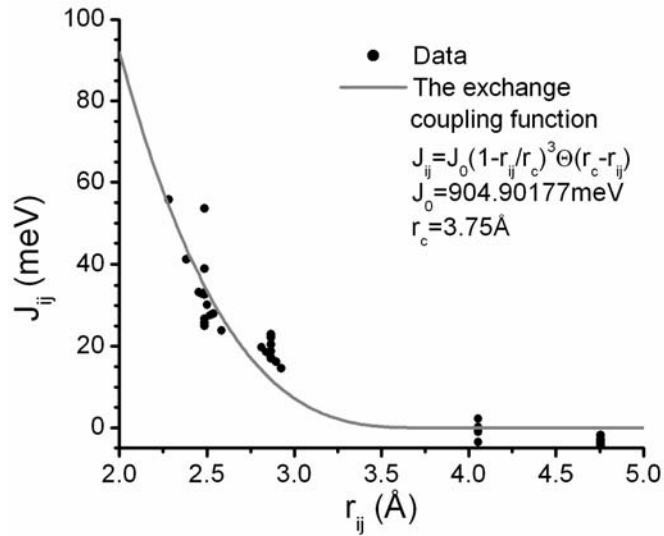


Figure 4.1 – Exchange function  $J_{ij}$  shown as a function of interatomic distance  $r_{ij}$  and compared with data taken from Ref. [16] and Ref. [17]. The assumed form for the exchange function is  $J_{ij}(r_{ij}) = J_0 (1 - r_{ij}/r_c)^3 \Theta(r_c - r_{ij})$ , where  $J_0 = 904.90177 \text{ meV}$  and  $r_c = 3.75 \text{ \AA}$ .

Figure 4.1 shows the fitted curve for  $J_0 = 904.90177 \text{ eV}$ , and the original data

points taken from Ref. [16] and [17]. The fitted curve is likely to become fairly inaccurate in the limit of small interatomic separations. However, it is hard to investigate this point here because of the lack of *ab-initio* data describing this limit. A more accurate representation for  $J_{ij}$  can be implemented once more extensive *ab-initio* data and more accurate functional forms for  $J_{ij}$  become available. Indeed,  $J_{ij}$  should also be a function of the *electronic* temperature since thermal excitations affect the Fermi-Dirac statistics of electrons and alter the equilibrium magnitudes of magnetic moments.

#### 4.4 Equations of Motion

The equations of motion for the atoms and the spins can be derived using the method of Poisson brackets [9] or by adopting the classical equation of motion for the undamped magnetization field [18],[19]. To use the Poisson brackets, one should consider the *actual* atomic spins  $\mathbf{S}_k$ , rather than the unit direction vectors  $\mathbf{e}_k$ . Starting from the atomic spin Hamiltonian,

$$H_A = -\frac{1}{2} \sum_{i,j} J_{ij}^A \mathbf{S}_i \cdot \mathbf{S}_j, \quad (4.9)$$

one can derive the equation of motion for  $\mathbf{S}_k$  as

$$\frac{d\mathbf{S}_k}{dt} = \frac{i}{\hbar} [H_A, \mathbf{S}_k] = \frac{-1}{\hbar} \left( \sum_i J_{ik}^A \mathbf{S}_i \right) \times \mathbf{S}_k \quad (4.10)$$

Comparing  $H_A$  and  $H_{spin}$ , the above equation becomes

$$\begin{aligned} S_k \frac{d\mathbf{e}_k}{dt} &= \frac{-1}{\hbar} \left( \sum_i J_{ik} \mathbf{e}_i \right) \times \mathbf{e}_k \\ \Rightarrow \Pi_k \frac{d\mathbf{e}_k}{dt} &= \mathbf{e}_k \times \left( \sum_i J_{ik} \mathbf{e}_i \right) \end{aligned} \quad (4.11)$$

where  $\Pi_k = \hbar S_k = \frac{\hbar M_k}{g \mu_B}$ , and the g-factor is taken as a positive quantity.  $M_k$  is

the magnitude of an atomic magnetic moment, which we can evaluate directly from the DD potential [20].

Equation 4.11 is derived quantum mechanically using the Heisenberg operator formalism. In the classical limit, i.e. when the magnitude of atomic spin  $\Pi_k$  is many times the spin of a single electron, the system of atoms and spins evolves along the classical trajectories. For ferromagnetic iron at 0K,  $M_k \approx 2.2\mu_B$ , which is not much greater than 1. We can expect that quantum effects would be significant, but will be neglected if the approximation of classical spin is adopted. However, for the purpose of the present thesis, we may assume that classical spin is sufficient to give us insights on the coupled spin and lattice subsystems.

One may also note that the equations of motion for the spin subsystem differ by a factor of  $\Pi_k$  from those derived by Omelyan *et al.* [6]-[8] and by Tsai *et al.* [21],[22], who also used the Poisson bracket approach. This difference is significant since the precession frequency depends on  $\Pi_k$  in a way analogous to the dependence of the acceleration of a particle on its mass. To confirm the accuracy of our equations, an independent alternative derivation is performed, by

starting from the classical equation of motion for the undamped magnetization field [18],[19],

$$\frac{d\mathbf{M}_k}{dt} = -\gamma(\mathbf{M}_k \times \mathbf{H}'_k) \quad (4.12)$$

where  $\gamma = \frac{g\mu_B}{\hbar}$  is the gyromagnetic ratio and  $\mathbf{H}'_k = -\frac{\delta H_M}{\delta \mathbf{M}_k}$  is the effective field.

The Hamiltonian for the effective magnetic moment is:

$$H_M = -\frac{1}{2} \sum_{i,j} J_{ij}^M \mathbf{M}_i \cdot \mathbf{M}_j, \quad (4.13)$$

from which it follows that

$$\frac{d\mathbf{M}_k}{dt} = -\gamma \left( \mathbf{M}_k \times \sum_i J_{ik}^M \mathbf{M}_i \right) \quad (4.14)$$

Comparing  $H_M$  and  $H_{spin}$  and taking into account that the direction of the magnetic moment is opposite to that of the atomic spin, equation 4.14 is transformed to:

$$\begin{aligned} \left( \frac{M_k}{\gamma} \right) \frac{d\mathbf{e}_k}{dt} &= \left( \mathbf{e}_k \times \sum_i J_{ik} \mathbf{e}_i \right) \\ \Rightarrow \Pi_K \frac{d\mathbf{e}_k}{dt} &= \left( \mathbf{e}_k \times \sum_i J_{ik} \mathbf{e}_i \right) \end{aligned} \quad (4.15)$$

which is the same as equation 4.11.

The final equations of motion for the atoms and their spins are given by

$$\begin{cases} \frac{d\mathbf{R}_k}{dt} = \frac{\partial H}{\partial \mathbf{p}_k} = \frac{\mathbf{p}_k}{m_k} \\ \frac{d\mathbf{p}_k}{dt} = -\frac{\partial H}{\partial \mathbf{R}_k} = -\frac{\partial U}{\partial \mathbf{R}_k} + \frac{1}{2} \sum_{i,j} \frac{\partial J_{ij}}{\partial \mathbf{R}_k} (\mathbf{e}_i \cdot \mathbf{e}_j) \end{cases} \quad (4.16)$$

and

$$\Pi_k \frac{d\mathbf{e}_k}{dt} = \mathbf{e}_k \times \mathbf{H}_k \quad (4.17)$$

where  $\mathbf{H}_k = \sum_i J_{ik} \mathbf{e}_i$  is the effective exchange vector field acting on spin  $k$ .  $\Pi_k$  plays the role of moment of inertia for the dynamics of angular motion of the spin vector. Equations 4.16 and 4.17 show that the dynamics of the lattice and spin subsystems are explicitly coupled through the dependence of  $J_{ij}$  on the atomic positions  $\{\mathbf{R}_k\}$  via the gradient term  $\partial J_{ij} / \partial \mathbf{R}_k$  in equation 4.16 and the  $J_{ij}$  term in equation 4.17. Note that the formulation in the foregoing does not take into account the spin-orbit coupling between the lattice and the spin subsystems.

## 4.5 Conservation Laws

The equations of motion derived in the foregoing is for a closed system and must satisfy the total energy and total angular momentum conservation laws. Let us first consider energy conservation. In this case, the time derivative of the total energy from equation 4.5 is:

$$\begin{aligned} \frac{dE}{dt} &= \sum_k \frac{\mathbf{p}_k}{m_k} \frac{d\mathbf{p}_k}{dt} + \sum_k \frac{\partial U}{\partial \mathbf{R}_k} \frac{d\mathbf{R}_k}{dt} \\ &\quad - \frac{1}{2} \sum_{i,j} \sum_k \frac{\partial J_{ij}}{\partial \mathbf{R}_k} \frac{d\mathbf{R}_k}{dt} (\mathbf{e}_i \cdot \mathbf{e}_j) - \frac{1}{2} \sum_{i,j} J_{ij} \frac{d}{dt} (\mathbf{e}_i \cdot \mathbf{e}_j) \end{aligned} \quad (4.18)$$

Grouping the 2<sup>nd</sup> and the 3<sup>rd</sup> terms together, we have

$$\begin{aligned} \frac{dE}{dt} &= \sum_k \frac{\mathbf{p}_k}{m_k} \frac{d\mathbf{p}_k}{dt} + \sum_k \left[ \frac{\partial U}{\partial \mathbf{R}_k} - \frac{1}{2} \sum_{i,j} \frac{\partial J_{ij}}{\partial \mathbf{R}_k} (\mathbf{e}_i \cdot \mathbf{e}_j) \right] \frac{d\mathbf{R}_k}{dt} \\ &\quad - \frac{1}{2} \sum_{i,j} J_{ij} \frac{d}{dt} (\mathbf{e}_i \cdot \mathbf{e}_j) \end{aligned} \quad (4.19)$$

The expression in square brackets in this equation is the negative of the right-hand side of the equation describing the evolution of the momentum (Equation 4.16), and  $d\mathbf{R}_k/dt = \mathbf{p}_k/m_k$ . Therefore, only the last term remains, i.e.,

$$\frac{dE}{dt} = -\frac{1}{2} \sum_{i,j} J_{ij} \frac{d}{dt} (\mathbf{e}_i \cdot \mathbf{e}_j) \quad (4.20)$$

Now,

$$\begin{aligned} \sum_{i,j} J_{ij} \frac{d}{dt} (\mathbf{e}_i \cdot \mathbf{e}_j) &= \sum_{i,j} J_{ij} \left[ \mathbf{e}_i \cdot \frac{d\mathbf{e}_j}{dt} + \frac{d\mathbf{e}_i}{dt} \cdot \mathbf{e}_j \right] \\ &= \sum_{i,j} J_{ij} \left[ \mathbf{e}_i \cdot \frac{1}{\Pi_j} \mathbf{e}_j \times \mathbf{H}_j + \frac{1}{\Pi_i} \mathbf{e}_i \times \mathbf{H}_i \cdot \mathbf{e}_j \right] \end{aligned} \quad (4.21)$$

The exchange function is symmetric, i.e.  $J_{ij} = J_{ji}$ .

$$\begin{aligned}
\sum_{i,j} J_{ij} \frac{d}{dt} (\mathbf{e}_i \cdot \mathbf{e}_j) &= \sum_{i,j} \frac{2}{\Pi_j} J_{ij} [\mathbf{e}_i \cdot \mathbf{e}_j \times \mathbf{H}_j] \\
&= \sum_{i,j} \frac{2}{\Pi_j} J_{ij} \left[ \mathbf{e}_i \cdot \mathbf{e}_j \times \sum_k J_{kj} \mathbf{e}_k \right] \\
&= \sum_j \frac{2}{\Pi_j} \left[ \left( \sum_i J_{ij} \mathbf{e}_i \right) \cdot \mathbf{e}_j \times \left( \sum_k J_{kj} \mathbf{e}_k \right) \right] \\
&= 0
\end{aligned} \tag{4.22}$$

because  $\sum_i J_{ij} \mathbf{e}_i = \sum_k J_{kj} \mathbf{e}_k$  and for any arbitrary two vectors  $\mathbf{A} \cdot [\mathbf{B} \times \mathbf{A}] = 0$ . Thus, the total energy is conserved, and remains constant while the individual energies of the lattice or the spin subsystems separately vary as functions of time.

Similarly, by considering the time derivative of the total angular momentum of the system  $\sum_i \Pi_i \mathbf{e}_i$ , one can show that for pure spin dynamics this quantity is also conserved. This can be proved by a series of transformations involving the transposition of summation indices, namely

$$\begin{aligned}
\frac{d}{dt} \sum_i \Pi_i \mathbf{e}_i(t) &= \sum_{i,j} J_{ji} (\mathbf{e}_i \times \mathbf{e}_j) = \sum_{i,j} J_{ji} (\mathbf{e}_j \times \mathbf{e}_i) \\
&= -\sum_{i,j} J_{ij} (\mathbf{e}_i \times \mathbf{e}_j) = -\sum_{i,j} J_{ji} (\mathbf{e}_i \times \mathbf{e}_j) = 0
\end{aligned} \tag{4.23}$$

where  $J_{ij} = J_{ji}$  and that for any two vectors  $\mathbf{A}$  and  $\mathbf{B}$  their vector product changes sign if the vectors are transposed  $\mathbf{A} \times \mathbf{B} = -\mathbf{B} \times \mathbf{A}$ .

## 4.6 Spin Temperature

Total angular momentum conservation imposes an unusually severe constraint on the dynamics of the spin system. Considering the case where initially the atomic spins are completely collinear, conservation of energy and angular momentum requires the spins to remain permanently collinear and cannot respond to changes of lattice vibration despite the coupling provided by the Hamiltonian, thus ruling out the dependence of magnetization as a function of temperature. Numerical studies performed for a microcanonical ensemble and described in the coming chapters indeed confirm this behavior. In terms of the general methodology of atomistic simulations, this is very unusual. To avoid complications with temperature control in MD simulations, microcanonical simulations for a very large system is generally believed to be the strategy to maintain best accuracy. Constraints due to angular momentum conservation thus rule out fundamentally the application of this strategy to SLD. In this regard, the dynamics of a large closed system of interacting spins is fundamentally different from the dynamics of a large closed system of interacting atoms, where inter-atomic interactions ultimately result in the statistical equilibration of positions and velocities asymptotically.

In order to perform a simulation of a non-isolated system, a method for controlling the temperature of the system has to be developed. The fact that the SLD equations conserve both the total energy and spin angular momentum shows that interaction between a system of magnetic atoms and the environment (i.e. the thermal bath or the thermal reservoir) has to involve both dynamic quantities. To facilitate the interchange of the spin angular momentum, it is necessary to

introduce the notion of spin temperature. In this regard, the deterministic spin dynamics equation (Equation 4.17) is replaced by the stochastic Langevin-type equations of the form [5],[23]:

$$\Pi_k \frac{d\mathbf{e}_k}{dt} = \left[ \mathbf{e}_k \times (\mathbf{H}_k + \mathbf{h}_k) - \eta \mathbf{e}_k \times (\mathbf{e}_k \times \mathbf{H}_k) \right] \quad (4.24)$$

where  $\mathbf{h}_k$  is a delta-correlated random fluctuation of the field  $\mathbf{H}_k$ , satisfying the condition:

$$\langle h_i(t') h_j(t'') \rangle = \mu \delta_{ij} \delta(t' - t'') \quad (4.25)$$

where  $\mu$  is the amplitude of the random noise, and indices  $i$  and  $j$  denote the Cartesian  $x$ ,  $y$ ,  $z$  coordinates. In equation 4.24,  $\eta$  is a dimensionless damping constant, which together with the random fluctuation  $\mathbf{h}_k$  describe the interaction between the spin subsystem and the thermostat, and the resulting exchange of energy and the angular momentum between the spin subsystem and the thermodynamic reservoir. Note that with equation 4.24, the spin angular momentum is no longer conserved.

The temperature of the spin subsystem is then defined by applying the fluctuation-dissipation theorem (FDT) [24],[25]. FDT introduces temperature *via* a relationship between the systematic and random forces, which indeed comes from the same origin. Since the random fluctuation  $\mathbf{h}_k$  is assumed to be Gaussian and Markoffian, the stochastic equation 4.24 can be mapped into the Fokker-Planck equation [25]:

$$\frac{\partial P}{\partial t} = -\frac{\partial}{\partial x_i}(A_i P) + \frac{1}{2} \frac{\partial^2}{\partial x_i \partial x_j}(B_{ij} P) \quad (4.26)$$

where  $x_1 = \theta$ ,  $x_2 = \phi$  and  $P(\theta, \phi, t)$  is the probability distribution function of energy at time  $t$ . The parameters  $A_i = \lim_{\Delta t \rightarrow 0} \frac{1}{\Delta t} \langle \Delta x_i \rangle$  and  $B_{ij} = \lim_{\Delta t \rightarrow 0} \frac{1}{\Delta t} \langle \Delta x_i \Delta x_j \rangle$  are the drift and diffusion coefficients in probability space, respectively, which can be obtained following the procedure described by Brown [5]:

$$\begin{aligned} A_\theta &= \frac{1}{\Pi_k} \left( \frac{1}{\sin \theta} \frac{\partial E_k}{\partial \phi} - \eta \frac{\partial E_k}{\partial \theta} \right) + \frac{\mu}{2\Pi_k^2} \cot \theta \\ A_\phi &= \frac{1}{\Pi_k} \left( \frac{-1}{\sin \theta} \frac{\partial E_k}{\partial \theta} - \frac{\eta}{\sin^2 \theta} \frac{\partial E_k}{\partial \phi} \right) \\ B_{\theta\theta} &= \frac{1}{\Pi_k} \mu \\ B_{\phi\phi} &= \frac{1}{\Pi_k^2} \mu \csc^2 \theta \\ B_{\theta\phi} &= B_{\phi\theta} = 0 \end{aligned} \quad (4.27)$$

where  $E_k = -\mathbf{H}_k \cdot \mathbf{e}_k$ .

In thermodynamic equilibrium (i.e.  $\partial W / \partial t = 0$ ), one can identify the energy distribution of the spin subsystem with the Gibbs distribution. i.e.

$$W = W_0 \exp\left(-\frac{E}{k_B T}\right) \quad (4.28)$$

Since the unit surface in the spherical coordinate is “ $\sin \theta d\theta d\phi$ ” instead of “ $d\theta d\phi$ ”, the  $P$  and  $W$  are related as:

$$P = W \sin \theta \quad (4.29)$$

After substituting equations 4.27 – 4.29 into the Fokker-Planck equation 4.26, the R.H.S. of equation 4.26 goes to zero if and only if:

$$\mu = 2\Pi_k k_B T \eta, \quad (4.30)$$

where  $T$  is the absolute temperature of the spin thermostat. This gives a relationship between the amplitude  $\mu$  of random fluctuations, the damping constant  $\eta$ , and the desired temperature  $T$  of the spin subsystem. In the numerical implementation of the method, the random noise is modeled with Gaussian random numbers.

## 4.7 Integration Algorithm

Conservation of both the energy and angular momentum is important for a large-scale SLD simulation to yield physically realistic results. However, to control the accumulation of numerical errors to an acceptable level over tens of millions of time steps is not a trivial task. Preliminary investigations showed that standard predictor-corrector methods that have been successfully implemented in MD simulations did not have sufficient accuracy in energy conservation to be of practical use for SLD. Omelyan *et al.* [6]-[8] and Tsai *et al.* [21],[22] investigated the application of symplectic integration algorithms for both the spin and the lattice degrees of freedom. These authors also suggested the possibility of modeling the exchange function using a pairwise inter-atomic function. However, the actual spin-lattice dynamic simulation has not been carried out. On the other hand, Tsai *et al.* did the simulations, but without the coupling between the lattice and the spin

degrees of freedom. Both integration schemes were based on the 2<sup>nd</sup> order Suzuki-Trotter Decomposition (STD) scheme. The integration algorithm presented here follows the same route.

In the current case, the set of SLD equations 4.16 and 4.17 have to be solved simultaneously. Within a small time step  $\Delta t$ , we may assume that there is a Hamiltonian operator  $\mathcal{H}$  that operates on the generalized coordinate  $\mathbf{x}$ , satisfying the equation of motion:

$$\frac{d\mathbf{x}}{dt} = \mathcal{H}\mathbf{x}, \quad (4.31)$$

where  $\mathbf{x}$  is an element of the direct sum of the coordinate space  $\mathbf{R}$ , momentum space  $\mathbf{P}$  and spin-direction space  $\mathbf{S}$ , i.e.  $\mathbf{x} \in \mathbf{R} \oplus \mathbf{P} \oplus \mathbf{S}$ . Referring to equations 4.16 and 4.17,  $\mathcal{H}$  can be decomposed into the sum of three operators, representing the atomic force  $\mathcal{F}$ , atomic velocity  $\mathcal{P}$ , and spin velocity  $\mathcal{S}$ , defined as

$$\begin{aligned} \mathcal{F} : \mathbf{R} \oplus \mathbf{S} &\rightarrow \mathbf{P}, \text{ s.t. } \mathcal{F}\mathbf{x} \equiv -\frac{\partial U}{\partial \mathbf{R}} + \frac{1}{2} \sum_{i,j} \frac{\partial J_{ij}}{\partial \mathbf{R}} (\mathbf{e}_i \cdot \mathbf{e}_j) \\ \mathcal{P} : \mathbf{P} &\rightarrow \mathbf{R}, \text{ s.t. } \mathcal{P}\mathbf{x} \equiv \frac{\mathbf{p}}{m} \\ \mathcal{S} : \mathbf{R} \oplus \mathbf{S} &\rightarrow \mathbf{S}, \text{ s.t. } \mathcal{S}\mathbf{x} \equiv \mathbf{e} \times \sum_i J_i \mathbf{e}_i \end{aligned} \quad (4.32)$$

In this equation, it is to be noted that the operation of  $\mathcal{F}$  is on elements of  $\mathbf{R}$  and  $\mathbf{S}$ , but keeps these spaces unchanged. It only affects the corresponding element in  $\mathbf{P}$ . The operation of  $\mathcal{P}$  is on elements of  $\mathbf{P}$ , and similarly only affects the corresponding element in  $\mathbf{R}$ . The operation of  $\mathcal{S}$  is the only one that also affects elements of  $\mathbf{S}$  on which the operator is defined. The treatment of the  $\mathcal{S}$  operator in a self-consistent way is considered as we proceed. Using these three operators, the equations of

motion (equation 4.16 – 4.17) can be written as

$$\mathcal{H}\mathbf{x} \equiv (\mathcal{P} + \mathcal{F} + \mathcal{S})\mathbf{x} \quad (4.33)$$

and

$$\frac{d}{dt} \begin{pmatrix} \mathbf{R} \\ \mathbf{p} \\ \mathbf{e} \end{pmatrix} = (\mathcal{P} + \mathcal{F} + \mathcal{S})\mathbf{x} = \begin{pmatrix} \frac{\mathbf{p}}{m} \\ -\frac{\partial U}{\partial \mathbf{R}} + \frac{1}{2} \sum_{i,j} \frac{\partial J_{ij}}{\partial \mathbf{R}} (\mathbf{e}_i \cdot \mathbf{e}_j) \\ \mathbf{e} \times \sum_i J_i \mathbf{e}_i \end{pmatrix}, \quad (4.34)$$

If we assume that  $\mathcal{H}$  is constant within a small time interval between time  $t$  and  $t + \Delta t$ , the solution of equation 4.31 can be formally written as

$$\mathbf{x}(t + \Delta t) = e^{\mathcal{H}\Delta t} \mathbf{x}(t). \quad (4.35)$$

According to STD,

$$e^{\mathcal{H}\Delta t} \mathbf{x} = e^{(\mathcal{P} + \mathcal{F} + \mathcal{S})\Delta t} \mathbf{x} = e^{S(\Delta t/2)} e^{(\mathcal{F} + \mathcal{P})\Delta t} e^{S(\Delta t/2)} \mathbf{x} + O(\Delta t^3) \quad (4.36)$$

Physically, when one deals with the operation of  $(\mathcal{F} + \mathcal{P})$ , only variables related to the lattice is affected, but not the spin-directions  $\{\mathbf{e}_k\}$ , i.e., they are frozen constant within the duration of the operation of  $(\mathcal{F} + \mathcal{P})$ , and equation 4.16b becomes

$$\frac{d\mathbf{p}_k}{dt} = -\frac{\partial U}{\partial \mathbf{R}_k} + \frac{1}{2} \sum_{i,j} \frac{\partial J_{ij}}{\partial \mathbf{R}_k} (\mathbf{e}_i \cdot \mathbf{e}_j) = -\frac{\partial U'}{\partial \mathbf{R}_k}, \quad (4.37)$$

Then, equation 4.16 reduces to the conventional MD case without spin. The detailed symplectic integration algorithm for this case has already been presented in Chapter 2.

The exponential operation of  $\mathcal{S}$  does not affect the lattice, which can be considered frozen during the evolution of  $\mathbf{x}$  under the operation of  $\mathcal{S}$ . However, operations involving the spins create complications because the effective field encountered by a particular spin is a self-consistent field determined by other spins. Indeed, the equation 4.17 represents a set of coupled 1<sup>st</sup> order differential equations for all spins, instead of a single equation. Unlike the case of coordinates and momenta the spin-velocity operators  $\mathcal{S}$  produces changes in itself *via* its operation in the spin space  $\mathfrak{S}$ . Therefore, an important aspect of the integration algorithm is associated with keeping track of the non-commuting spin variables. By using the 2<sup>nd</sup> order STD, we can transform this messy problem into a series of single spin rotations, but with the trade off of the  $O(\Delta t^3)$  trajectory error. To treat this situation, the spin-direction space is further decomposed into a direct sum of subspaces, each of which contains the spin direction of a single atom. The spin-velocity operator  $\mathcal{S}$  can then be written as the sum of a series of single spin-velocity operators, i.e.  $\mathcal{S} = (\mathcal{S}_1 + \mathcal{S}_2 + \dots + \mathcal{S}_{N-1} + \mathcal{S}_N)$ , so that

$$e^{S\tau} \mathbf{x} = e^{S_1(\tau/2)} e^{S_2(\tau/2)} \mathbb{L} e^{S_{N-1}(\tau/2)} e^{S_N\tau} e^{S_{N-1}(\tau/2)} \mathbb{L} e^{S_2(\tau/2)} e^{S_1(\tau/2)} \mathbf{x} + O(\tau^3) \quad (4.38)$$

Since the rotation of a single spin is analytically solvable [26] involving no numerical dissipation of the total energy, this leads to the symplecticity of the method. In this regard, recasting equation 4.17 into:

$$\frac{d\mathbf{e}_k}{dt} = \overset{\vee}{\omega}_k \times \mathbf{e}_k \quad (4.39)$$

where  $\overset{\vee}{\omega}_k = -\mathbf{H}_k/\Pi_k$ , the updated spin orientation takes the form:

$$\mathbf{e}_k(t + \tau) = \exp(S_k \tau) \mathbf{e}_k(t) = \mathbf{D}_k(\tau) \mathbf{e}_k(t), \quad (4.40)$$

where

$$\mathbf{D}_k(\tau) = \mathbf{I} + \mathbf{W}_k \sin(|\overset{\vee}{\omega}_k| \tau) + \mathbf{W}_k^2 [1 - \cos(|\overset{\vee}{\omega}_k| \tau)] \quad (4.41)$$

The  $\mathbf{W}_k$  is a skew-symmetric matrix with Cartesian components  $W_{k,xy} = -\omega_{k,z}/|\overset{\vee}{\omega}_k|$ ,  $W_{k,xz} = \omega_{k,y}/|\overset{\vee}{\omega}_k|$  and  $W_{k,yz} = -\omega_{k,x}/|\overset{\vee}{\omega}_k|$ . In practice, since numerical evaluation of “sin” and “cos” function in extremely small angles is not sufficiently accurate due to truncation errors, the rotation of each spin is performed according to [7],

$$\begin{aligned} & \exp(S_k \tau) \mathbf{e}_k(t) \\ &= \frac{\mathbf{e}_k(t) + [\overset{\vee}{\omega}_k \times \mathbf{e}_k(t)] \tau + \left[ \overset{\vee}{\omega}_k (\overset{\vee}{\omega}_k \cdot \mathbf{e}_k(t)) - \frac{|\overset{\vee}{\omega}_k|^2 \mathbf{e}_k(t)}{2} \right] \frac{\tau^2}{2}}{1 + \frac{|\overset{\vee}{\omega}_k|^2 \tau^2}{2}} + O(\tau^3), \quad (4.42) \end{aligned}$$

derived directly from equations 4.39 – 4.41. Higher-order STDs have also been investigated [8], but the 2<sup>nd</sup> order STD algorithm is found to be sufficient for practical simulations.

Since the integration algorithms for both the spin and lattice subsystems are

symplectic, the current integration algorithm is symplectic too, which can resist numerical energy dissipation in the long run. We should note that the symplecticity does not originate from the 2<sup>nd</sup> order STD. However, it is facilitated by supplying a framework within which the operations can be evaluated analytically. Since no approximation is taken in each operation, it eliminates all the calculation error, despite the  $O(\Delta t^3)$  trajectory error and machine error. This is the real reason of the symplecticity. In practice, Omelyan *et al.* decomposed the system as:

$$\mathbf{x}(t + \Delta t) = e^{J\Delta t} \mathbf{x}(t) = e^{\mathcal{F}(\Delta t/2)} e^{\mathcal{P}(\Delta t/2)} e^{\mathcal{F}\Delta t} e^{\mathcal{P}(\Delta t/2)} e^{\mathcal{F}(\Delta t/2)} \mathbf{x}(t) + O(\Delta t^3) \quad (4.42)$$

whereas Tsai *et al.* decomposed it as:

$$\mathbf{x}(t + \Delta t) = e^{J\Delta t} \mathbf{x}(t) = e^{S(\Delta t/2)} e^{\mathcal{F}(\Delta t/2)} e^{\mathcal{P}\Delta t} e^{\mathcal{F}(\Delta t/2)} e^{S(\Delta t/2)} \mathbf{x}(t) + O(\Delta t^3) \quad (4.43)$$

For convenience, we denote Omelyan's method by  $(\mathcal{F}, \mathcal{P}, S, \mathcal{P}, \mathcal{F})$  and Tsai's approach by  $(S, \mathcal{F}, \mathcal{P}, \mathcal{F}, S)$ , neither of which have been used for the current SLD numerical scheme. Instead, the  $(S, \mathcal{P}, \mathcal{F}, \mathcal{P}, S)$  decomposition is used to minimize operations involving  $\mathcal{F}$ , which is the most time consuming step of the algorithm due to the force evaluation.

When stochasticity is incorporated in the Langevin spin dynamics equation 4.24, the numerical integration is adjusted. The formulism is the same as equation 4.39, but with  $\overset{V}{\omega}_k = -\Pi_k^{-1} [(\mathbf{H}_k + \mathbf{h}_k) - \eta(\mathbf{e}_k \times \mathbf{H}_k)]$ , which is complicated by the presence of  $\mathbf{e}_k(t)$  itself. We solve this problem by proceeding as in the 2<sup>nd</sup> order Runge-Kutta method [27]. To advance from time-step  $n$  to  $n+1$ , one can write:

$$y_{n+1} = y_n + k_2 + O(\Delta t^3) \quad (4.44)$$

where  $k_2 = f\left(x_n + \frac{1}{2}\Delta t, y_n + \frac{1}{2}k_1\right)\Delta t$  and  $k_1 = f(x_n, y_n)\Delta t$ . A trial step is made to the midpoint of the interval, and then the value at midpoint is used to calculate the real step across the whole interval. The error is  $O(\Delta t^3)$ . Using the similarity with the linear case, one may first advance the atomic spin from  $t$  to  $t + \Delta t/2$ , i.e.,

$$\mathbf{e}_k\left(t + \frac{\Delta t}{2}\right) = \exp\left(L_{s_k} \frac{\Delta t}{2}\right) \mathbf{e}_k(t) \quad (4.45)$$

with  $\overset{V}{\omega}_k = -\Pi_k^{-1} \left\{ (\mathbf{H}_k + \mathbf{h}_k) - \eta [\mathbf{e}_k(t) \times \mathbf{H}_k] \right\}$ . Then, we can substitute this midpoint value into  $\overset{V}{\omega}_k$  and follow the evolution again from  $t$  to  $t + \Delta t$ :

$$\mathbf{e}_k(t + \Delta t) = \exp\left(L_{s_k} \Delta t\right) \mathbf{e}_k(t) \quad (4.46)$$

where  $\overset{V}{\omega}_k = -\Pi_k^{-1} \left\{ (\mathbf{H}_k + \mathbf{h}_k) - \eta [\mathbf{e}_k(t + \Delta t/2) \times \mathbf{H}_k] \right\}$ . Since the error of STD is of the order of  $O(\Delta t^3)$ , the method is fully justified.

From the discussion above one might get the superficial impression that since the  $(\mathcal{F}, \mathcal{P}, \mathcal{F})$  decomposition is equivalent to the velocity Verlet algorithm, one can simply add two “ $S$ ” parts to an existing MD program. Unfortunately, this naïve recipe is invalid, because in a  $(S, \mathcal{F}, \mathcal{P}, \mathcal{F}, S)$  decomposition, the “ $F$ ” part depends *both* on the atomic *and* the spin configurations. Therefore, after the application of

the first “ $S$ ” operator, the forces acting on atoms have to be recalculated. In the velocity Verlet algorithm, forces are evaluated at the current and the preceding time steps to find the new velocity. Also, the force corresponding to the preceding time step is normally taken from the calculation in the previous time step. In the STD, evolution of each degree of freedom is coupled to all the other variables. This makes the parallelization of the algorithm a challenging task, the solution of which will form the subject of the next chapter.

## 4.8 Brief Conclusion

The methodology of Spin-Lattice Dynamics (SLD) simulation is established in this chapter where the coupled dynamics of the spin and lattice subsystems are treated on equal footing. The equations of motion are derived for a system of particles with interacting intrinsic spins. The particles interact *via* a many-body potential and the spins *via* a Heisenberg-type Hamiltonian with an exchange function depending on the interatomic separation, which couples the lattice and spin subsystems. To facilitate energy and angular momentum interchange of the ferromagnetic system with the environment, the concept of a reservoir is used. The spin temperature is introduced by the fluctuation-dissipation theorem (FDT). Following the framework established by Brown [5], the relationship between the dissipative coefficient and random forces is derived. The 2<sup>nd</sup> order Suzuki-Trotter decomposition approach is adopted to design the integration algorithm for SLD, to minimize numerical energy dissipation. Treatment for the spin subsystem has to be specifically designed to tackle the problem of entanglement. The modification on

the numerical scheme for the stochastic equation is also presented.

**REFERENCE**

- [1] D. G. Pettifor, *Bonding and Structure of Molecules and Solids* (Oxford University Press, Oxford, 1995).
- [2] P. Mohn, *Magnetism in the Solid State* (Springer, Heidelberg, 2003).
- [3] J. Kubler, *Theory of itinerant electron magnetism* (Oxford University Press, 2000) page 158 – 162
- [4] S. L. Dudarev and P. M. Derlet, *J. Computer-Aided Mater. Des.* **14**, 129 (2007)
- [5] W. F. Brown Jr., *Phys. Rev.* **130**, 1677 (1963)
- [6] I. P. Omelyan, I. M. Mryglod and R. Folk, *Phys. Rev. Lett.* **86**, 898 (2001)
- [7] I. P. Omelyan, I. M. Mryglod and R. Folk, *Phys. Rev. E*, **64**, 016105 (2001)
- [8] I. P. Omelyan, I. M. Mryglod and R. Folk, *Phys. Rev. E*, **66**, 026701 (2002)
- [9] L. A. Turski, *Phys. Rev. B*, **30**, 2779 (1984)
- [10] J. H. Van Vleck, *Rev. Mod. Phys.*, **17**, 27 (1945)
- [11] Duk Joo Kim, *New Perspectives in Magnetism of Metals* (Kluwer Academic/Plenum Publishers, New York, 1999), page 63-67.
- [12] S. L. Dudarev and P. M. Derlet, *J. Phys.: Condens. Matter* **17**, 7097 (2005)
- [13] C. Kittel and E. Abrahams, *Rev. Mod. Phys.*, **25**, 233 (1953)
- [14] T. Holstein and H. Primakoff, *Phys. Rev.*, **58**, 1098 (1940)
- [15] A. J. Dekker, *Solid State Physics* (Englewood Cliffs, N.J., Prentice-Hall, 1957)
- [16] S. Morán, C. Edere and M. Fähnle, *Phys. Rev. B*, **67**, 012407 (2003)
- [17] R. F. Sabiryanov and S. S. Jaswal, *Phys. Rev. Lett.* **83**, 2062 (1999)
- [18] T. L. Gilbert, *IEEE Trans. Magn.*, **40**, 3443 (2004)
- [19] M. Fähnle, R. Drautz, R. Singer, D. Steiauf and D. V. Berkov, *Comp. Mater.*

*Sci.* **32**, 118 (2005)

[20] P. M. Derlet and S. L. Dudarev, *Prog. Mater. Sci.* **52**, 299 (2007)

[21] S. H. Tasi, M. Krech and D. P. Landau, *Brazil. J. Phys.*, **34**, 382 (2004)

[22] S. H. Tsai, H. K. Lee and D. P. Landau, *Am. J. Phys.*, **73**, 615 (2005)

[23] J. L. García-Palacios and F. J. Lázaro, *Phys. Rev. B*, **58** 14937 (1998)

[24] S. Chandrasekhar, *Rev. Mod. Phys.*, **15**, 1 (1943)

[25] R. Kubo, *Rep. Prog. Phys.*, **29**, 255 (1966)

[26] J. B. Marion and S. T. Thornton, *Classical Dynamics of Particles and systems*,  
4<sup>th</sup> Ed. (Harcourt, Inc. 1995)

[27] W. H. Press, B. P. Flannery, S. A. Teukolsky, W. T. Vetterling, *Numerical recipes in C++ : the art of scientific computing, 2nd ed.* (Cambridge University Press, 2002)

# Chapter 5: Parallel Algorithms for Suzuki-Trotter Decomposition

## 5.1 Brief Introduction

In the previous chapter, the physical background and the numerical scheme for the Spin-Lattice Dynamics (SLD) are presented. The associated computer program is structured following a conventional molecular dynamics (MD) simulation, with the intrinsic (classical) spin degrees of freedom and its coupling to the lattice subsystems taken into account *via* the exchange function. Similar to MD, large-scale simulations that involve millions of atoms and tens of millions of time-steps can be most efficiently carried out using parallel programming techniques to reduce often extremely long computation time (or run-time) [1]-[6]. In addition, a stable integration algorithm that allows a larger time-step can also enhance the overall performance. In comparison to predictor-corrector method, a symplectic Suzuki-Trotter decomposition (STD) method [6]-[13] is shown to be superior, because of the resistance to the numerical energy dissipation. Reasons are already mentioned in Chapter 2 and 4.

Normally, parallel programming can be readily performed with STD only in procedures in which the spin system is not involved. In STD the decomposition of the spin subsystem has to be performed sequentially, as explained in the previous chapter. To design a parallel algorithm for the STD scheme in such cases is not straightforward. In this chapter, a proposed methodology to tackle the problem is

presented. The designed algorithm has been verified in computer systems with share memory architecture (e.g. using OpenMP), and is capable of achieving a gain in speed of 6-7 times with 8 threads.

## 5.2 Current Parallel Algorithms

Parallel algorithms of MD are usually designed based on three types of decomposition schemes: atomic, force and spatial [1],[5]. The purpose of the algorithm is to distribute the workload over a set of processors/threads to speed up the computation by allowing independent procedures to be carried out simultaneously. Trobec *et al.* [6] reviewed several symplectic integration methods with parallel algorithms in MD simulation. Although the Leap-Frog-Verlet (LFV) and Split Integration Symplectic Method (SISM) are different on how the Hamiltonian is split, both of them belong to the 2<sup>nd</sup> order STD. The LFV algorithm, or called velocity Verlet algorithm, is indeed equivalent to equations 2.11 and 2.12, with solution,

$$\mathbf{x}(t + \Delta t) = e^{\mathcal{H}\Delta t} \mathbf{x}(t) = e^{\mathcal{F}\Delta t/2} e^{\mathcal{P}\Delta t} e^{\mathcal{F}\Delta t/2} \mathbf{x}(t) + O(\Delta t^3) \quad (5.1)$$

for the operator  $\mathcal{H} = (\mathcal{F} + \mathcal{P})$  and  $\mathbf{x}$  is the generalized co-ordinates, as defined in previous chapter. Within a single time step, three evolutionary steps have to be processed sequentially. Thus, parallel algorithm of any of the 3 types of decompositions can only be implemented within each evolutionary step [6].

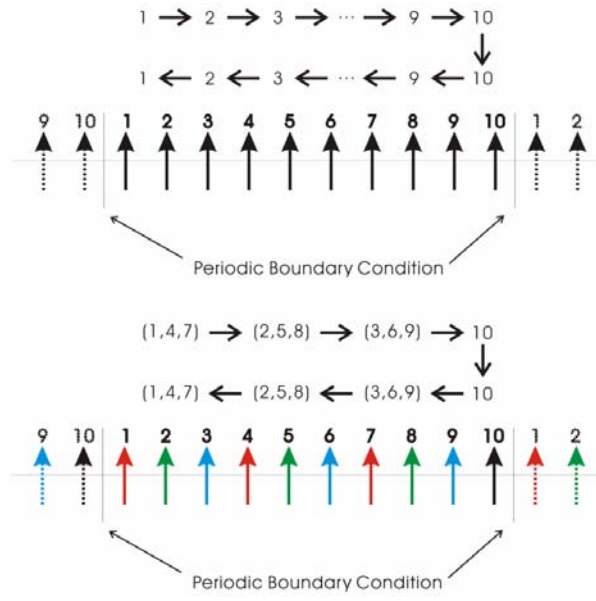


Figure 5.1 – Schematic picture of 1D spin chain containing 10 spins, where the Suzuki-Trotter decomposition is (top) sequential; (bottom) parallelized

This type of algorithms is effective only when each evolution operation can simultaneously involve a sufficiently large number of variables. However, in SLD simulations, the evolution of the spin of each atom has to be treated sequentially. This situation may be most easily visualized in the pure spin dynamics example of a 1D spin chain system with 10 spins, as depicted schematically in the top half of Figure 5.1. The evolution of the spin chain from time  $t$  to  $t + \Delta t$  in the STD scheme can be written as:

$$\mathbf{e}(t + \Delta t) = e^{s_1 \Delta t / 2} e^{s_2 \Delta t / 2} \dots e^{s_{10} \Delta t} \dots e^{s_2 \Delta t / 2} e^{s_1 \Delta t / 2} \mathbf{e}(t) + O(\Delta t^3) \quad (5.2)$$

where  $e^{s_k \Delta t}$  is the evolution operator of  $\mathbf{e}_k(t)$  over the time interval  $(t, t + \Delta t)$  and  $\mathbf{e}(t) = \{\mathbf{e}_k(t)\}$  is the system of unit atomic spin vectors. In equation 5.2, the evolution of the spin system is processed from spin No. 1 to No. 10, then reversely from spin No. 10 to No. 1. For simplicity, it may be represented as (1, 2, 3, 4, 5, 6,

7, 8, 9, 10, 9, 8, 7, 6, 5, 4, 3, 2, 1). In other words, the evolution of spin No. 1 depends on spin No. 2, the evolution of which depends on spin No. 3, ... up to spin No. 10. It is impossible to do any parallel programming under such circumstances.

### 5.3 Grouping Independent Atoms

In most computer simulations, a cutoff distance for the interatomic potential is needed due to the presence of screening effects or simply to cut down unnecessary computation. The dynamics of an atom and its spin thus only depend on others in a defined neighborhood, and are independent of those outside this neighborhood. In other words, the evolution of an atom and its spin only depends on information from a *selected number* of atoms to which it is linked, rather than from the *entire* system.

For the 1D spin chain shown in Figure 5.1, for example, the evolution of spin No. 1 is independent of spins No. 4 and No. 7 (the bottom of Figure 5.1) if the exchange coupling is assumed to extend to the 2<sup>nd</sup> nearest neighbors only. In addition, according to STD,

$$\begin{aligned}
 & e^{(A+B+C)\tau} \mathbf{x}(t) \\
 &= e^{A\tau/2} e^{B\tau/2} e^{C\tau} e^{B\tau/2} e^{A\tau/2} \mathbf{x}(t) + O(\tau^3) \\
 &= e^{B\tau/2} e^{A\tau/2} e^{C\tau} e^{A\tau/2} e^{B\tau/2} \mathbf{x}(t) + O(\tau^3) \\
 &= e^{C\tau/2} e^{B\tau/2} e^{A\tau} e^{B\tau/2} e^{C\tau/2} \mathbf{x}(t) + O(\tau^3)
 \end{aligned} \tag{5.3}$$

Thus, the order of the operation is immaterial if they are interchanged according to equation 5.3. This property allows us to rearrange (1, 2, ..., 10, ..., 2, 1) into (1, 4,

7, 2, 5, 8, 3, 6, 9, 10, 9, 6, 3, 8, 5, 2, 7, 4, 1) or ( $\{1,4,7\}$ ,  $\{2,5,8\}$ ,  $\{3,6,9\}$ , 10,  $\{3,6,9\}$ ,  $\{2,5,8\}$ ,  $\{1,4,7\}$ ). Because atoms No. 1, 4 and 7 in  $\{1,4,7\}$  are independent, they evolve independently and can be processed simultaneously in different threads, followed by the group  $\{2,5,8\}$  and then  $\{3,6,9\}$ , and so on. For the remaining atom No. 10, it is a group on its own. We may use this approach to formulate a parallel algorithm in which atoms are collected into groups within which members are all independent and can therefore be processed simultaneously in different threads. Of course, it is important that before starting any calculation on a specific group, one must ensure the calculation on the previous group is completed. In other words, a “barrier” directive is needed.

5	1	2	3	4	5	1
25	21 <sup>E</sup>	22 <sup>F</sup>	23 <sup>G</sup>	24 <sup>H</sup>	25 <sup>G</sup>	21
20	16 <sup>D</sup>	17 <sup>C</sup>	18 <sup>D</sup>	19 <sup>E</sup>	20 <sup>F</sup>	16
15	11 <sup>A</sup>	12 <sup>B</sup>	13 <sup>A</sup>	14 <sup>B</sup>	15 <sup>C</sup>	11
10	6 <sup>D</sup>	7 <sup>C</sup>	8 <sup>D</sup>	9 <sup>E</sup>	10 <sup>F</sup>	6
5	1 <sup>A</sup>	2 <sup>B</sup>	3 <sup>A</sup>	4 <sup>B</sup>	5 <sup>C</sup>	1
25	21	22	23	24	25	21

Figure 5.2 – A 2D system that is cut into 25 link-cells with periodic boundary condition. All the cells are allocated into group A to group H.

In 2D and 3D cases, although one may still use the atomic delinking approach, the spatial delinking approach may be more convenient. As in conventional MD, the simulation box is usually divided into many smaller boxes, called link-cells [14]. Since the edge of each cell is larger than the cutoff distance(s) of interatomic

potential and/or exchange coupling, the forces on a particular atom or spin can only come from atoms within its own cell or surrounding cells. The implementation of link cells greatly enhances the computation efficiency by reducing redundant calculations. Figure 5.2 is an illustration of a 2D system divided into 25 link cells with periodic boundary condition. Treating each cell as a subsystem, they may be group into groups A to H (Figure 5.2), so that any atom in a member cell of a group is independent of any atom in any other cell of the same group. As a result, cells in the same group can be processed simultaneously in different threads. For example, cells {1,3,11,13} constitute group A, {2,4,12,14} group B, etc. Then, cell No. 1, 3, 11 and 13 can be processed concurrently. The working sequence (1,2,...,25...,2,1) can be recast into a different one (A, B,...,H,...,B, A), i.e.

$$e^{L_1 \frac{\Delta t}{2}} e^{L_2 \frac{\Delta t}{2}} \dots e^{L_{25} \Delta t} \dots e^{L_2 \frac{\Delta t}{2}} e^{L_1 \frac{\Delta t}{2}} \mathbf{x}(t) \rightarrow e^{L_A \frac{\Delta t}{2}} e^{L_B \frac{\Delta t}{2}} \dots e^{L_H \Delta t} \dots e^{L_B \frac{\Delta t}{2}} e^{L_A \frac{\Delta t}{2}} \mathbf{x}(t) \quad (5.4)$$

It is to be noted that atoms/spins within a link-cell has to be processed sequentially according to STD. The 3D case is similar to 2D, but the number of cells in a group is increased to 26. In practice, a subprogram can be written to allocate members into groups automatically.

Essentially, the parallel algorithm works to rearrange the order of the evolutionary operations, without violating the validity of STD. Then, one can gather them into groups in which the cells are independent, so that in each group evolutionary step, all the cells in the group can be processed simultaneously in parallel. Of course, the evolutionary operation of different groups still has to be treated sequentially.

## 5.4 Integrity of the Algorithm

The integrity of the algorithm is checked by Bernstein's conditions [15] and Leslie Lamport's sequential consistency model [16]. Bernstein's condition states that when there are two program fragments  $P_i$  and  $P_j$ , with input  $I_{i(j)}$  and output  $O_{i(j)}$  variables, they can be calculated simultaneous if  $I_{i(j)} \cap O_{j(i)} = \emptyset$  and  $O_i \cap O_j = \emptyset$ . It means that the same memory cannot be shared between different threads, except for inputs only. Otherwise, it causes race condition. Since each operator only needs information on itself and its surroundings, they do not need data from other members of the same group nor alter any of their properties. Therefore, it satisfies the Bernstein's condition. Moreover, working on the same group members in sequential or parallel should be the same, as all processors are just calculating according to the same set of equations of motion, and each calculation is independent of the output of its group member, unless one of those processors produces different result. It satisfies the Leslie Lamport's sequential consistency model.

Indeed, the foregoing spatial decomposition scheme can also be applied to MD simulations. It has the advantage of saving the necessity of protective locks [16] on memory in the evaluation of forces. Since forces are calculated in pairs (Newton's 3<sup>rd</sup> Law), the outputs do not only modify the data within a particular link-cell, they also modify those in surrounding. Within the present method, a lock within its own link-cell is unnecessary. When a lock is applied (E.g. OpenMP, the directive in C/C++ is “#pragma omp atomic”), it may slow down the program. Surely, there is tradeoff between this and the load balance. From the above example

of 2D case, one may notice that idle processors are unavoidable.

## 5.5 Efficiency

In the following, the efficiency of the proposed algorithm will be evaluated by realistic simulations. For this purpose, simulations are performed according to the SLD equations of motion (i.e., equation 4.16 and 4.17) in a micro-canonical (NVE) ensemble. The same spatial decomposition schemes as mentioned in section 4.3 are applied to the spin and lattice subsystems. In each case, atoms are initially placed in a regular bcc lattice in [100] directions with lattice constant  $a = 2.8665\text{\AA}$ . Five different lattice configurations are used. They are all cubes with edge sizes  $20a$ ,  $30a$ ,  $40a$ ,  $50a$  and  $80a$ , with numbers of atoms 16000, 54000, 128000, 250000 and 1024000 respectively. The velocities of all the atoms are initially set to zero. All the spins in the left-hand side of the simulation cell are initialized to point upwards whereas those on the right hand side point downwards, making a  $180^\circ$  domain wall structures. Periodic boundary conditions are applied along  $x$ ,  $y$  and  $z$ . The edge of each link-cell is larger than the cutoff distance of the interatomic potential and exchange function for spin-spin interaction.

The actual run-time of the above model (i.e.  $\mathcal{H} = (\mathcal{F} + \mathcal{P} + \mathcal{S})$ ) and the one with only spin part (i.e.  $\mathcal{H} = \mathcal{S}$  only; a fixed lattice system) is recorded for 10000 time-steps. A computer with 2 *Intel Xeon Quad-core x5355* CPU and 4GB RAM is used. Totally there are 8 cores. Due to the hardware limitation, only the efficiency from 1 to 8 threads is tested. In the software aspect, *Scientific Linux 5.0* and *Intel*

C++ compiler 10.0 with OpenMP package is used. The efficiency is defined as [17]:

$$Eff(n) = \frac{T(1)}{nT(n)} \quad (5.5)$$

where  $Eff(n)$  is the efficiency and  $T(n)$  is the run-time for  $n$  threads. The term efficiency does not relate directly to the actual run-time. For example, if a program needs 10 minutes to finish the calculation by using a single thread, and it takes 6 minutes by 2 threads, actually it runs faster, but its efficiency is only 83%.

Figure 5.3 and Figure 5.4 show the run-time and efficiency of spin only system, while Figure 5.5 and Figure 5.6 show the run-time and efficiency of systems with coupled spin and lattice dynamics. In both cases, they show similar behavior. The run-time always decreases with more threads, independent of the size of the systems (ranging from ten thousands to million spins and atoms). However, they tend to reach saturation for about 8 threads. It should be due to Amdahl's law [18], which states that because of the sequential part, a parallelized program cannot be speedup more than  $n$  times and the usefulness of those parallel parts. Fortunately, the run-times appear to increase linearly with the systems' size. Because of the order- $N$  nature of the link-cell system, the total calculation time on forces increases only linearly when the number of atoms. When 8 threads are used, the run-time for 1024000 (which is more than one million) atoms is about 2.3s and 8.4s per time-step for spin only and spin-lattice systems, respectively. If one uses a time-step of 1 femtosecond, it takes about 2.7 days and 9.7 days to reach 0.1 nanosecond. It should be acceptable to have such speed on a single machine.

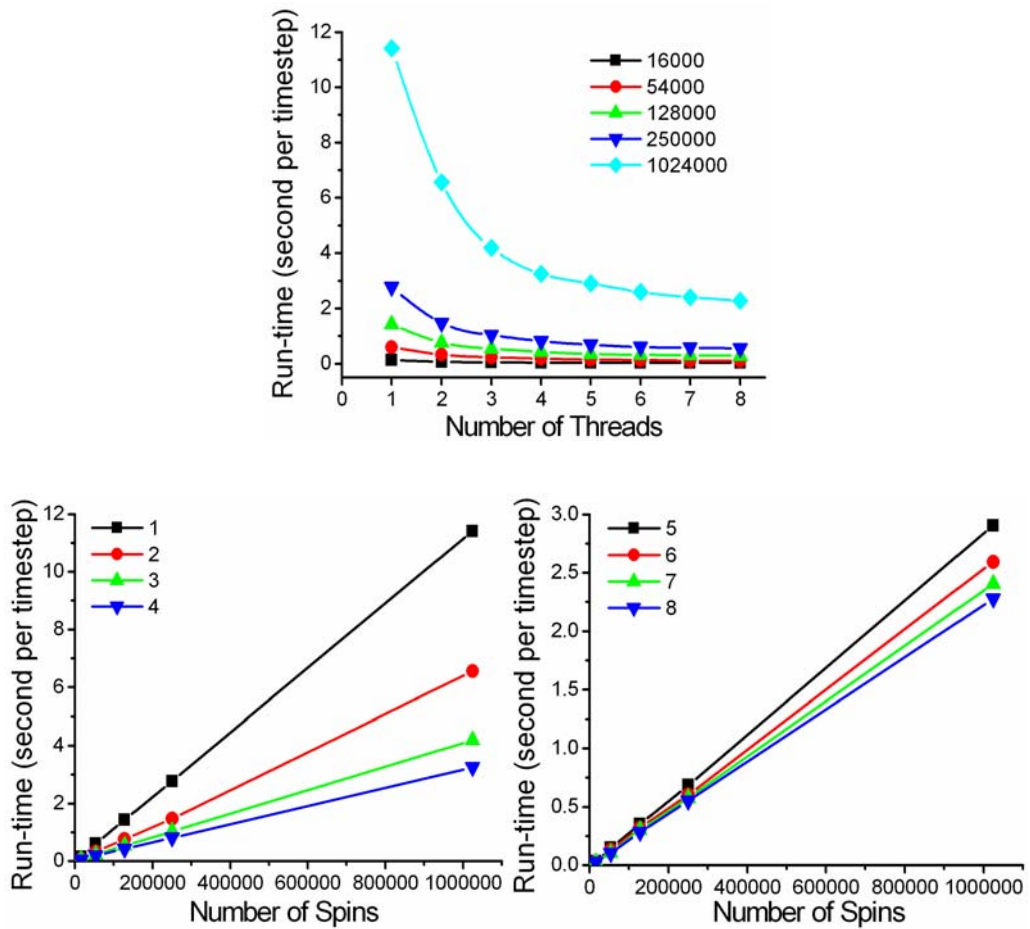


Figure 5.3 – The actual run-time of spin only system (top) versus number of threads with 16000, 54000, 128000, 250000 and 1024000 spins; (bottom left) versus number of spins with threads from 1 to 4; (bottom right) versus number of spins with threads from 5 to 8.

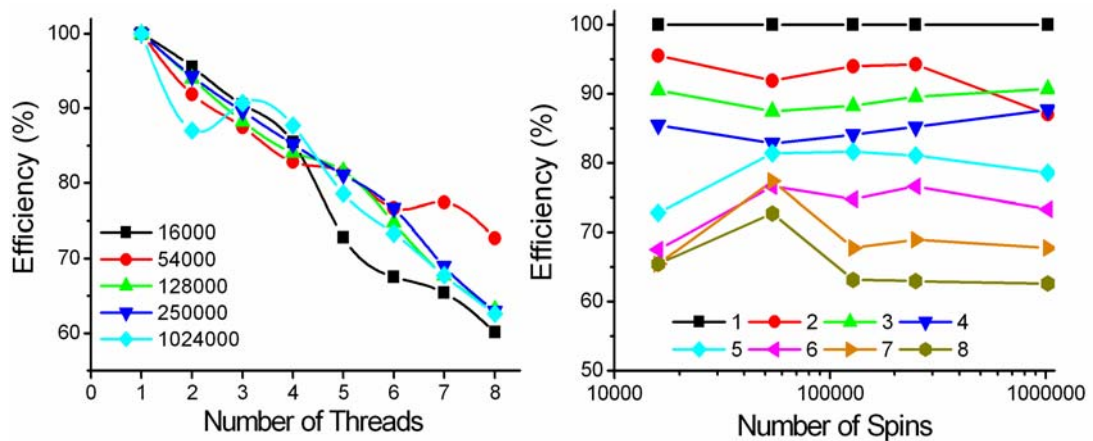


Figure 5.4 – The efficiency of spin only system (left) versus number of threads with 16000, 54000, 128000, 250000 and 1024000 spins; (right) versus number of spins with threads from 1 to 8.

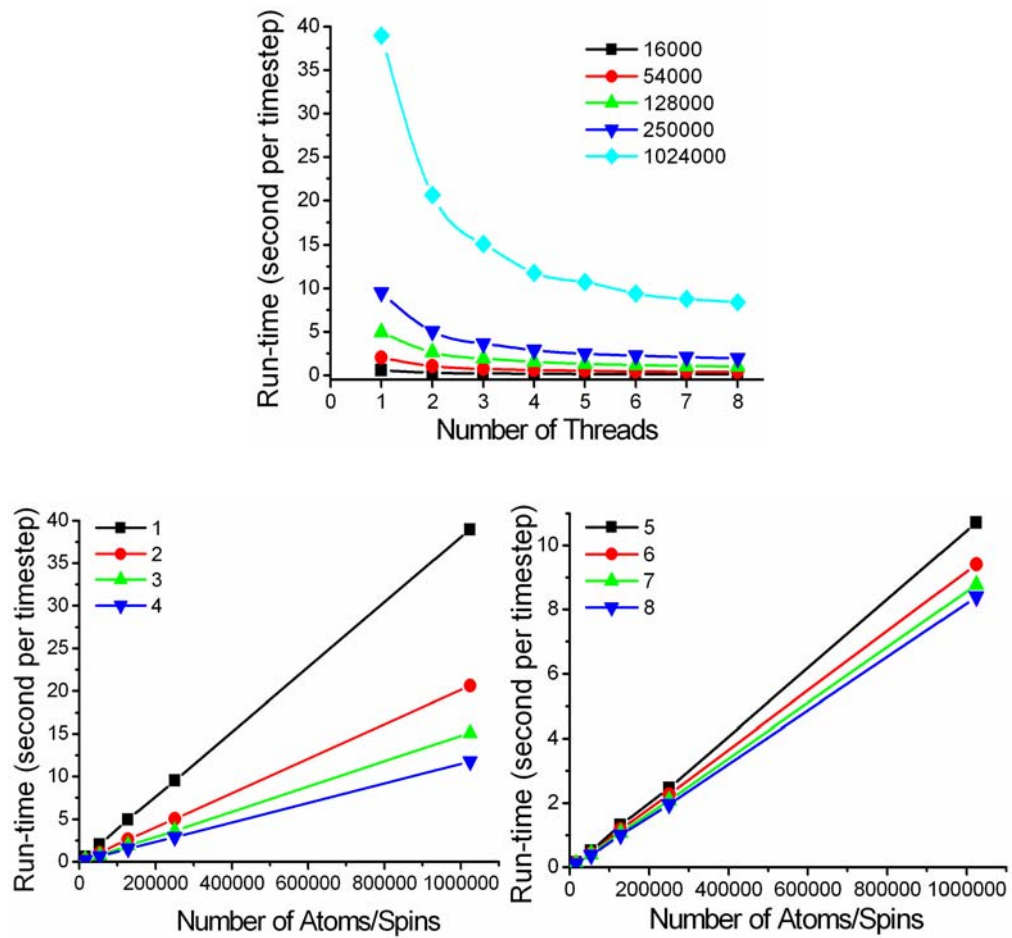


Figure 5.5 – The actual run-time of spin-lattice system (top) versus number of threads with 16000, 54000, 128000, 250000 and 1024000 spins; (bottom left) versus number of spins with threads from 1 to 4; (bottom right) versus number of spins with threads from 5 to 8.

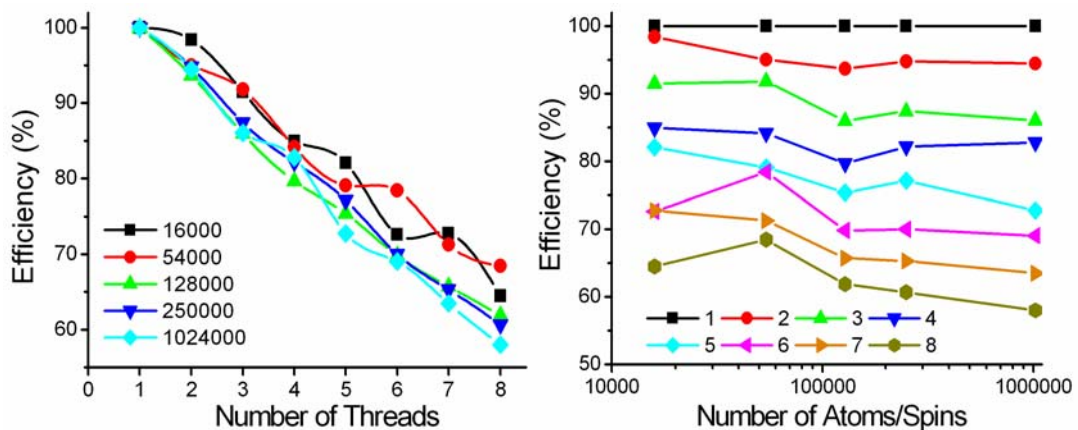


Figure 5.6 – The efficiency of spin and lattice coupled system (left) versus number of threads with 16000, 54000, 128000, 250000 and 1024000 spins; (bottom) versus number of spins with threads from 1 to 8

The curves of efficiency generally show monotonic decreasing, but with fluctuations. This behavior may be due to the resources wastage on the idle processors time. For example, in the spin-only system, the one with 1024000 spins is separated into 18 groups. There are 8 groups with 19683 members, 2 groups with 2783 members, 2 groups with 1431 members, 2 groups with 207 members, 1 group with 31 members, 1 group with 30 members and 2 groups with 4 members. Suppose each link-cell (i.e. member) needs about the same calculation time, one can count when using 3 threads, it got 7 units idle processors time. But for 2 threads, it got 15 units idle processors time. Therefore it is not surprising to see the sudden increase in the efficiency of 3 threads. Of course, it is not the only reason. It also depends on various others factors, such as the architecture of compiler, OS, processor, memory etc. Moreover, since each link-cell is not required to contain the same number of atoms, load-balance is another important issue in this kind of spatial decomposition algorithm.

As a whole, one can see that the overall trend of the efficiency is decreasing linearly from 100% to about 60~70%, when 1 to 8 threads are used. Comparing to some other parallel algorithms, such as certain force decomposition method [3], which can attain 98.88% efficiency, the current method are certainly inferior. However, one must remember that we are dealing with an extreme case of STD, in which most parallel processing schemes do not work.

## 5.6 Stability

Stability is another important aspect to consider. Figure 5.7 shows that the total energy per atom of the  $180^\circ$  domain wall system with 54000 atoms and spins as a function of computation time using respectively the  $(S, F, P, F, S)$  and the  $(S, P, F, P, S)$  algorithms, with the proposed parallel algorithm already incorporated. Both the  $(S, F, P, F, S)$  and the  $(S, P, F, P, S)$  algorithms perform well, and the total energy per atom remains constant within  $\sim 10^{-5}$  eV and sometimes  $\sim 10^{-6}$  eV. This demonstrates the stability of our program for the long runs ( $>1$ ns). Furthermore, the speed of the  $(S, P, F, P, S)$  SLD algorithm is recorded. It is found to be approximately half the speed of the velocity Verlet algorithm, when compared with conventional MD. Moreover, the  $(S, F, P, F, S)$  algorithm is approximately 60% slower than the  $(S, P, F, P, S)$  algorithm.

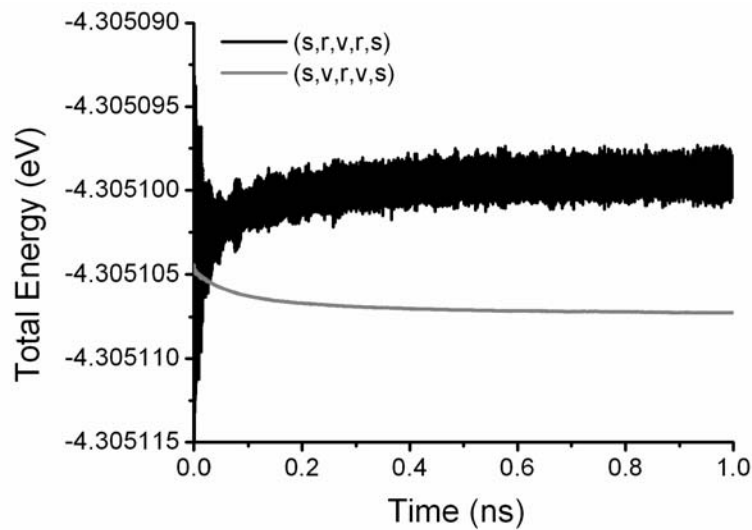


Figure 5.7 – The total energy per atom versus time for a microcanonical ensemble simulation of the dynamical relaxation of a  $180^\circ$  domain wall. Two algorithms, the

$(S, F, P, F, S)$  and the  $(S, P, F, P, S)$ , in both of which the parallel algorithm for STD is incorporated, are compared. The  $(S, P, F, P, S)$  algorithm is found to be ~60% faster than the  $(S, F, P, F, S)$  algorithm

## 5.7 Brief Conclusion

A parallel algorithm is developed for application to the STD method for spin dynamics (SD) and spin-lattice dynamics (SLD) simulations, where each evolutionary step for the spin subsystem has to be processed sequentially, one spin at a time. Indeed, the parallel algorithm for STD is simply to rearrange the order of the evolution operations in groups, and making sure they are independent of each other within a group. The efficiency is about 60~70% when using 8 threads. The run-time per time step is linearly proportional to the system size. Such algorithms can also be implemented on conventional MD and SD programs, without handling complicated mathematics. It can be applied to very large system (>million atoms and/or spins). It also shows satisfactory stability and conservation of energy in long runs of  $>1 \times 10^6$  time-steps, corresponding to 1 ns. No iteration or further approximation is needed within our algorithm. Only the trajectory error with  $O(\Delta t^3)$  from the STD remains. The proposed method is not mutually exclusive to other decomposition methods. For example, one can use spatial decomposition twice, which gives two layers of decomposition. The first layer can be distributed within the cluster by MPI (Message Passing Interface) and the second layer is distributed within the machine by OpenMP.

## REFERENCES

- [1] S. J. Plimpton and B. A. Hendrickson, “Parallel Molecular Dynamics with the Embedded Atom Method”, in *Materials Theory and Modeling*, Vol. 291 *Materials Research Society Symposium Proc., Fall 1992*, p.37
- [2] S. J. Plimpton, *J. Comp. Phys.* **117**, 1 (1995).
- [3] R. Murty and D. Okunbor, *Parallel Computing*, **25**, 217 (1997)
- [4] A. Fijany, T. Cağınm, A. Jaramillo-Botero and W. Goddard III, “Novel Algorithms for Massively Parallel, Long-term, Simulation of Molecular Dynamics Systems”, *Advances in Engineering Software*, Vol. 29, No. 3-6 (1998) 441-450
- [5] G. S. Heffelfinger, Parallel Atomistic Simulations, *Comp. Phys. Comm.* **128** 219 (2000)
- [6] R. Trobec, F. Merzel and D. Janežič, *J. Chem. Inf. Comp. Sci.*, **37** 1055 (1997)
- [7] D. Janežič and F. Merzel, *J. Chem. Inf. Comput. Sci.*, **37** 1048 (1997)
- [8] I. P. Omelyan, I. M. Mryglod and R. Folk, *Phys. Rev. Lett.* **86**, 898 (2001)
- [9] I. P. Omelyan, I. M. Mryglod and R. Folk, *Phys. Rev. E* **64**, 016105 (2001)
- [10] I. P. Omelyan, I. M. Mryglod and R. Folk, *Phys. Rev. E* **66**, 026701 (2002)
- [11] S. H. Tasi, M. Krech and D. P. Landau, *Brazil. J. Phys.* **34**, 382 (2004)
- [12] S. H. Tsai, H. K. Lee and D. P. Landau, *Am. J. Phys.* **73**, 615 (2005)
- [13] M. Krech, Alex Bunker and D. P. Landau, *Comp. Phys. Comm.* **111**, 1 (1998)
- [14] M. P. Allen and D. J. Tildesley, “*Computer Simulation of Liquids*” (Oxford University Press, 1987)
- [15] A. J. Bernstein, *IEEE Trans. Electronic Comp.*, **Vol. EC-15**, No. 5, 757 (1966)
- [16] Leslie Lamport, *IEEE Trans. on Comp.*, **Vol. C-28**, No. 9, 690 (1979)

- [17] L. R. Scott, T. Clark and B. Bagheri, *Scientific Parallel Computing*, (Princeton, NJ: Princeton University Press, 2005)
- [18] G. Amdahl, *AFIPS Conference Proceedings*, **30** 483 (1967)

# Chapter 6: Equilibration Processes in a Microcanonical Ensemble

## 6.1 Brief Introduction

According to Van Kranendonk and Van Vleck [1], spin-spin relaxation of perturbations that “spoil the constancy of the spatial components of magnetic moment” take place *via* the exchange interactions. Spin-lattice relaxation, on the other hand, occurs through the “modulation of the spin interaction energies, i.e. the spin waves, by the crystalline vibration” [1] or, in other words, through the variation of the exchange function due to thermal vibrations of atoms in the lattice [2]. Since spin-spin relaxation is an equilibration process whereby non-equilibrium states introduced by an external perturbation are eliminated, locally triggered magnetic reversal could be smeared out during the relaxation. In addition, if the spin and lattice subsystems are not in equilibrium with each other, spin-lattice relaxation may modify the magnetization by creating or annihilating magnons *via* phonon-magnon interaction. Therefore, it is of technological importance to understand the timescales and the detail mechanisms of these two processes. In particular, spin-spin and spin-lattice relaxation times are crucial to data integrity in high-speed magnetic storage devices, and a wide range of magneto-optical experiments [3]-[11] have been performed to generate the needed information for design purposes, in addition to the obvious scientific interest.

In pure spin dynamics, spin-spin relaxation is usually described by the

damping term in the Landau-Lifshitz or Gilbert equation [12] (equation 1.1 and 1.2), which restores the direction of magnetization when misorientation occurs. In that case, the spin-spin relaxation time  $\tau_{ss}$  can be interpreted as a quantity inversely proportional to the damping constants. Experimentally, one may obtain a measurement of  $\tau_{ss}$  from the linewidth of the ferromagnetic resonance (FMR) signal. Such measurements for iron [13]-[15] found  $\tau_{ss}$  to be in the range of 1 to 10ns. Conversely, in the pulsed laser pump-probe experiment by Scholl *et al.* [6] and the magneto-optical Kerr effect (MOKE) experiment by Koopmans *et al.* [7], the spins in Ni thin films was found to equilibrate within a timescale of a few tens of picoseconds. Since the exchange coupling of Fe is much stronger than Ni, one would expect that  $\tau_{ss}$  of Fe is shorter, or at least of the same order as Ni. Obviously, the two-orders-of-magnitude difference in these results needs understanding, and a SLD simulation would be useful for this purpose.

In the case of spin-lattice relaxation, Vaterlaus *et al.* [16]-[18] performed the only direct experiment on Fe to measure the relaxation time  $\tau_{sl}$ . The sample was hit by 20ns and 30ps laser pulses and the spin-polarized photoelectron emission was examined. The sample surprisingly remained ferromagnetic, even after the sample melted under the high-pulsed intensity of the 30ps pulses. The authors concluded that the upper and lower bounds of  $\tau_{sl}$  are 20ns and 30ps respectively. Subsequently, with an improved technique they obtained a  $\tau_{sl} = 100 \pm 80$  ps for Gd. However, no further work was done on Fe. A few years later, Scholl *et al.* [6] obtained a value of  $\tau_{sl} \approx 500$  ps for Ni thin film *via* a pump-probe experiment,

which is the same experiment in which  $\tau_{ss}$  had been measured. They found that two relaxation mechanisms are distinguishable in the demagnetization curve, which has a very short plateau in the short-time regime and a much longer gradual reduction at longer times. Theoretically, Hübner *et al.* [19]-[22] calculated for Gd a value of  $\tau_{sl} = 48$  ps by attributing the relaxation mechanism to the spin-orbit interaction caused by the magnetocrystalline anisotropy of the surface energy. However, the same mechanism does not seem applicable to bulk  $\alpha$ -Fe, in which the orbital moments of the  $3d$ -electron are nearly quenched, and the coupling between the orbital moments and the lattice *via* the anisotropic crystal field is weak [23]. The transfer of energy between the spin and the lattice subsystems *via* spin-orbit interaction should be negligible. The uncertainty surrounding  $\tau_{sl}$  in Fe can also be clarified using a SLD simulation.

In the following, microcanonical simulations using SLD are performed to investigate the rate of energy transfer within the spin subsystem and between the spin and lattice subsystems. A  $180^\circ$  domain wall system is presented as an example. The characteristics of spin-spin and spin-lattice relaxations obtained from this investigation will be used to understand the conflicting experimental results in the foregoing discussions. The detailed behavior of the system at the very beginning of the relaxation process very often depends on how the initial and boundary conditions are applied, such as the geometry of the simulation box. The role played by the simulation box in this regard will be discussed. Nevertheless, it must be emphasized that the origin of the ultrafast demagnetization [4]-[10] caused by electron thermalization and the corresponding electron-spin and electron-phonon

interactions are highly complex and are outside the scope of this thesis.

## 6.2 Equilibration Process – Part I (from Spin to Lattice)

Microcanonical simulations were performed for a system of 54000 atoms initially placed in a regular bcc lattice with the lattice parameter  $a = 2.8665 \text{ \AA}$ . The dimensions of the cubic simulation cell were  $30a \times 30a \times 30a$ , with periodic boundary conditions applied along the  $x$ ,  $y$  and  $z$  directions. The sample temperature was initially set at 0K, with a spin configuration such that all the spins in the left-hand side of the simulation cell ( $0 < x < 15a$ ) were all collinear and pointing upwards whereas the spins in the right hand side ( $15a < x < 30a$ ) were also all collinear but pointing downwards (Figure 6.1). Small perturbations are added into the spin subsystem to initiate the evolution, i.e. four atoms are randomly chosen and their spins are slightly deviated. The system was thermodynamically isolated. From the dynamics of the system, the characteristics of and mechanisms responsible for the adiabatic spin-spin and spin-lattice relaxations of the periodic array of  $180^\circ$  domain walls were studied. We should note that in the current model it is the scalar part of the inter-atomic potential and the exchange function  $J_{ij}(\mathbf{R})$  that fully define the dynamics of the atoms and their spins. The evolution follows the conservative dynamics equations 4.16 and 4.17, in which both the total energy and the total angular momentum of the system remain constant during the simulation.

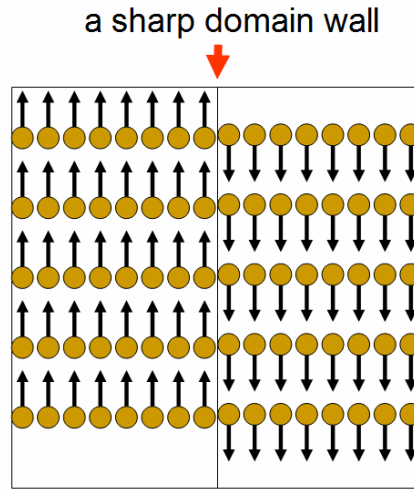
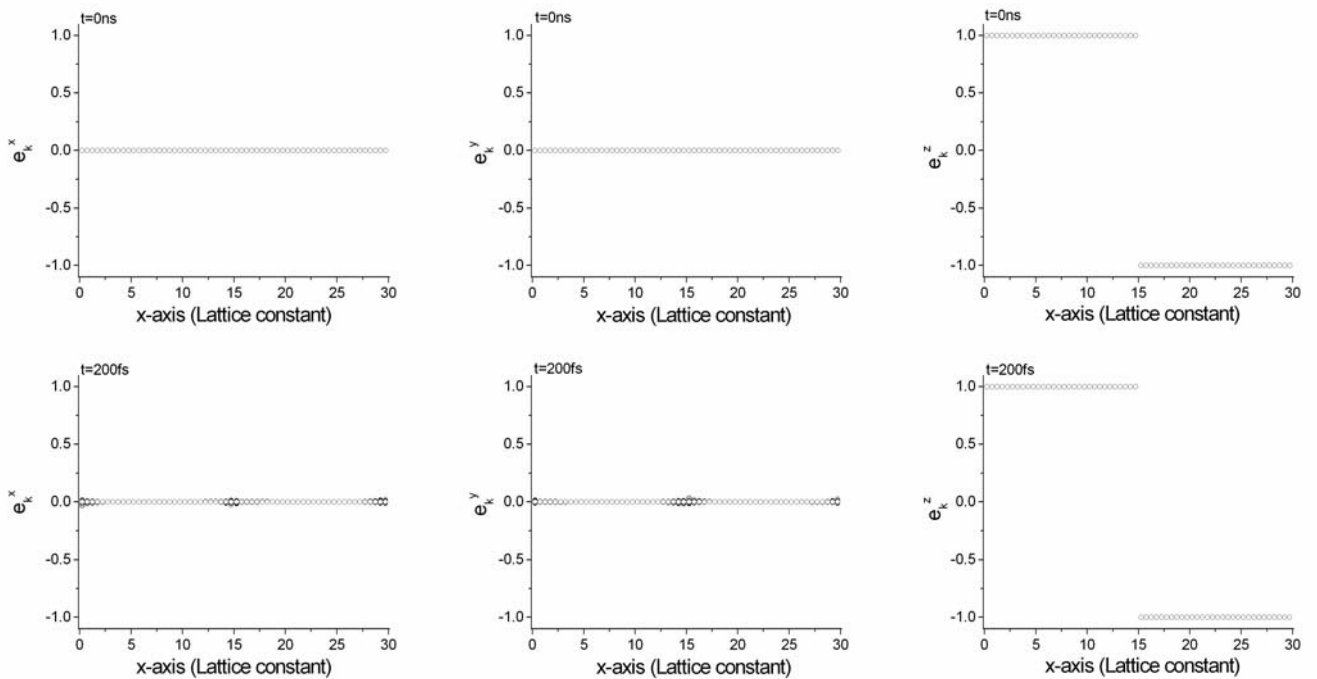


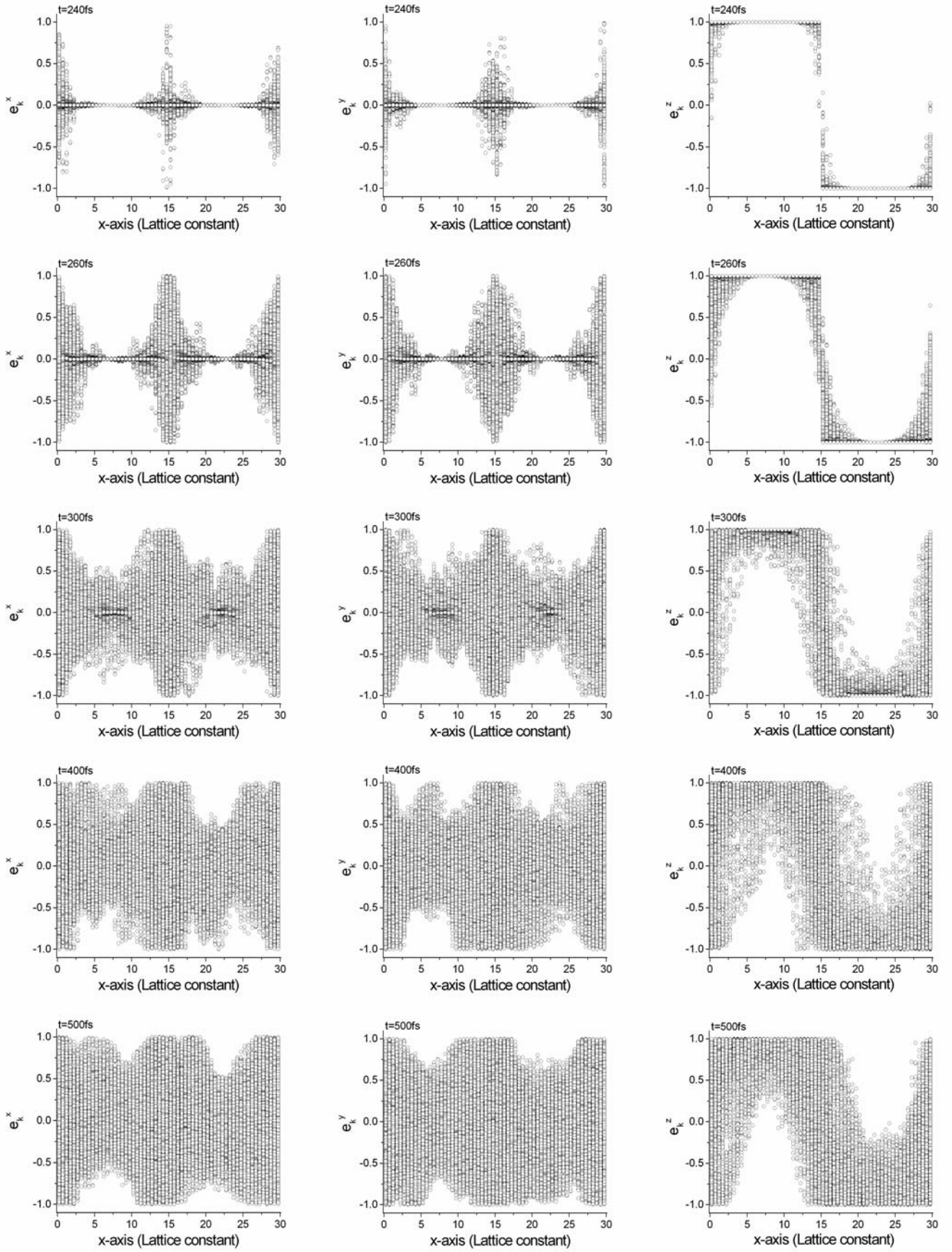
Figure 6.1 – Schematic picture of the unrelaxed  $180^\circ$  domain wall system. All the spins in the left-hand side of the simulation cell ( $0 < x < 15a$ ) pointed upwards whereas the spins in the right hand side of the cell ( $15a < x < 30a$ ) pointed downwards.

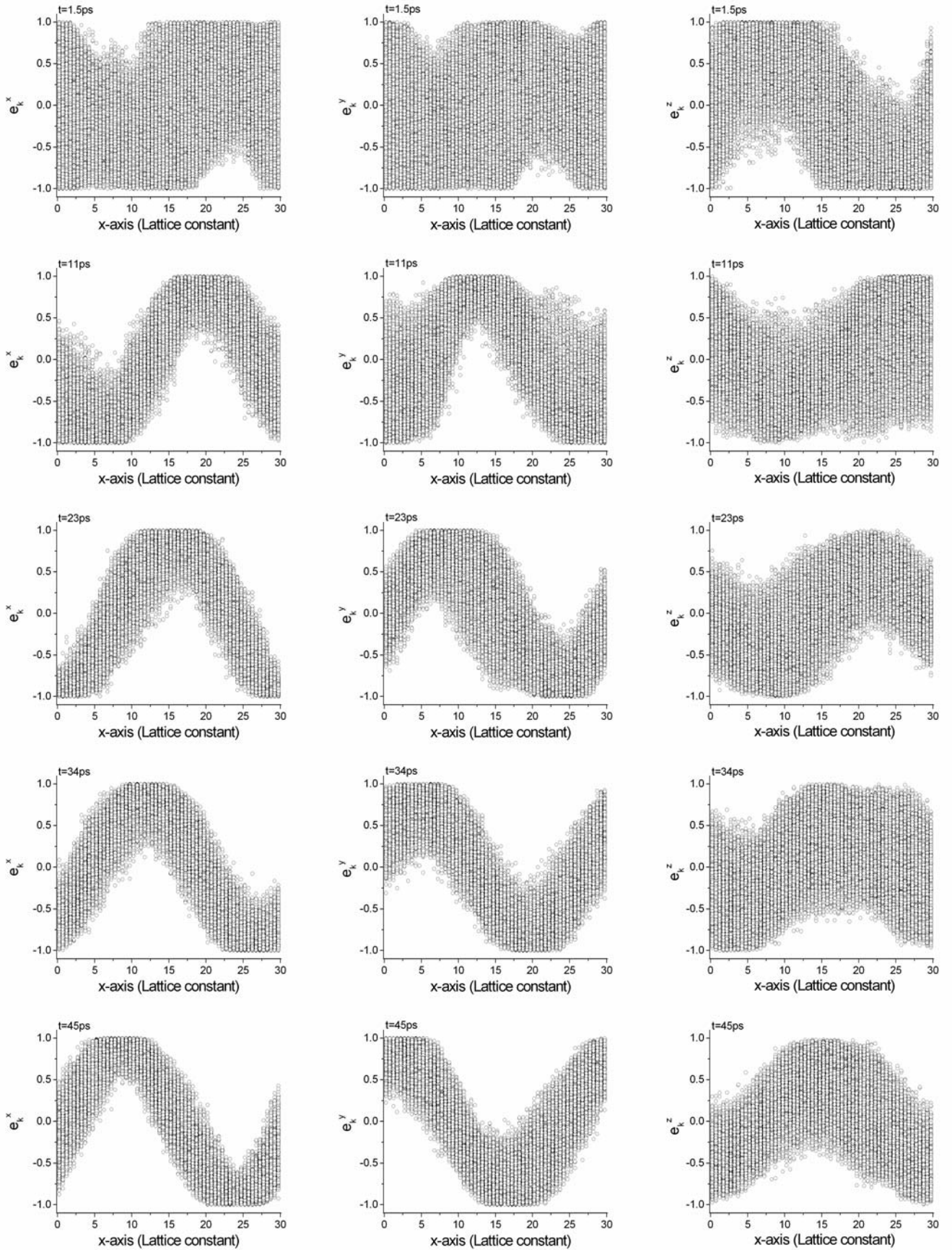
To describe the degree of collinearity of spins in a volume containing  $N$  atoms, it is convenient to introduce the spin collinearity parameter  $\xi_c = \frac{1}{N} \left| \sum_i \mathbf{e}_i \right|$ .  $\xi_c$  is a statistical measure of directional order in the spin subsystem characterizing collective orientations of spins irrespective of the magnitude of the magnetic moments. For example, if  $\xi_c = 1$  then the spin orientations are fully collinear, whereas  $\xi_c = 0$  corresponds to a fully disordered spin configuration.

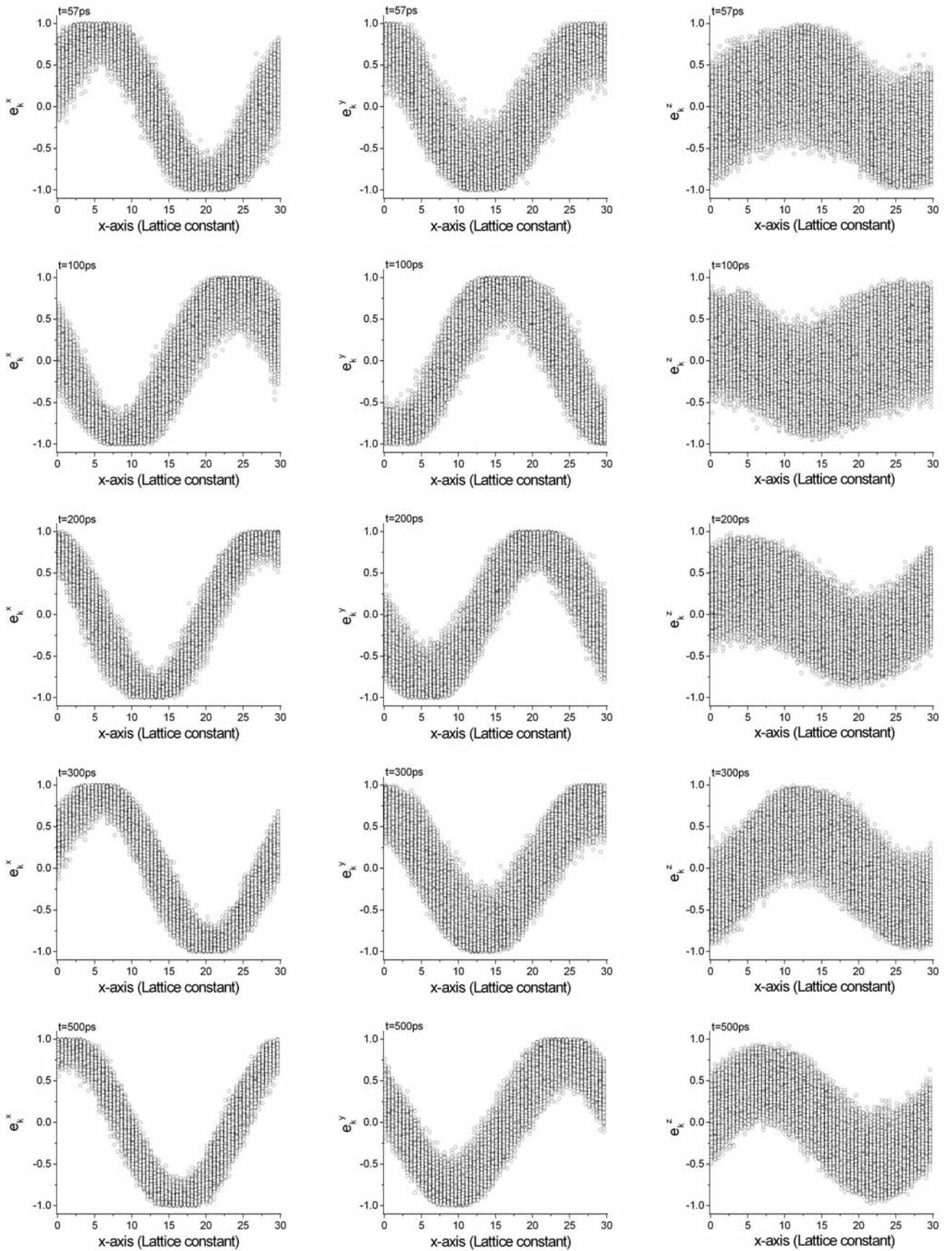
In the simulations considered here, the velocities of all the atoms were set to zero initially, and energy was stored solely in the spatially heterogeneous spin configuration of the domain wall. The system starts with a sharp magnetic boundary and evolves to maximize its entropy, subjected to the conservation of energy, linear momentum and angular momentum. The evolution of the spin system is shown in Figure 6.2. The initial spin configuration remains unchanged for about 0.24ps before the geometrical symmetry is broken by the lattice vibrations arriving

from nearest domain boundaries. Spin waves (magnons) then begin to appear and propagate with energy expended from the spin-spin interaction. The collinearity  $\xi_c$  of spins on planes parallel to the domain boundary starts to decrease and the spin configuration becomes progressively more disordered as the initial sharp domain boundary relaxes *via* magnon creation (spin-spin relaxation) during the next several picoseconds. By 1.5 ps, the original sharp domain boundary has already been relaxed substantially, and by 11 ps, there is no sign of it any more, and the orderliness has started to return. After that, the magnon density slowly reduces to come to an equilibrium value by transferring energy to the phonon subsystem (see further discussion below) as the relaxation of the spin system continues to proceed *via* spin-lattice relaxation, a process that lasts hundreds of picoseconds.









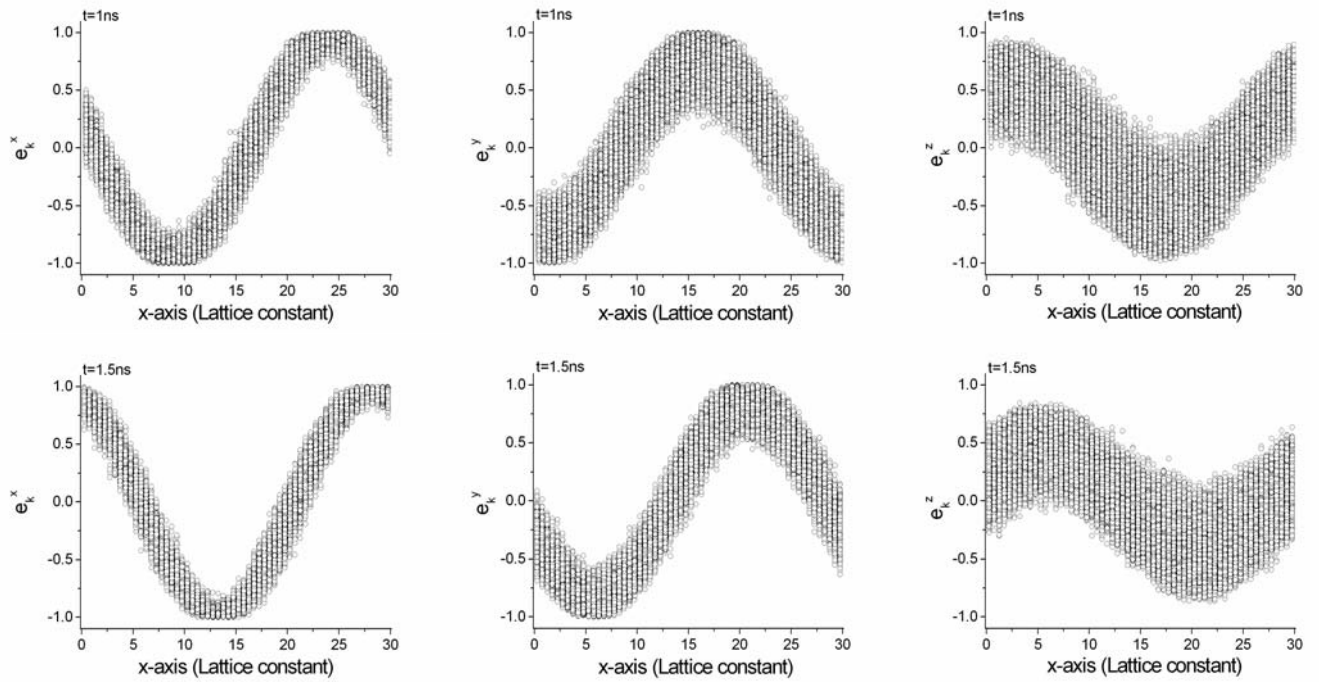


Figure 6.2 – Projections of the unit vectors of atomic spins corresponding to the microcanonical ensemble simulation of the dynamical relaxation of a  $180^\circ$  domain wall system.

Figure 6.3 shows the collinearity  $\xi_C$  of  $y$ - $z$  planes at different  $x$  (i.e. the  $n^{\text{th}}$  lattice plane) as a function of time in logarithmic scale. The most striking feature in this figure is the loss of collinearity as reflected by the reduction of  $\xi_C$  as the magnon number density increases during spin-spin relaxation in the picosecond range. The relaxation of the domain boundary proceeds initially through the creation of magnons that almost immediately redistribute, destroying  $\sim 90\%$  of the initial collinearity throughout the simulation region within a few tenths of a picosecond. Relaxation of the magnon system *via* magnon-magnon interaction (spin-spin relaxation) starts to re-establish the collinearity quickly. Over  $60\%$  of the collinearity is recovered within about 1-2ps. After that, spin-lattice interaction starts to become effective. The excitation of phonons by the magnons helps

re-establish the phonon-magnon equilibrium and produces further relaxation by energy transfer from the spin-subsystem to the lattice subsystem, producing further recovery of the collinearity. It is remarkable that more than 90% of the  $\xi_C$  has already been re-established at about 20 ps. Nevertheless, due to the mismatch between the timescales of evolution of the spin and lattice vibrations, the magnon-phonon coupling is relatively weak, resulting in a much longer total relaxation time with half-life  $\sim 0.25$ ns.

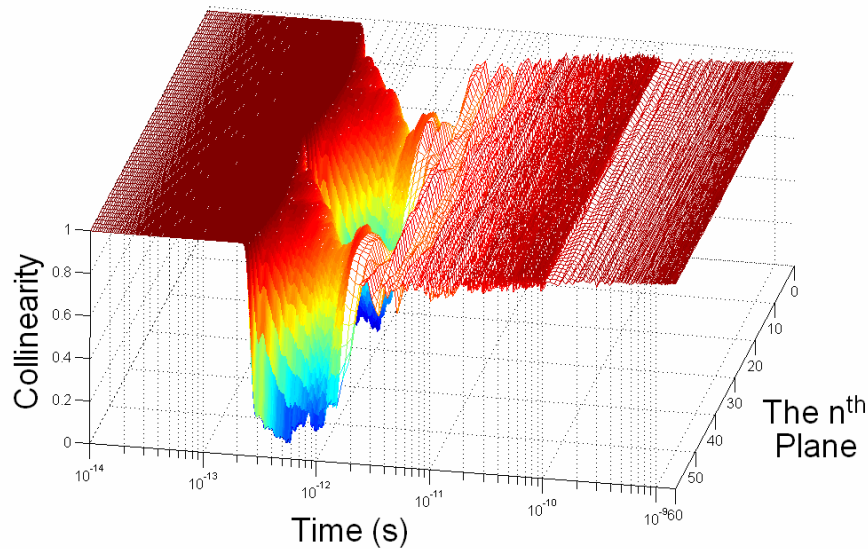
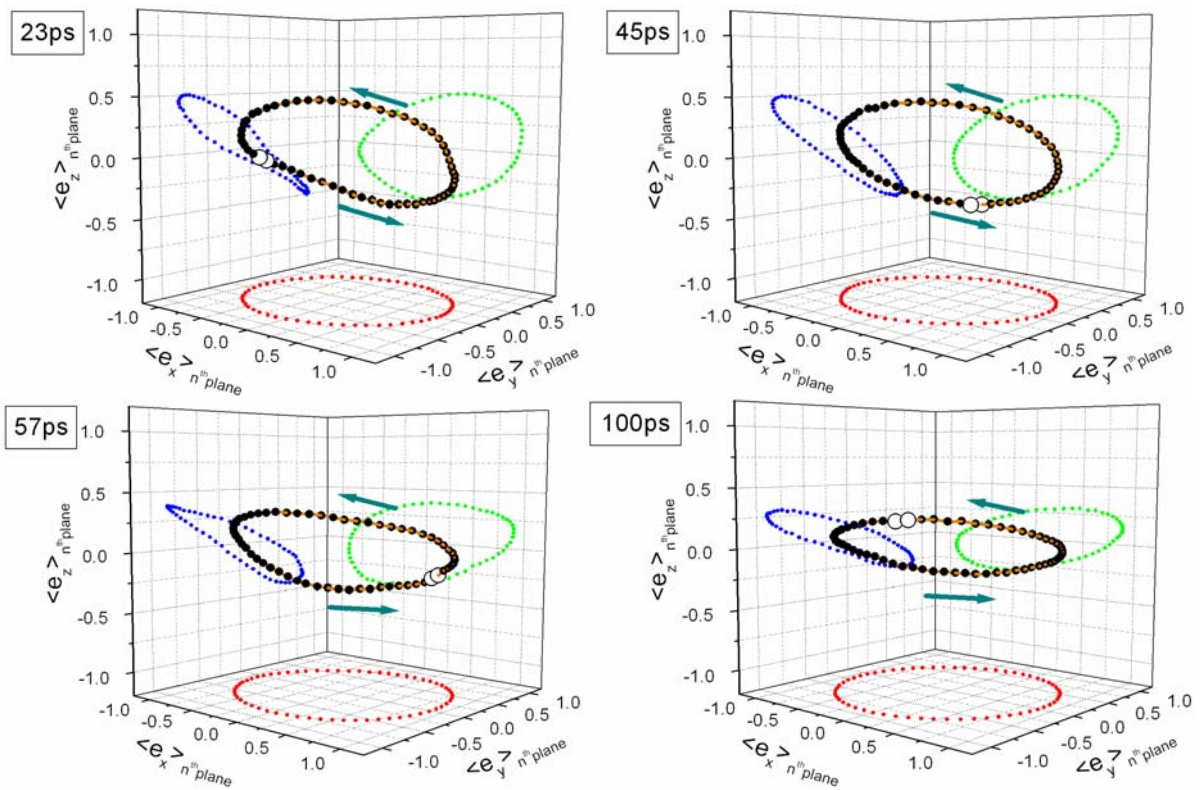


Figure 6.3 – The collinearity  $\xi_C$  of y-z planes at the  $n^{\text{th}}$  lattice plane along the x direction as a function of time in logarithmic scale.

To further understand the relaxation process and the re-established magnetic structure, Figure 6.4 plotted the average unit spin vectors of y-z planes along the x-axis, for several time instances. The projections on the x-y, x-z and y-z planes are also plotted. Projections on the x-y and x-z atomic planes represent the Neel's components, and those on the y-z plane the Block component, of the domain-wall structure. The two unfilled circles denote the two y-z planes at 0 and 29.5 lattice

constant spacing along the  $x$ -axis, i.e., the first and last planes in Figure 6.2. The arrows denote the sequence of atomic planes in between from left to right. The motion of these two circles reflects the motion of domain walls. It can be seen that the domain walls have mixed Neel-Block characters, which changes with time, and are already mobile as early as between 20 and 40 ps at least, but could be even earlier. Comparison of the magnetic structure at various times shows that the steady-state magnetic structure is probably dynamic and not static. However, this may instead be due to the periodic boundary condition, which is different from the real sample that must have a finite size and fixed boundaries.



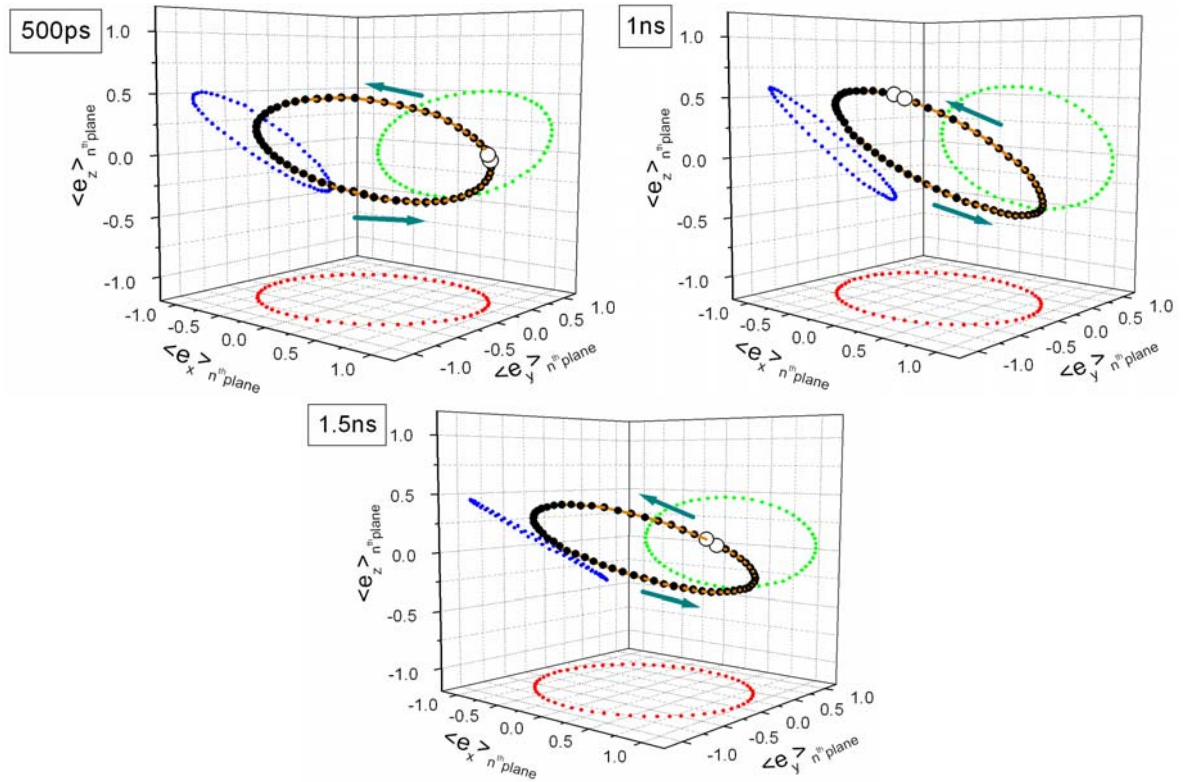
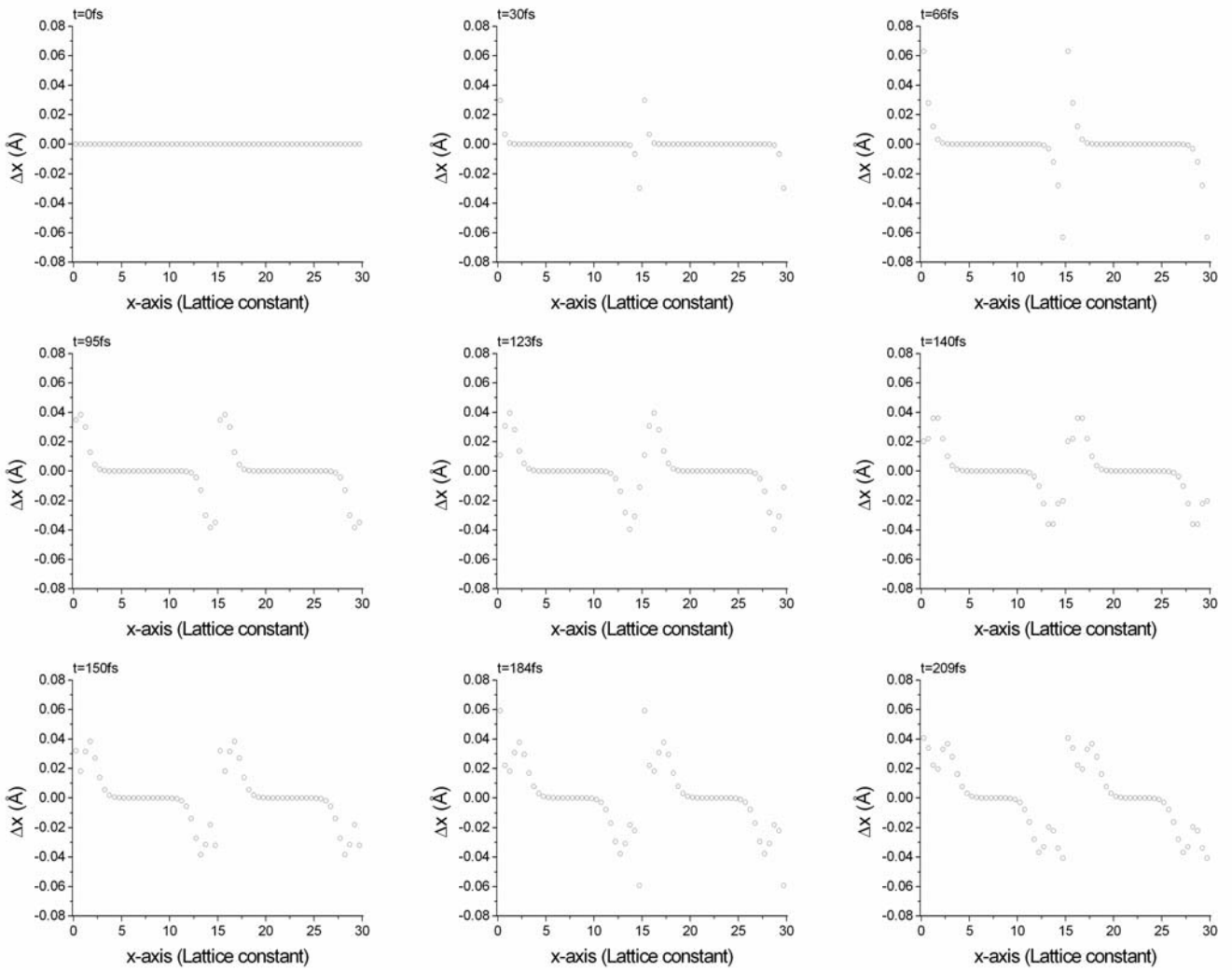


Figure 6.4 – Magnetic structure for various times after spin-spin relaxation. Each dot represents the direction of the unit vectors of atomic spins averaged over the  $n^{\text{th}}$  lattice plane parallel to the initial sharp domain boundary. The projections of the unit vectors in the three Cartesian directions are also shown. The unfilled circles denoted the first and the last planes. The dark green arrows represent the increase of plane index along  $x$  direction.

Contrary to the spins, the atoms in the immediate neighborhood of the domain boundary were already moving at  $\sim 0.03$  ps (Figure 6.5). The kinetic energy of the motion was supplied from the exchange interaction between the atoms, i.e., through the time variation of  $\mathbf{R}$  in the exchange parameter  $J_{ij}(\mathbf{R})$ . In this process, phonons with parallel wave vectors in the  $x$  direction are first created. The initial atomic oscillations can be seen to maintain planar coherency with wave vectors parallel to the  $x$  direction for approximately two cycles, each occurring on the Debye timescale of  $\sim 0.1$  ps (see Figure 6.6a). At about 0.24 ps, phonons with non-parallel wave vectors started to appear due to the scattering by the freshly

created magnons (see Figure 6.5), in which the associated phonon-magnon coupling is governed by the exchange interaction, with a magnitude proportional to  $J_{ij}$ . The loss of coherency and order from then on, as clearly shown in both Figure 6.2 and Figure 6.5, is due to the increase of the phonon density caused by the relaxation of the spin system towards equilibrium as phonon creation by magnon destruction continues.



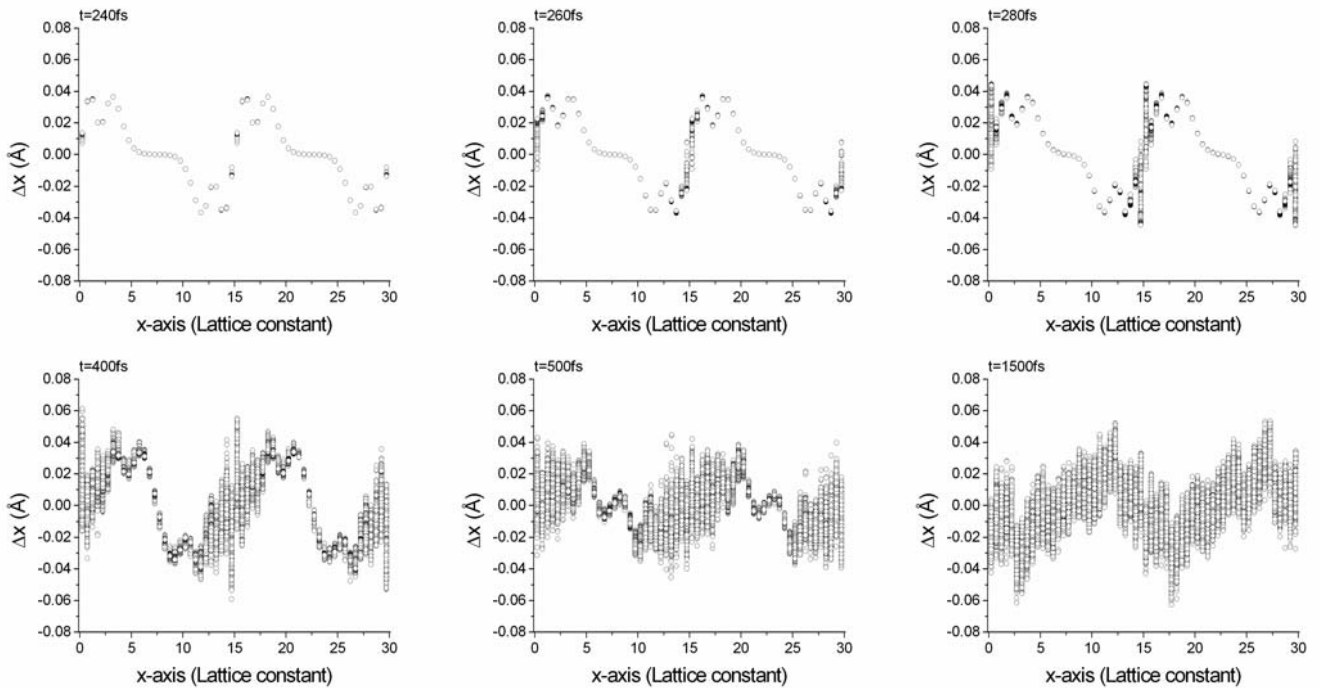


Figure 6.5 – The  $x$ -components of the deviations of atomic positions (i.e.  $\Delta x$ ) from their corresponding perfect lattice points along the  $x$  direction in the 10fs timescale.

The evolution of the various energy components are shown in Figure 6.6(a) to (d) at different time scales. The initial atomic oscillations, the beginning of the spin-spin relaxation (i.e., relaxation within the spin subsystem) at  $\sim 0.24\text{ps}$ , and at the same time the start of the equipartition of the lattice kinetic and the potential energies, can be seen from Figure 6.6(a) & (b) which shows in greater detail the rapid emergence of energy equipartition during the first few picoseconds, signaling the attainment of quasi-equilibrium of the lattice and spin subsystems separately. The increase of the equilibrated lattice total energy is driven primarily by the energy transfer from the spin subsystem *via* phonon-magnon scattering. At the same time, the spin subsystem gradually loses its order due to the continued accumulation of magnons, created to relax the initial sharp magnetic boundary. This produces a gradual increase of the system entropy (see Figure 6.2). The spin

system also evolves into a quasi-equilibrium configuration, which can be approximately described by an incoherent superposition of spin waves, in a timescale of about 20ps that the collinearity recovered 90% (Figure 6.3). This is consistent with the experimental results of Scholl *et al.* [6] and Koopmans *et al.* [7] in which  $\tau_{ss}$  was found to be about a few tens of picoseconds for Ni, where the  $\tau_{ss}$  is supposed to be shorter for Fe due to the stronger exchange coupling.

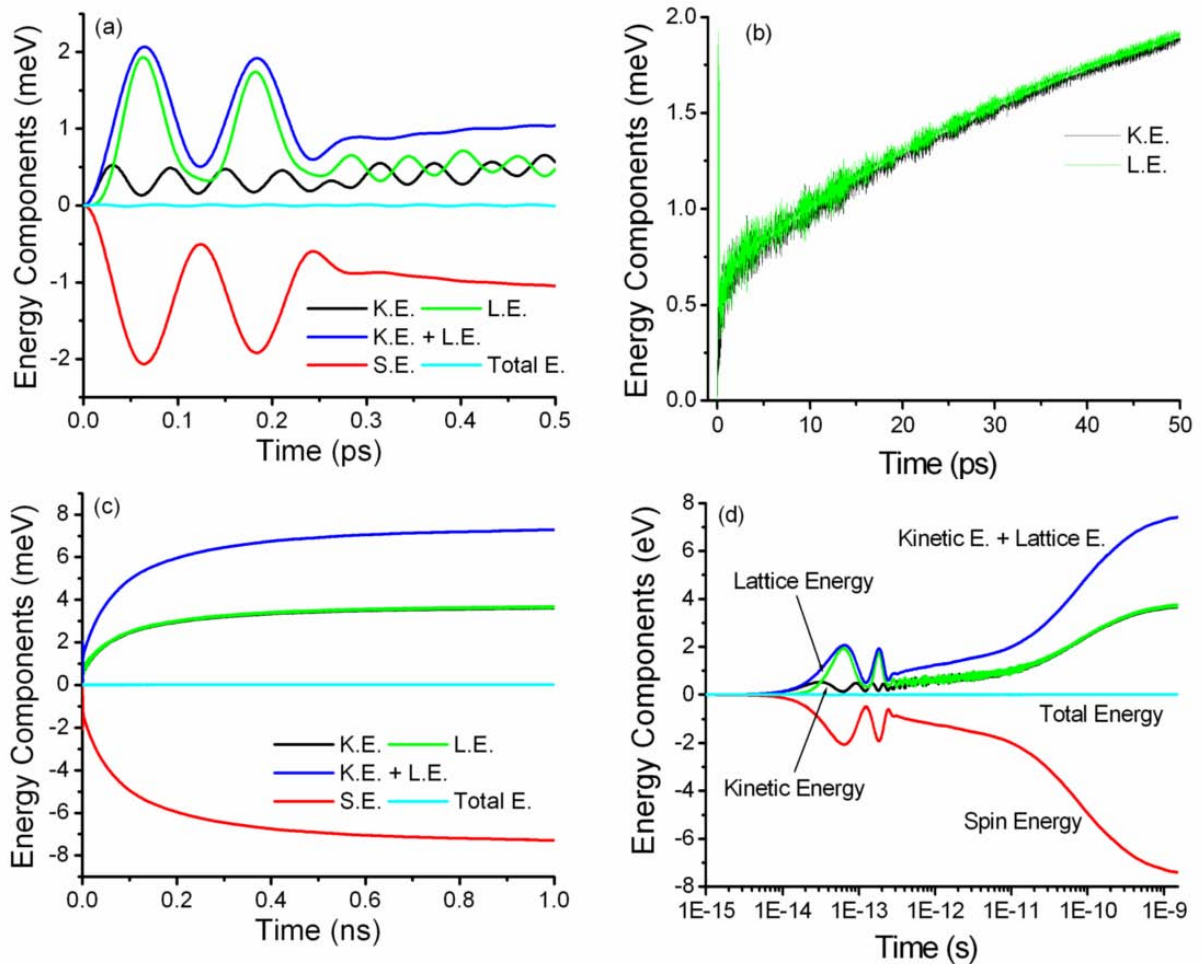


Figure 6.6 – Time evolution of the kinetic, potential and the spin energy contributions determined in simulations of dynamical relaxation of a sharp  $180^\circ$  domain wall and shown in the (a) 0.1 ps, (b) 10 ps and (c) 1 ns timescale. Figure (d) is the same as (c) but the  $x$ -axis is in  $\log_{10}$  scale. The velocities of all the atoms were initialized to zero at  $t=0$ . The curves show the variation of energy contributions with respect to their initial values. K.E. and L.E.

respectively refer to the kinetic and the scalar (lattice) part of the potential energy defined by equation 4.5, whereas the spin energy S.E. refers to the Heisenberg spin-spin interaction energy (last term in equation 4.5). The sum of the lattice and the spin energies equals the total energy of the system.

Figure 6.6(c) shows the continued energy transfer from the spin subsystem to the lattice subsystem *via* magnon-phonon interaction due to the supersaturation of magnons and the thermodynamic tendency to equilibrate the two subsystems. It can also be seen that the relaxation half-life for this process is approximately  $\sim 0.25\text{ns}$ , which is two-orders of magnitude longer than the relaxation time associated with magnon process i.e., the excitation of spin waves. The long duration of this relaxation process is derived from the relative weakness of the coupling between the spin wave and the lattice wave. The spin-lattice relaxation process is driven by the phonon-magnon coupling due to the exchange interaction. The nanosecond timescale of the phonon-magnon thermalization found in our simulations agreed with the analytical estimates by Sinha and Upadhyaya [24]. We note that the final equilibrated system configuration here has to be subjected to the conservation of total angular momentum of the spin subsystem, which puts a restriction on the modes of evolution of the spin subsystem. At this stage, the kinetic energy of the lattice subsystem gradually increased, corresponding to an effective temperature increase from 0K to about 28K ( $\sim 0.36\text{eV}$  per atom). By the time  $t = 1\text{ns}$ , the initial sharp domain structure becomes a collection of correlated spin waves with zero total angular momentum any time. Relaxation by further minimization of the free-energy is prevented by angular momentum conservation, and the relaxed spin configuration shown in Figure 6.2 continues to oscillate.

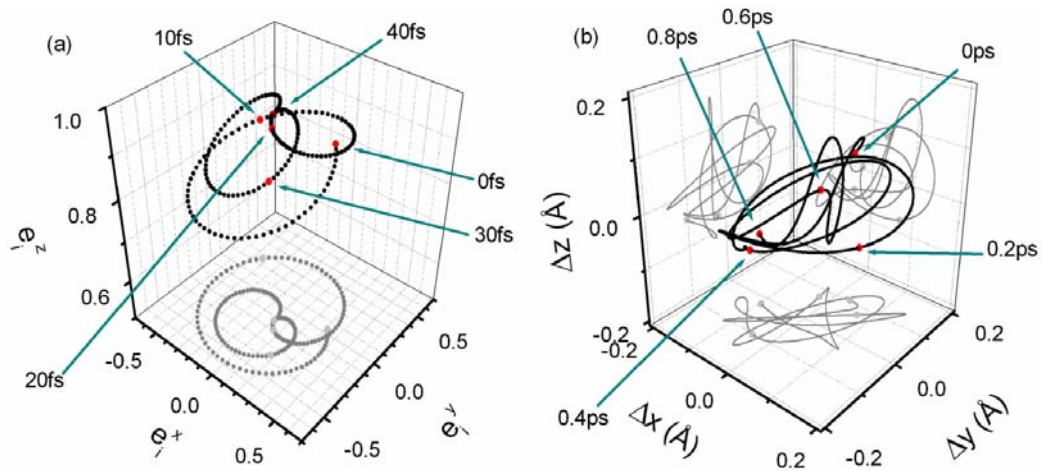


Figure 6.7 – The phase trajectory of an atom (left) and the spin direction (right) in a 54000 atom microcanonical simulation, thermally equilibrated at  $T = 300\text{K}$ .

At this point, it is instructive to compare the timescales characterizing the microscopic evolution of the atomic and the spin degrees of freedom. Each individual atom and each individual spin are coupled to the surrounding atoms and spins, and can be treated as closed classical thermodynamic systems evolving under a time-dependent external force. Figure 6.7 illustrates the phase trajectories for the coordinates and the spin direction drawn for an arbitrarily chosen atom in a system thermalized at 300K. (The thermalization process for a system of spin will be discussed in the next chapter.) One can see that the characteristic timescale of the quasi-periodic motion of an atom is of the order of 0.1ps (which is the inverse Debye frequency of the material), whereas the dynamics of precession of an atomic spin is characterized by a timescale about an order of magnitude smaller. This indicates a spin stiffness that is proportionately larger than that of the lattice. The fundamental difference between the 3D dynamics of atoms and the 2D dynamics of spins, and the mismatch between the frequencies of the quasi-periodic modes of motion shown in Figure 6.7, may be responsible for the relatively long

equilibration timescale characterizing the interaction between the spin and the lattice subsystems.

### 6.3 Equilibration Process – Part II (from Lattice to Spin)

The previous section considers a relaxation process in which energy flows from the spin to the lattice subsystem. Lattice vibrations or phonons are created by the phonon-magnon interaction. The spin-lattice relaxation takes about 1ns for the full equilibration. It is reasonable to ask the following questions. Are there relaxation processes in which energy flow in the reverse direction, i.e. from the lattice to the spin subsystem? Will the rate of relaxation be the same? To answer these questions the following simulations were performed, in which extra energy is introduced into the lattice subsystem after the spin-lattice system has been equilibrated.

The simulation is performed starting from the relaxed  $180^\circ$  domain wall system described in the foregoing section. Only the kinetic energy is rescaled to 300K instantaneously. Since the coupling between kinetic energy (K.E.) and the lattice potential energy or lattice energy (L.E.) is very strong, Figure 6.8(a) shows that the lattice subsystem is in quasi-equilibrium almost from the very beginning. Within the first 0.2ps, the K.E. pumped  $\sim 17\text{meV}$  to L.E., or equivalently, the temperature drops from 300K to 162K, as evidenced by the equipartition of the kinetic and potential energies. This can also be understood as a local energy transfer within the lattice subsystem, so it is extremely fast. At such a short timescale, a transient effect also happens where the energy flows from the spin to lattice subsystem,

which is contrary to intuition (Figure 6.8(b)). This is just because the  $\mathbf{R}$  in  $-(1/2)\sum_{i,j}J_{ij}(\mathbf{R})\mathbf{e}_i\cdot\mathbf{e}_j$  was changed abruptly by the instantaneous rescaling of K.E, which leads to the loss of S.E., without any phonon-magnon interaction happening here. In the timescale of 1ns, Figure 6.8(c) shows that energy flows from the lattice subsystem to the spin subsystem as expected, through the phonon-magnon interaction. When the new equilibrium is attained, the K.E. is equivalent to a temperature of 129K.

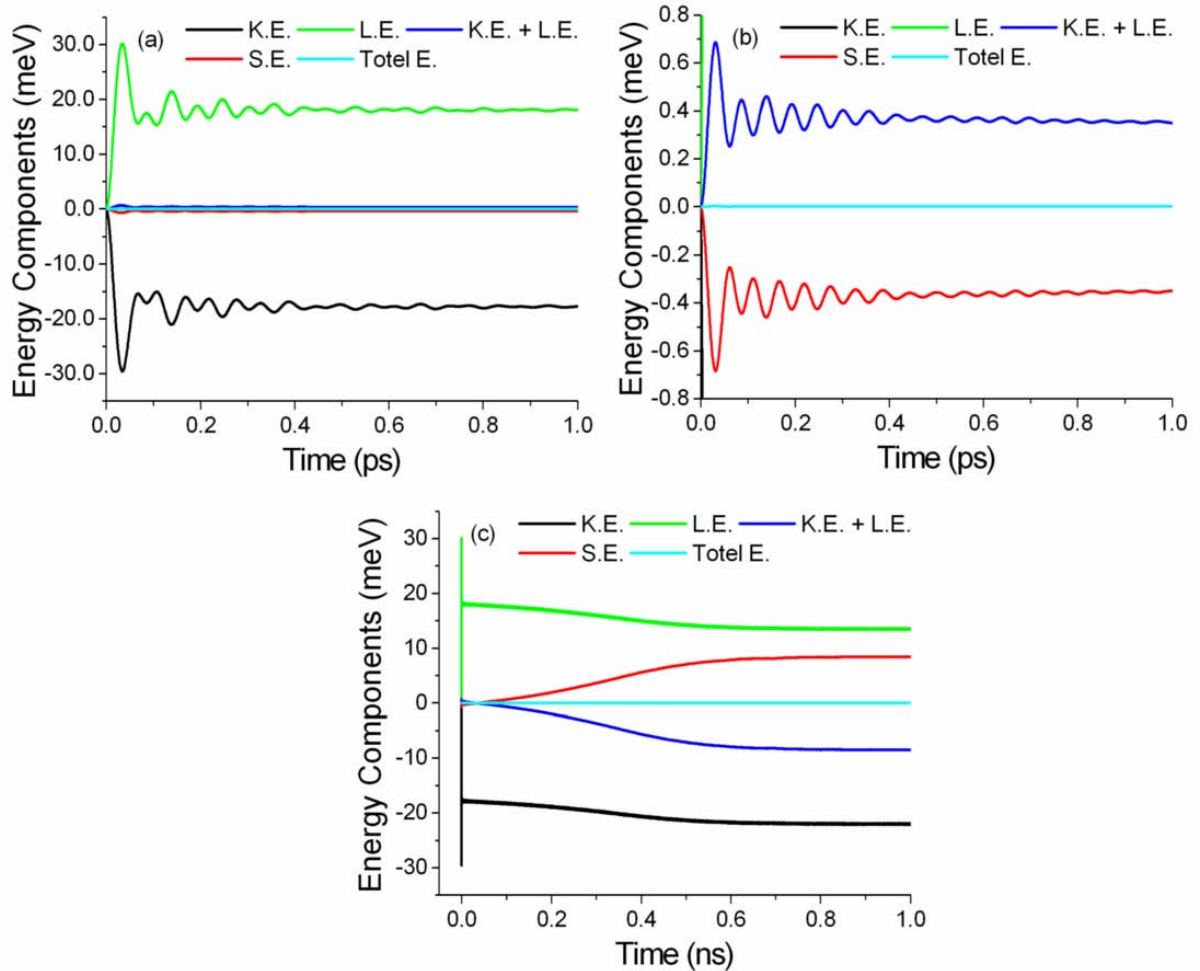


Figure 6.8 – After the relaxation of the 180° domain wall system, the kinetic energy of the atoms is rescaled to 300K instantaneously. The time evolution of the kinetic (K.E.) and potential energies (L.E.) of the lattice and the spin energy (S.E.) are shown in (a) & (b) in

timescales of 1 ps, and in (c) of 1ns, respectively. (b) is the same as (a) but with the y-scale enlarged about 40 times to show the details of the K.E. and L.E. and the energy equipartition. The curves show the variation of various energy components with respect to their initial values.

Results of further investigation done with the system rescaled to 100K and 600K are shown in (Figure 6.9(a)). The sample temperatures drop to 64K and 302K within the first 0.2ps, and eventually equilibrate at 55K and 237K respectively. The relaxation time is shorter for the higher temperature simulation. Since higher temperature means more phonons, it is expected to have a higher frequency of phonon-magnon scattering and so a stronger coupling between the spin and lattice subsystem. Furthermore, one can plot the half-lives against the inverse of temperature as in Figure 6.9(b). The half-lives are obtained by fitting the S.E. curves to the Boltzmann function that produces a sigmoidal curve, the one that rescaled to 600K is shown in Figure 6.9(c) as an example. From this, one can obtain the half-lives that are indeed at the inflexion points of the curves. Then, a linear least square fit is applied to the data, which may be extrapolated to 0.245ns when temperature goes to infinity. Together with these and previous simulations, it can be seen that the spin-phonon interaction can transfer energy in both directions with a characteristic time  $\tau_{sl}$  under 1ns. This agrees with experiments by Vaterlaus *et al.* [16]-[18] and Scholl *et al.* [6].

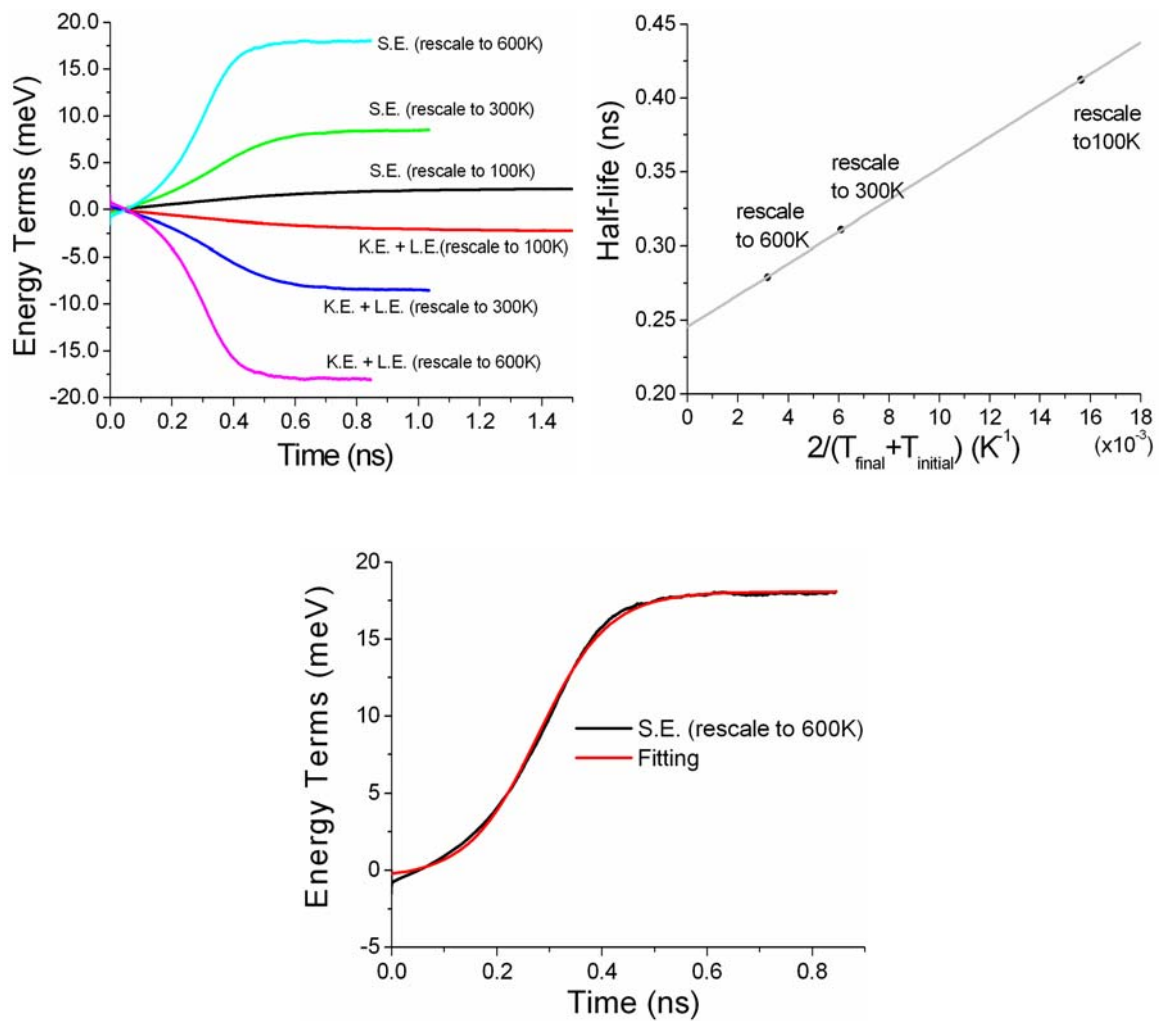


Figure 6.9 – (a) The time evolution of the kinetic + potential (scalar) and the spin energy terms are shown in 1ns timescale, where the kinetic energy is rescaled to 100K, 300K or 600K instantaneously after the relaxation of the  $180^\circ$  domain wall. The curves show the variation of energy terms with respect to their initial values. (b) The relationship between the half-life of the spin-lattice relaxation and the inverse of temperature. The half-life is obtained by fitting the curve of S.E. by the Boltzmann function that produces a sigmoidal curve.  $T_{\text{initial}} = 28\text{K}$  and  $T_{\text{final}} = 100\text{K}$ , 300K or 600K. The grey line is the linear least square fit to the data with the y-intercept at 0.245ns. (c) the one that rescaled to 600K is shown as an example, where the red curve is the fitting line.

## 6.4 Size Effects of the Simulation Box

All simulations considered in this chapter are for isolated systems under the

constraints of the conservation laws. Size effects may be important because of the finite volume of the simulation box and the imposition of the periodic boundary conditions. Indeed, such effects are evident in Figure 6.5, from which it can be seen that the spin wave had a wavelength equal to the  $x$ -dimension of the box, the minimum value allowed under the constraint of total angular momentum conservation.

Another issue concerns the dependence of  $\tau_{sl}$  on the dimensions of the simulation box. We consider this issue with the same set-up as the  $180^\circ$  domain wall system, but the edge length is reduced to  $16a$  and  $20a$ . Figure 6.10(a) shows the variation of the spin energy with respect to their equilibrium values. It reveals that all of the systems with different sizes response similarly under the same initial conditions. The red lines in Figure 6.10(b) are linear least square fits to the middle part of the curves. The half-life is then plotted against the inverse of the volume of simulation box in Figure 6.10(c). This shows clearly that smaller box has a shorter  $\tau_{sl}$ . This behavior may be due to a higher energy density of the initial spin configuration in the smaller box, i.e., more walls per unit volume. Due to the consequently higher magnon density, the magnon-phonon reaction rate increases, resulting in a faster relaxation and a shorter  $\tau_{sl}$ .

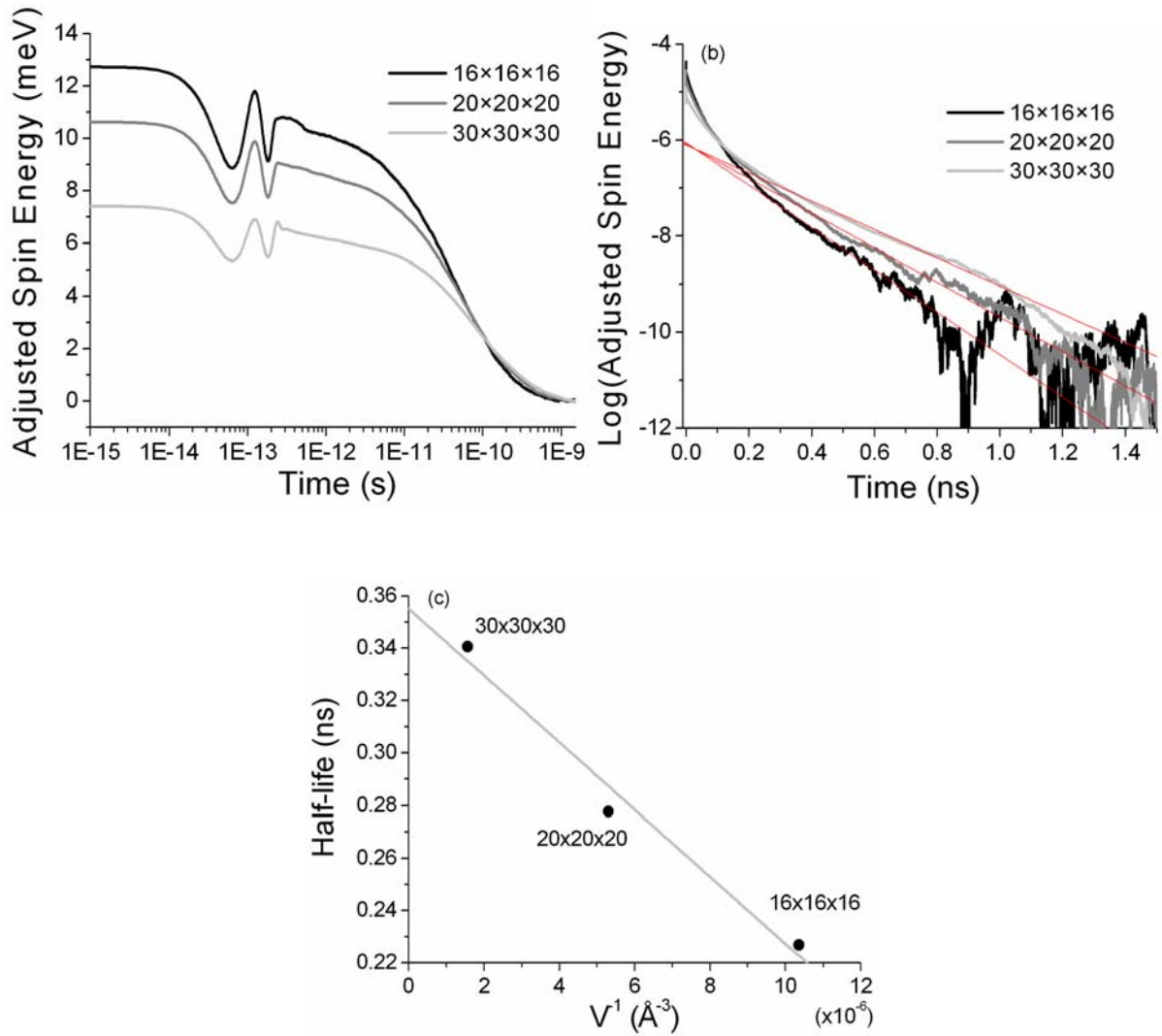


Figure 6.10 – (a) Time evolution of the spin energy terms determined in simulations of dynamical relaxation of a  $180^\circ$  domain wall with the edge length of the simulation box being  $16a$ ,  $20a$  and  $30a$ . The curves show the variation of spin energy with respect to their equilibrium values. The (b) is the same as (a), but the  $x$ -axis is in linear scale and  $y$ -axis is in log scale. Those red lines are linear least square fit to the middle part of the curves. (c) The relationship between the volume of the simulation boxes and the half-lives, where the half-lives are the inverse of the slope of those red lines. The grey line is the linear least square fit to the data points with the  $y$ -intercept at  $0.355\text{ns}$ .

## 6.5 Brief Conclusion

Microcanonical Spin-Lattice Dynamics simulations are performed. The relaxation of a  $180^\circ$  domain wall system is treated as an example. The relaxation is achieved mainly *via* the coordinate dependence of the exchange function that facilitates the transfer of energy between the spin and the lattice subsystems. For ferromagnetic  $\alpha$ -Fe, the current simulations suggest that the relaxation occurs in two stages, *via* two different mechanisms, namely, the spin-spin relaxation and the spin-lattice relaxation. The spin-spin relaxation is achieved *via* the production and destruction of spin waves, i.e., magnons, and re-establishing the collinearity with a characteristic time of few picoseconds. The spin-lattice relaxation is achieved *via* the production of phonons, either directly from the elastic relaxation of the sharp domain boundary through the action of the spin-oriented-dependent forces, or from the conversion of the supersaturated magnons, produced also directly from the magnetic relaxation of the domain boundary. It appears that the magnetic relaxation is a much faster process and creates a high supersaturation of magnons quickly at the beginning of the relaxation process. However, magnon creation does not allow magnetic energy to leave the spin subsystem, the spin system soon comes to a quasi-equilibrium, and further relaxation has to be through the conversion of magnons to phonons. Due to the mismatch between the timescales of evolution of the spin and lattice vibrations, the magnon-phonon coupling is relatively weak, resulting in a much longer total relaxation time lasting hundreds of picoseconds. The relaxation may, nevertheless, be speeded up by enhancing the phonon-magnon interaction with an increase of the phonon or magnon densities. The simulation scheme is shown to enable the energy flow from spin to lattice subsystem or vice

versa. The size of the simulation box does affect the relaxation speed *via* the initial energy density. Further investigation is needed. The effect of attaching a reservoir will be presented in the next chapter.

**REFERENCES:**

- [1] J. Van Kranendonk and J. H. Van Vleck, *Rev. Mod. Phys.*, **30**, 1 (1958)
- [2] C. Kittel and E. Abrahams, *Rev. Mod. Phys.*, **25**, 233 (1953)
- [3] Th. Gerrits, H. A. M. van den Berg, J. Hphlfeld, L. Bär and Th. Rasing, *Nature*, **418**, 509 (2002)
- [4] E. Beaurepaire, J.-C. Merle, A. Daunois and J.-Y. Bigot, *Phys. Rev. Lett.*, **76**, 4250 (1996)
- [5] J. Hohlfeld, E. Matthias, R. Knorren and K. H. Bennemann, *Phys. Rev. Lett.*, **78**, 4861 (1997)
- [6] A. Scholl, L. Baumgarten, R. Jacquemin and W. Eherhardt, *Phys. Rev. Lett.*, **79**, 5146 (1997)
- [7] B. Koopmans, M. van Kampen, J. T. Kohlhepp and W. J. M. deJonge, *Phys. Rev. Lett.*, **85**, 844 (2000)
- [8] B. Koopmans, M. van Kampen, J. T. Kohlhepp and W. J. M. deJonge, *J. Phys.: Condens. Matter*, **15**, S723 (2003)
- [9] T. Kampfrath, R. G. Ulbrich, F. Leuenberger, M. Münzenberg, B. Sass and W. Felsch, *Phys. Rev. B*, **65**, 104429 (2002)
- [10] D. Cheskis, A. Porat, L. Szapiro, O. Potashnik and S. Bar-Ad, *Phys. Rev. B*, **72**, 014437 (2005)
- [11] J. Wang, C. Sun, Y. Hashimoto, J. Kono, G. A. Khodaparast, Ł. Cywiński, L. J. Sham, G. D. Sanders, C. J. Stanton and H. Munekata, *J. Phys.: Condens. Matter*, **18**, R501 (2006)
- [12] T. L. Gilbert, *IEEE Trans. Magn.* **40**, 3443 (2004)
- [13] S. M. Bhagat, J. R. Anderson and L. L. Hirst, *Phys. Rev. Lett.* **16**, 1099 (1966)

- [14] S. M. Bhagat, J. R. Anderson and N. Wu, *Phys. Rev.* **155**, 510 (1967)
- [15] B. Heinrich, K. B. Urquhart, A. S. Arrott, J. F. Cochran, K. Myrtle and S. T. Purcell, *Phys. Rev. Lett.* **59**, 1756 (1987)
- [16] A. Vaterlaus, D. Guarisco, M. Lutz, M. Aeschlimann, M. Stampanoni and F. Meier, *J. Appl. Phys.*, **67**, 5661 (1990)
- [17] A. Vaterlaus, T. Beutler and M. Meier, *Phys. Rev. Lett.*, **67**, 3314 (1991)
- [18] A. Vaterlaus, T. Beutler, D. Guarisco, M. Lutz and F. Meier, *Phys. Rev. B*, **46**, 5280 (1992)
- [19] W. Hübner and K. H. Bennemann, *Phys. Rev. B*, **53**, 3422 (1996)
- [20] W. Hübner and G. P. Zhang, *Phys. Rev. B*, **58**, R5920 (1998)
- [21] G. P. Zhang and W. Hübner, *Phys. Rev. Lett.*, **85**, 3025 (2000)
- [22] R. Gómez-Abal and W. Hübner, *J. Phys.: Condens. Mater.*, **15**, S709 (2003)
- [23] J. Kuneš and V. Kamberský, *Phys. Rev. B*, **65**, 212411 (2002)
- [24] K.P. Sinha and U.N. Upadhyaya, *Phys. Rev.* **127**, 432 (1962)
- [25] C. Kittel, *Introduction to Solid State Physics*, 7<sup>th</sup> ed. (John Wiley & Sons, Inc, 1996) Page 473.

# Chapter 7: Spin Thermalization and Related Effects

## 7.1 Brief Introduction

Hübner and Zhang [1] pointed out that “*the concept of spin temperature is questionable not only due to the nonequilibrium, but also due to the absence of well-defined quasiparticle statistic for the spin.*”. Yet, the introduction of spin thermostat and the associated spin temperature is essential to the simulation of non-isolated systems for which conservation laws cannot be applied as in a micro-canonical ensemble. The concept of spin thermostat and spin temperature have been introduced in Chapter 4 of this thesis *via* Langevin spin dynamics [2],[3] using the fluctuation-dissipation theorem (FDT) [4],[5]. In this scheme, temperature is incorporated in the numerical scheme of Spin-Lattice Dynamics (SLD) for classical atomic spins, assuming a Gibb’s energy distribution. Both energy and angular momentum of the spin subsystem and the reservoir are allowed to interchange to establish thermodynamic equilibrium under specified conditions. In this chapter, several applications aimed to test the feasibility of the Langevin SLD model at elevated temperatures will be reported.

As a first example, a bulk sample of bcc iron is considered. It was isothermally and isobarically heated up to thermal equilibrium at various temperatures from 0K, when all spins are initialized with perfect collinearity  $\xi_C = 1$ . In this case, the experimental isothermal magnetization curve is

well-known to be describable over a broad range of temperatures in terms of the mean-field classical approximation. Since the spin equilibration process in the Langevin SLD simulation is governed by a physically meaningful coupling constant  $\eta$  (equation 4.30), the characteristic time of the process reveals in detail the response of the system as a function of temperature. The spatial correlation and time-correlation functions of spin orientations can also be examined.

In the second example, magnetic thin films of bcc Fe are considered at finite temperatures. These thin films are of technological importance and have found important applications in magneto-electric devices, such as those based on giant magneto-resistance. In ferromagnetic iron, both *ab-initio* calculations [6],[7] and calculations using the newly developed magnetic many-body potential [8] predict that the magnetic moments at the surface are enhanced. Indeed, the reduction of the coordinate number on the metal surface leads to band narrowing that should increase the corresponding magnetic moment. Experimental results [9]-[11], on the other hand, only support an enhancement of magnetization at very low temperatures. Reduction of the magnetization was observed even at temperatures as low as room temperature. Hasegawa [12] partially resolved this problem by considering the spin fluctuations at the surface. He calculated the average magnetic moment layer-by-layer by the functional integral method within the static and single-site approximation. Although his calculated bulk Curie temperature  $T_c$  is double the experimental value, he did successfully show the enhancement of the average magnetic moment on the surface at low temperatures, and the reduction at high temperatures. In this chapter, the magnetization in a Fe thin film is investigated within the scheme of SLD. It will be shown that with spin-wave

excitation taken into account magnetization on the film surface indeed should behave as experimentally observed.

In a third example, Langevin SLD simulations are tested in cases involving magneto-mechanical effects, such as exhibited in thermal expansion and elasticity. It is well-known [13]-[16] that magnetic contributions made up a significant part of the total free energy, and would affect the mechanical properties significantly. Hasegawa and Pettifor [13] and Friák *et al.* [14] showed that magnetism is essential to stabilize the bcc phase of Fe at low temperatures. Hasegawa *et al.* [15] calculated the temperature dependence of elastic constants with the influence of magnetic moments, and observed the softening of the tetragonal shear constant  $C'$ . Dever [16] noticed in his experiments that the nonlinear temperature dependence of the elastic constants is associated with the amount of spin alignment. Our simulation results are expected to be able to shed some light in this regard.

## 7.2 Temperature-Dependent Spontaneous Magnetization

Isothermal-isobaric simulation using the Langevin SLD scheme is performed to understand the thermal equilibration process of the spin subsystem at various temperatures. The simulation cell consists of 54000 atoms initially forming a regular bcc lattice with the lattice parameter  $a = 2.8665 \text{ \AA}$ . The initial dimensions of the cell are  $30a \times 30a \times 30a$ , with periodic boundary conditions applied along  $x$ ,  $y$  and  $z$  directions. All spins are initially perfectly collinear. The simulation cell is first allowed to expand or shrink under stress-free condition until a steady-state

configuration is established. The degree of collinearity  $\xi_c$  of spins of a group of  $N$  atoms is defined as the magnitude of the mean unit spin-vector of the group,

i.e.,  $\xi_c = \frac{1}{N} \left| \sum_i \mathbf{e}_i \right|$ , as defined in the previous chapter. The mean magnetization of

the group is the product of  $\xi_c$  and the averaged magnitude of the atomic magnetic moment defined by the magnetic potential.

Figure 7.1 shows the collinearity of the thermalized spin subsystem at various temperatures, calculated using Langevin SLD as a function of time with perfectly collinear initial spins ( $\xi_c = 1$ ). The simulation traces the dynamics of the thermalization process of the spin subsystem interacting with a thermostat. The strength of the coupling to the thermostat is determined by a damping constant  $\eta$  (Equation 4.30) set to  $10^{-3}$ . The thermalization process was allowed to continue for a sufficiently long period of time to ensure equilibrium. It can be seen that at low temperatures, equilibrium values of  $\xi_c$  are finite, but decreases with increasing temperature. For temperatures higher than about 1100K, collinearity vanishes with  $\xi_c$  fluctuating around zero, signifying a disordered spin state. We should note that  $\xi_c$  is positive definite and cannot drop below zero. The residual positive collinearity is due to the randomly fluctuating spins.

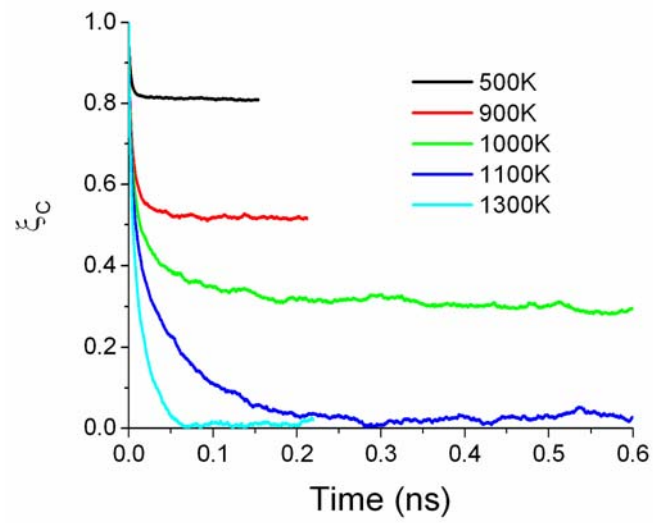


Figure 7.1 – Examples of dynamical simulations performed using the Langevin SLD algorithm for  $\eta = 10^{-3}$  for several temperatures of the thermostat.

Physically, it is expected that the magnitude of  $\eta$  only affects the duration of the transients, but not the values of  $\xi_C$  at equilibrium. To show that this is indeed the case, isothermal relaxations were performed for two different values of  $\eta = 10^{-3}$  and  $10^{-4}$ , respectively, at the thermostat temperature of 300K. Figure 7.2 shows the resulting evolution of  $\xi_C$  as a function of time. It can be seen, as expected, that the value of the damping constant only affects the speed of equilibration, and not the final equilibrium value of  $\xi_C$ .

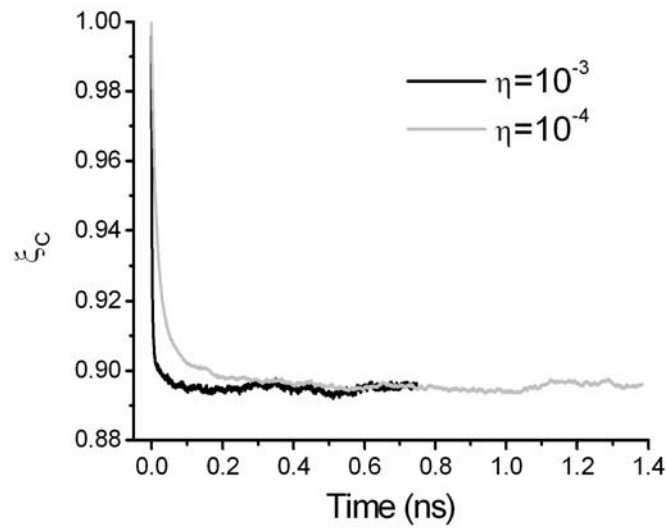


Figure 7.2 – Examples of Langevin SLD simulation of thermal relaxation at  $T = 300\text{K}$  of the spin subsystem interacting with the thermostat, performed for two different values of the damping constant.

It is obvious that in Figure 7.1, the characteristic time for thermal equilibration process varies for different temperatures. The half-life of the equilibration process can be obtained approximately as shown in the Figure 7.3(a) and plotted as a function of time in Figure 7.3(b). In Figure 7.3(a), the logarithm of  $\xi_c$  is plotted against the time after the minimum collinearity is first subtracted. For low temperatures, e.g. 500K, a linear least square fit to the long-time part of the curve, and the negative of the inverse of the slope is the estimated thermalization half-life time. When the temperature is higher than the  $T_c$ , e.g. 1300K, the collinearity already drops to zero, and it is meaningless to analyze the long-time part of the curve because it only represents totally disordered random fluctuations. The linear least square fit then refers to the flat part of the curve where a finite degree of collinearity still sustains. After plotting and fitting for temperature from 0K to 1700K, Figure 7.3(b) shows a peak at around 1000K to 1100K, near  $T_c$  of Fe. It reveals that near the phase transition point the magnetic order of the system would

be most persistent, i.e., rigid.

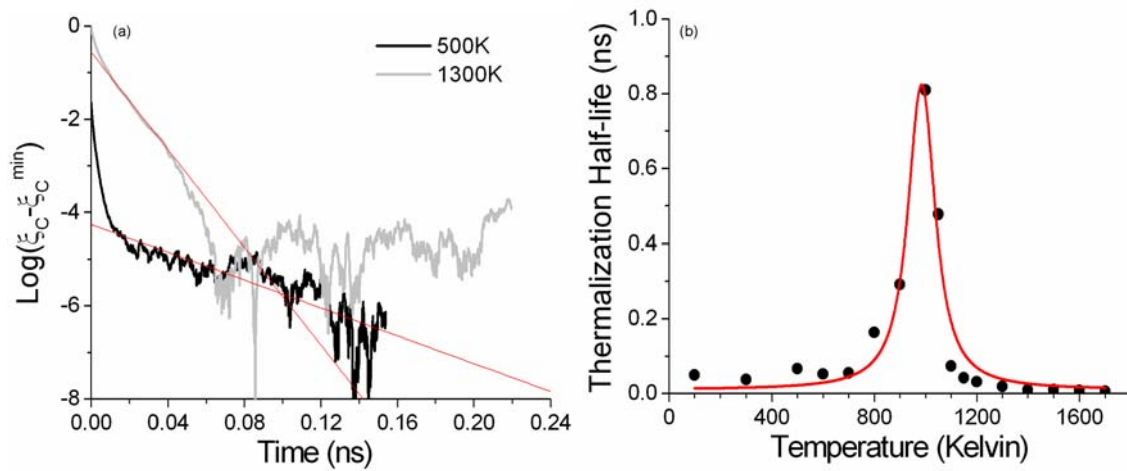


Figure 7.3 – (a) Logarithm of the collinearity minus the minimum value of the curve as a function of time at 500K and 1300K. The red straight lines are linear least square fit to the flat part of the curves, where their slopes are approximately the negative of the inverse of the thermalization half-life times. (b) The thermalization half-life was presented as a function of temperature. The red line is a Lorentzian peak function fitted to data for the purpose of eyes guiding only.

Unlike a Monte Carlo simulation, the dynamic simulation of thermalization performed here is derived from the Fokker-Planck equation, which “*does not merely label the sequential order of generated states when sampling the phase space, but is related to physical time.*” [3]. Although the rate of thermalization is a function of  $\eta$  as shown in Figure 7.2, the general trend of the characteristic time of thermalization as a function of temperature should not depend on  $\eta$ . The thermalization-time peak may be understood as arising from the intense competition between the magnetic order, favored by internal energy minimization, and the disorder favored by entropy maximization at higher temperatures near the phase transition point, which tends to prolong the duration for the system to reach equilibrium.

In Figure 7.4, the calculated equilibrium values of the spin collinearity  $\xi_C$  are plotted as a function of absolute temperature. Also shown on the same graph are the corresponding experimental data [17] and the average magnetization curve predicted by the mean-field approximation, to be further described in the following.

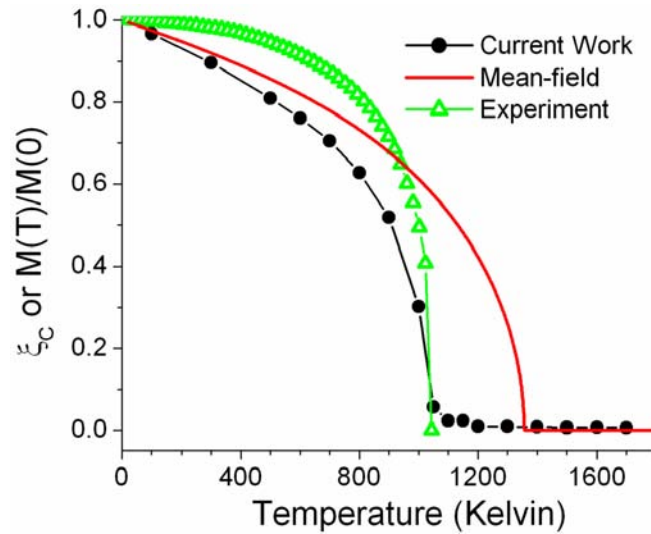


Figure 7.4 – The equilibrium magnetization curve showing the average atomic spin evaluated dynamically using canonical ensemble simulations for various temperatures. Experimental data were taken from Ref. [17] and the mean field approximation curve was evaluated using the method described in text.

The experimental  $T_c$  of bcc Fe is 1043K. The calculated mean-field value of  $T_c$  obtained using the exchange function  $J_{ij}$  adopted in this thesis is 1357K. Our simulations predict a  $T_c$  between 1050K and 1100K. Given that these results are based on the same *ab-initio* form for the exchange function, it is encouraging that the present treatment correctly describes the order/disorder nature of the ferro/paramagnetic transition in bulk bcc iron, which also lends confidence to the SLD algorithm. One may note that the calculations presented here are the first successful *dynamical* simulation of the ferro/paramagnetic phase transition,

performed *via* a method in which the reduction of spin collinearity with temperature is related to the spin-lattice coupling caused by the space dependence of the interatomic exchange interaction. The trend of the temperature dependence of the calculated spin collinearity curve is closer to the classical mean-field spin approximation than to the experimental data. This finding corroborates the conclusion of Hubbard [18] who interpreted this deviation as the result of the use of a classical statistical approach to the treatment of a (real) quantum system of atomic spins. The higher  $T_c$  in the mean-field calculation is reasonable, since it does not include the spin wave excitation in the  $z$ -direction.

For the sake of completeness, the following page will be used to review the mean field theory of magnetization for a classical spin system [18],[19]. The Hamiltonian for the spin subsystem in the Heisenberg form is given by  $H_{spin} = -(1/2) \sum_{i,j} J_{ij} \mathbf{e}_i \cdot \mathbf{e}_j$ . The mean field theory assumed that the effective field is spatially homogeneous and that all the spins are aligned. The spin energy for a particular atom  $k$  is now

$$\begin{aligned}
 E_k &= -\frac{1}{2} \sum_i J_{ik} \langle \mathbf{e}_i \rangle \cdot \mathbf{e}_k - \frac{1}{2} \sum_i J_{ki} \mathbf{e}_k \cdot \langle \mathbf{e}_i \rangle \\
 &= -\frac{1}{2} \sum_i J_{ik} e^z e_k^z - \frac{1}{2} \sum_i J_{ki} e_k^z e^z \\
 &= -H_{eff} e_k^z
 \end{aligned} \tag{7.1}$$

where  $H_{eff} = e^z \sum_i J_{ik}$ . It is to note that only the  $z$  projection of spin  $\langle \mathbf{e}_i \rangle = e^z$  is non-zero. With a partition function for classical particles,

$$\begin{aligned}
Z(\beta) &= \int_{-1}^1 \exp\left(-\beta(-H_{\text{eff}}e_k^z)\right) de_k^z \\
&= \int_{-1}^1 \exp(\zeta e_k^z) de_k^z \\
&= \frac{1}{\zeta} (\exp(\zeta) - \exp(-\zeta))
\end{aligned} \tag{7.2}$$

where  $\zeta = \beta H_{\text{eff}} = H_{\text{eff}}/k_B T$ . The ensemble average value of spin as a function of temperature is

$$\begin{aligned}
e^z &= \frac{\partial \ln Z(\zeta)}{\partial \zeta} \\
&= \frac{\exp(\zeta) + \exp(-\zeta)}{\exp(\zeta) - \exp(-\zeta)} - \frac{1}{\zeta}
\end{aligned} \tag{7.3}$$

The  $e^z$  can be obtained by iteration starting with initial values following the superheating path and using the exchange parameters for the 1<sup>st</sup> and 2<sup>nd</sup> nearest neighbors, i.e.  $\sum_i J_{ik}(R_{ik}) = 8J_{ij}(\sqrt{3}a/2) + 6J_{ij}(a)$ . Eventually, we can arrive at the magnetization curve shown in Figure 7.4

### 7.3 Correlation functions

An order/disorder ferro/paramagnetic phase transition is characterized by the disappearance of the long-range order in the spin subsystem. To investigate the remaining short-range order in the spin subsystem at equilibrium, the corresponding spatial spin-spin correlation functions are calculated and shown in Figure 7.5 for the first twelve nearest neighbor (N.N.) shells. It can be seen that the

1<sup>st</sup> and 2<sup>nd</sup> nearest neighbors are strongly correlated even for temperatures higher than  $T_c$ . The correlation functions remain non-negative for all the sites up to the 12<sup>th</sup> nearest neighbor.

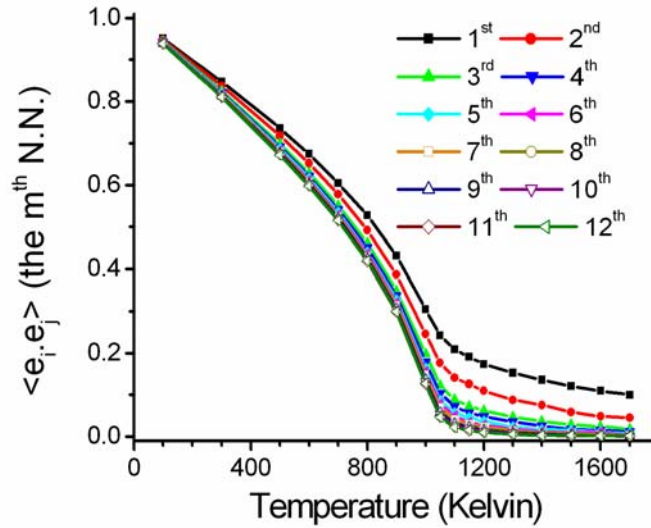


Figure 7.5 – The spin-spin spatial correlation functions shown as functions of absolute temperature for the 1<sup>st</sup>, 2<sup>nd</sup> ... 12<sup>th</sup> nearest neighbour atoms.

To analyze the dynamics of atomic spins at thermal equilibrium, the time-dependent spin-spin autocorrelation function

$$\langle \mathbf{e}_i(t) \cdot \mathbf{e}_i(t+\tau) \rangle = \frac{1}{N} \sum_i \mathbf{e}_i(t) \cdot \mathbf{e}_i(t+\tau)$$

is calculated from a NVE model of a thermally equilibrated ensemble. Figure 7.6 shows the oscillating behavior of  $\langle \mathbf{e}_i(t) \cdot \mathbf{e}_i(t+\tau) \rangle$  found for short timescales of the spin precession trajectories similar to that shown in Figure 6.7, where it can be seen that the transverse component of the spin orientation vector increases due to the increase of the average precession angle treated as a function of temperature. At  $\sim 700\text{K}$  the fluctuations shown in Figure 7.6 reach a maximum and then gradually die out. It is to be noted that in the limit  $\tau \rightarrow \infty$  the autocorrelation function asymptotically

approaches the square of the spin collinearity at equilibrium.

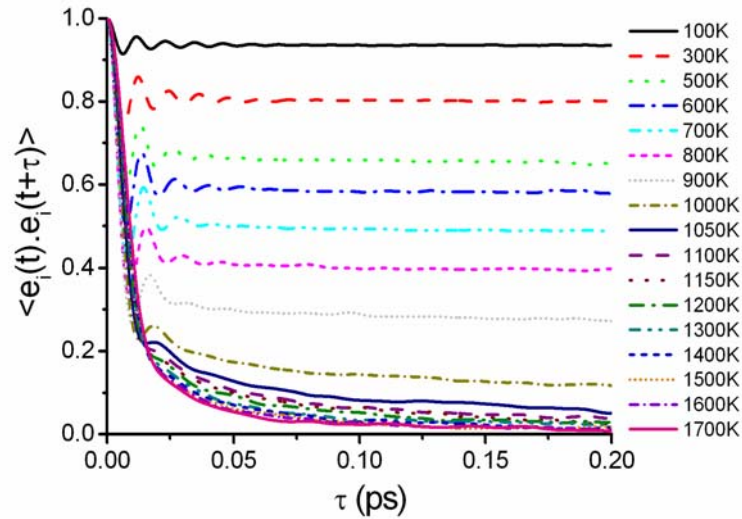


Figure 7.6 – The time-dependent spin-spin on-site autocorrelation functions evaluated dynamically using microcanonical ensemble simulations performed for fully thermalized initial configurations.

To estimate the spin autocorrelation dephasing time, an exponential decay function was least-square fitted to the upper envelope curve for low temperatures, and to the entire curve for high temperatures. The results are plotted in Figure 7.7, which shows that the spin autocorrelation dephasing time was approximately 10fs. This result corroborates very well the findings of Hübner and Zhang [1] who estimated, by calculating the optical susceptibility of metallic Ni, that the dephasing time was of the order of 10fs.

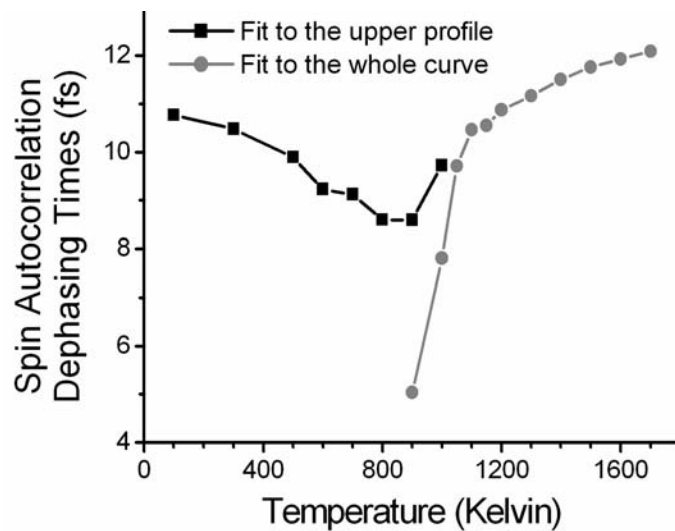


Figure 7.7 – The spin autocorrelation dephasing times for the curves shown in Figure 7.6.

## 7.4 Magnetization in Fe Thin Films

In this section, the magnetization profile in thin films is considered. Atomic blocks of bcc Fe with (100), (110) and (111) surfaces are prepared by cutting from thermally equilibrated bulk samples. The sample sizes are all the same, about  $85\text{\AA} \times 85\text{\AA} \times 75\text{\AA}$ . Periodic boundary condition is applied on the  $x$  and  $y$  directions only. Along the  $z$  direction, there are in total 52, 36 and 90 layers for films with (100), (110) and (111) surfaces respectively, where the number of atoms in each lattice plane are 900, 1296 and 504. The surfaces are allowed to relax until the sample attains stress-free condition and the total energy attains equilibrium again. After that, the magnetic properties of these samples are examined layer-by-layer through the depth of the film.

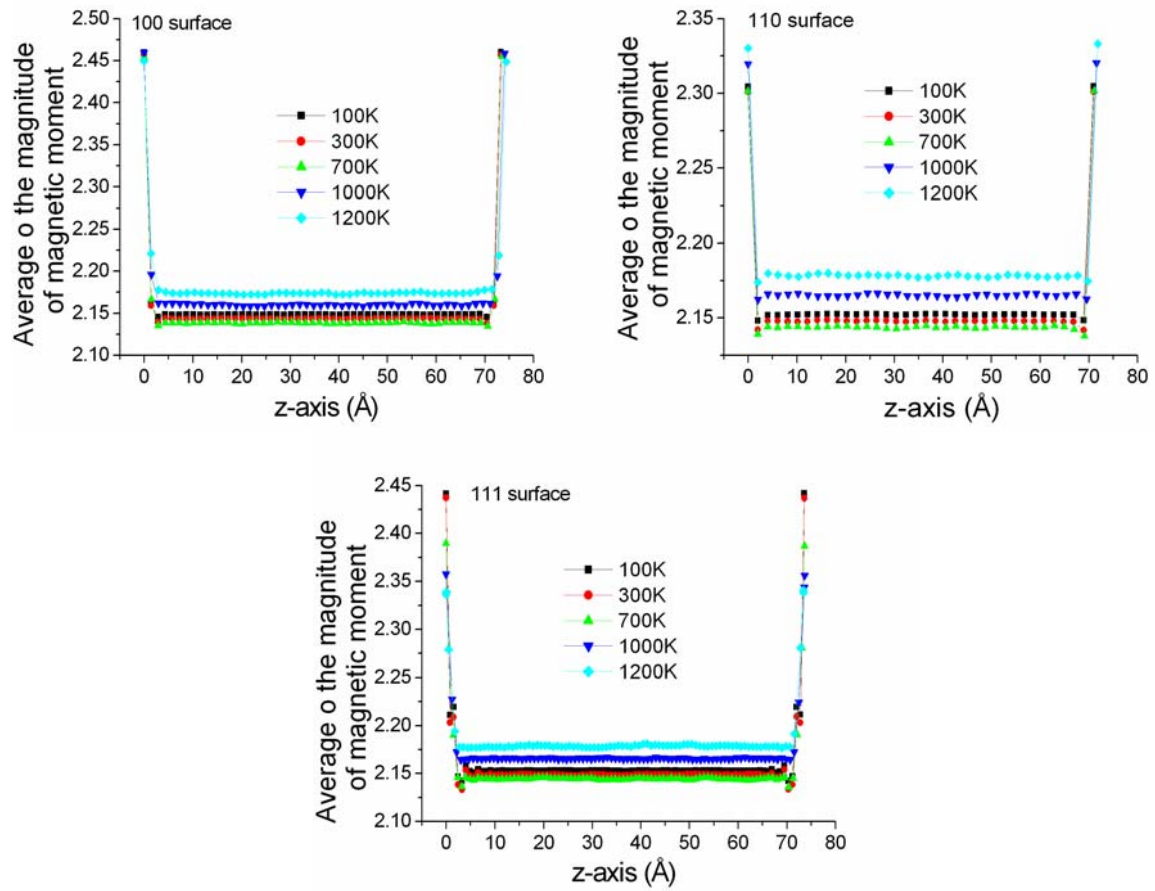


Figure 7.8 – The average of the magnitude of magnetic moment calculated layer-by-layer for various temperatures and for (100), (110) and (111) surfaces.

The average of the magnitudes of the atomic magnetic moments  $\langle m_i \rangle$  of each layer is calculated and plotted in Figure 7.8. It should be emphasized that this is different from the magnitude of the average magnetic moment which takes into account the direction of the magnetic moment of each atom. This value can also be obtained directly from the DD potential as in Ref. [8], in which the surface properties of Fe is investigated at 0K only. The current results agree well with the *ab-initio* [6],[7] and the magnetic potential results [8] that the  $m_i$  is enhanced for all three kinds of surfaces. It clearly predicts that even at high temperature its value

is still increased on the surface, which contradicts the experimental results [9]-[11].

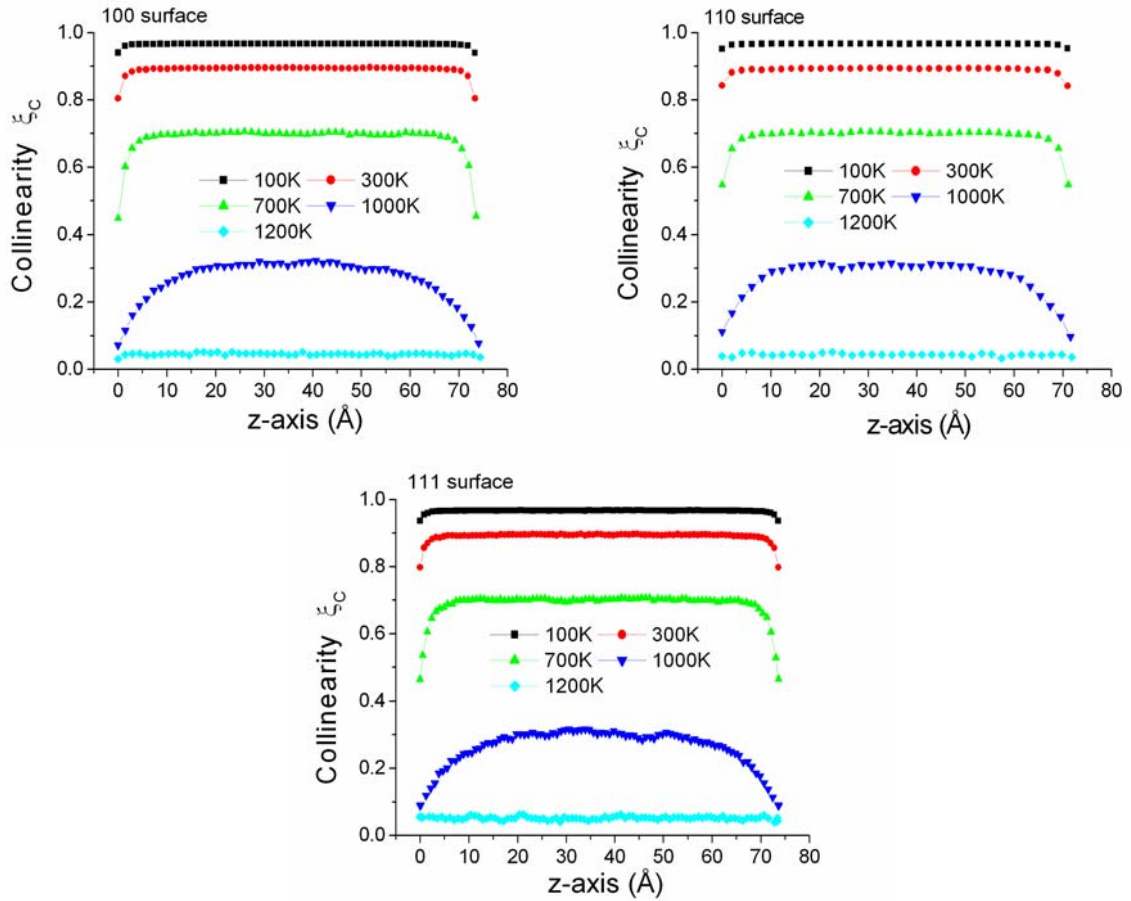


Figure 7.9 – The collinearity calculated layer-by-layer for various temperature and for (100), (110) and (111) surfaces.

The layer-by-layer collinearity  $\xi_C$  of the thin-film is shown in Figure 7.9 for different surface crystallography. In the middle of the film,  $\xi_C$  keeps the bulk value, but its value drops approaching the surface because of the decrease of neighboring atoms, thus weakening the effective field that maintains the spin order. As a result, the atomic spins on the surface becomes more disordered corresponding to a lower degree of collinearity and a smaller value of  $\xi_C$ .

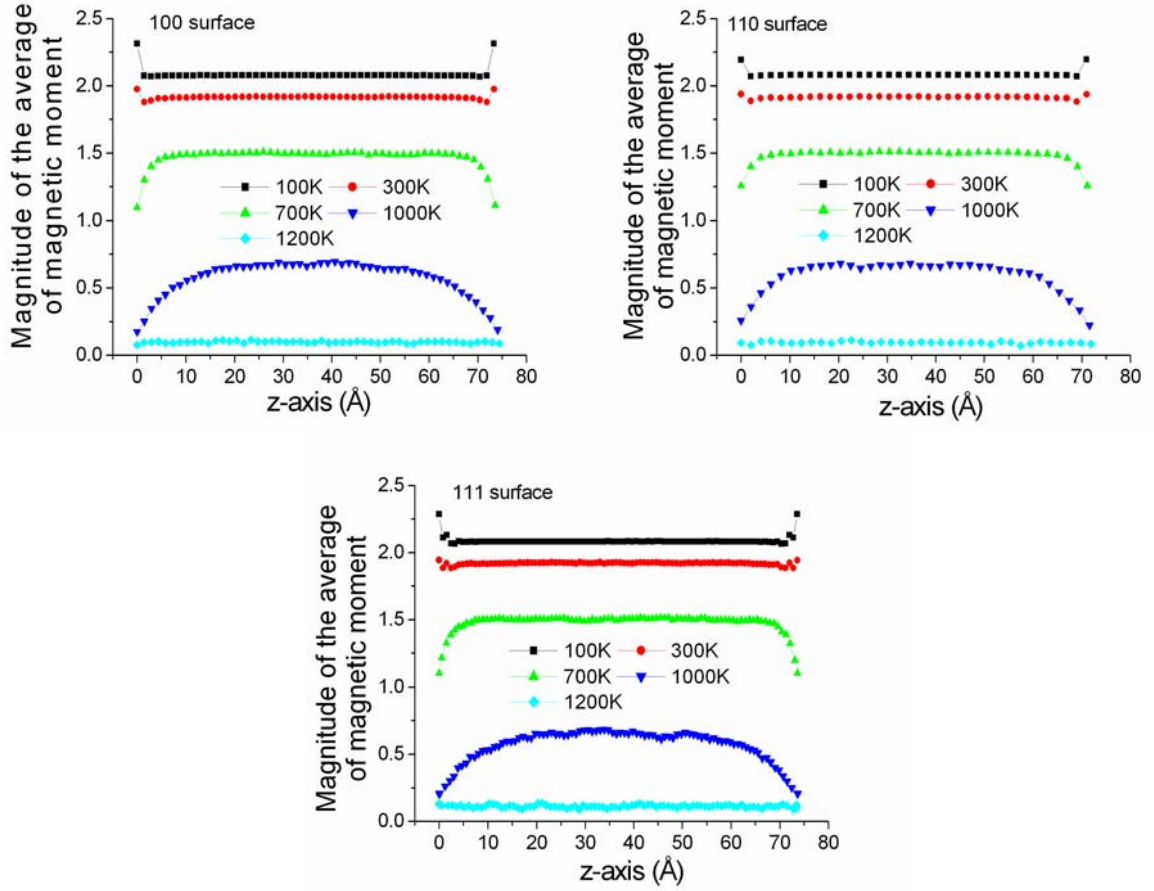


Figure 7.10 – The average of magnetic moment calculated layer-by-layer for various temperature and for (100), (110) and (111) surfaces.

Since the magnetic moment vector is given by  $\mathbf{M}_k = -m_k \mathbf{e}_k$ , its average is

governed by both  $\langle m_i \rangle$  and  $\xi_C$ , where the magnitude of the average of magnetic

moment of a layer  $|\langle \mathbf{M}_i \rangle| = \frac{1}{N_{n^{\text{th}} \text{ layer}}} \left| \sum_i (-m_i \mathbf{e}_i) \right| \approx \langle m_i \rangle \frac{1}{N_{n^{\text{th}} \text{ layer}}} \left| \sum_i \mathbf{e}_i \right| = \langle m_i \rangle \xi_C$ ,

providing that the  $m_i$  of all atoms in a layer are about the same. In Figure 7.10,

the  $|\langle \mathbf{M}_i \rangle|$  on the surface can be seen to increase at low temperatures and decrease

at higher temperatures as a result of the combined effects of  $\langle m_i \rangle$  and  $\xi_C$ . This

fits both the *ab-initio* result at 0K, where  $\xi_C = 1$ , and the experimental ones for

finite temperatures. We should note that the average magnetization  $|\langle \mathbf{M}_i \rangle|$  at the room temperature on all the surfaces in the current calculations shows enhancement, which is not in quantitative agreement with experiments [9]-[11]. Yet, the trend of decreasing magnetization on the surface from positive to negative as temperature increases is clear in the current work. At the same time, the mechanism responsible for this rather complicated behavior is also clearly established.

## 7.5 Magnetic Effects on Elastic Constants

In this section, magneto-mechanical effect is considered. The first property that can most easily be examined is the thermal expansion. The equilibrium zero pressure lattice constants at various temperatures can be obtained by taking the time average of the dimensions of the simulation box, after the system has attained equilibrium. Figure 7.11 compares the lattice constants calculated with and without spin-lattice coupling, plotted as a function of temperature. The results obtained without spin-lattice coupling is a conventional MD simulation with the DD potential [20].

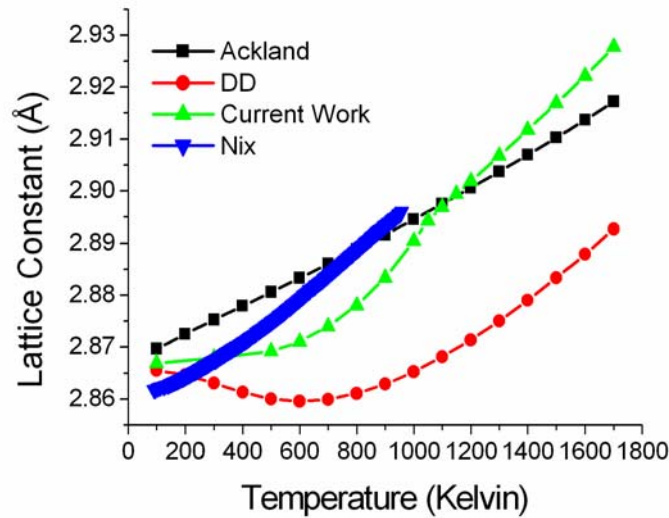


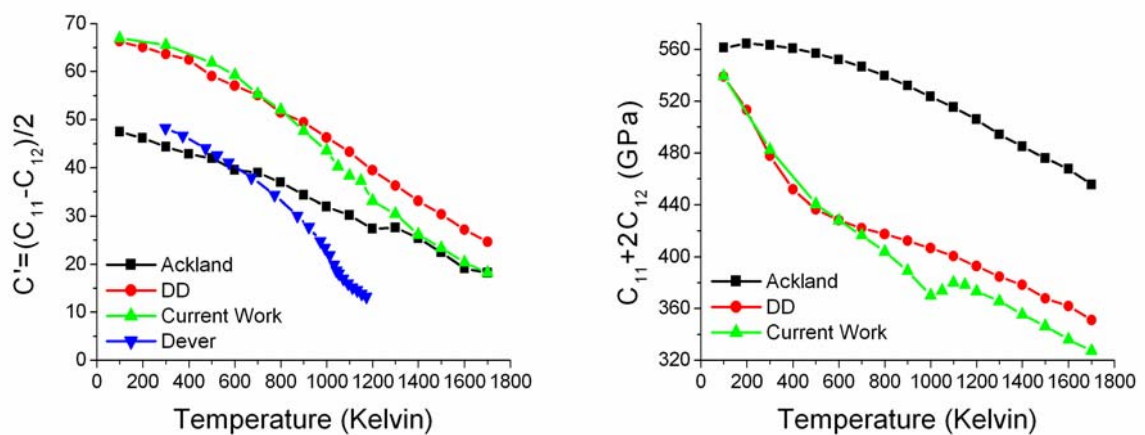
Figure 7.11 – Equilibrium zero pressure lattice constant of bcc iron evaluated using SLD simulations, conventional MD simulations performed for the Ackland potential [21], the magnetic DD potential [20], and experimental data taken from Nix and MacNair [22] shown for a range of temperatures.

The striking difference reflects the significant effect of spin-lattice coupling on the temperature-dependent equilibrium lattice constant, which is one of the most basic properties of the material. MD results using the Ackland potential [21] and the experimental results of Nix and MacNair [22] are also plotted for comparison. One can see that taking into account the spin-lattice coupling within the present scheme produces generally better agreement with observations, even though deviations from experimental values still exist. We should particularly note the inflection point of the predicted curve near  $T_c$ . This is evidently related to the spin part of the Hamiltonian and to the effect of spin-spin correlations on inter-atomic forces, a feature neither the DD nor Ackland potentials manage to produce. Comparing the values of lattice constant calculated with and without the spin-lattice interaction, one can conclude that the effect of the exchange interaction at a finite temperature favors the expansion of the lattice, a result one could have

guessed from the spatial dependence of the exchange function.

The elastic constants  $C' = (C_{11} - C_{12})/2$  and  $C_{11} + 2C_{12}$  are next calculated.

$C'$  is obtained by applying a very small uniaxial tensile stress on the simulation box along the  $z$  direction, letting the box to shrink in the  $x$  and  $y$  directions and thus allowing a tetragonal shear to occur.  $C_{11} + 2C_{12}$  is obtained by calculating the stresses in two samples, one given a small expansion and the other a small contraction. Then, it was calculated from the hydrostatic stresses and the volumetric strains.  $C_{11}$  and  $C_{12}$  are deduced algebraically. To obtain  $C_{44}$ , a pure shear strain is applied through progressive mismatching periodic boundary conditions. The calculated elastic constants are shown in Figure 7.12 as functions of temperature, with and without the spin degree of freedom. Results obtained using MD with Ackland potential, and experimental results by Dever [16] are also shown for comparison.



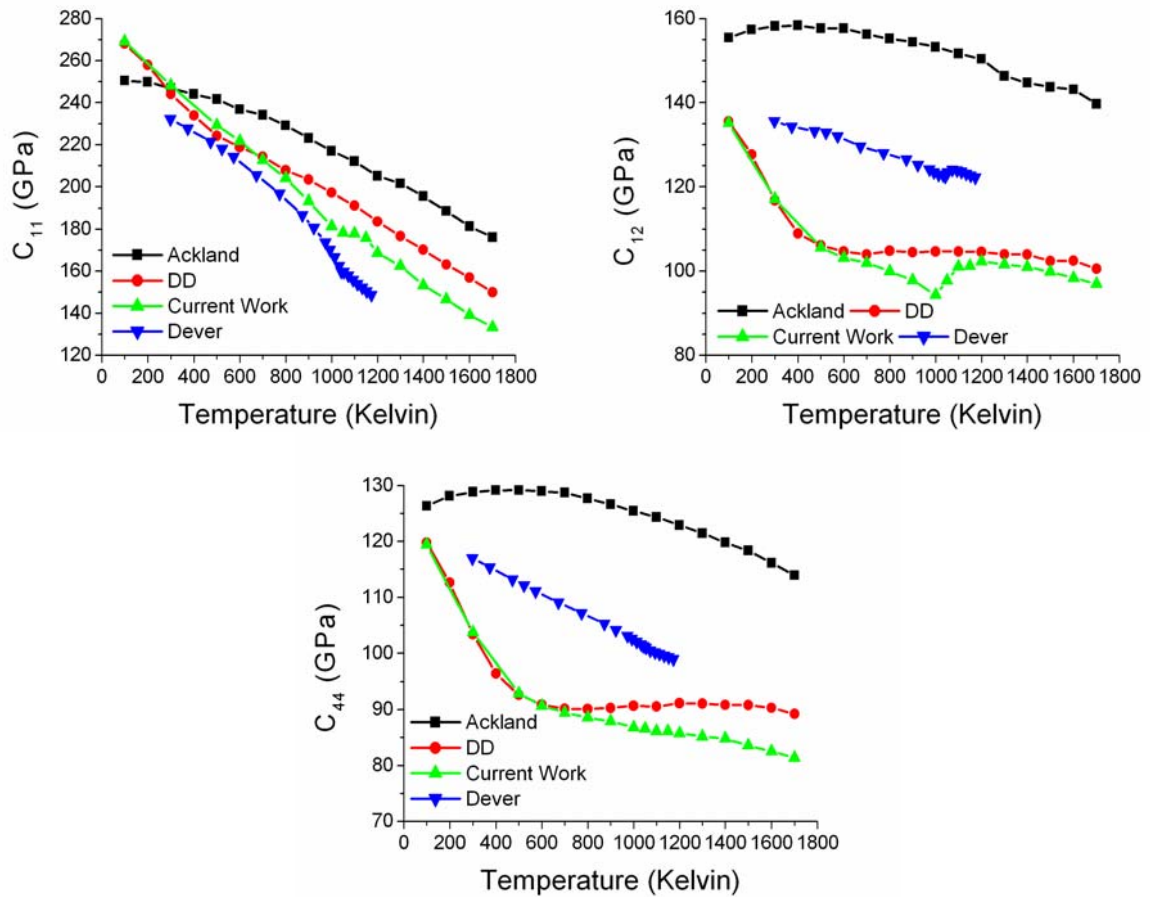


Figure 7.12 – Elastic constant of bcc iron evaluated using SLD simulations, conventional MD simulations performed for the Ackland potential [21], the magnetic DD potential [20], and experimental data taken from Dever [16] shown for a range of temperatures.

In general, the SLD results are close to the MD results using the DD potential at temperatures lower than about 600K. For higher temperatures, the effects of spin-lattice dynamics become important, causing increasingly bigger deviations between the MD and SLD results. An outstanding feature in this regard is the experimentally observed anomalous behavior near  $T_c$ , such as the characteristic cusp in  $C_{12}$ , which can only be discerned in the SLD results. Indeed, despite the lack of good supporting evidence, Dever [16] also speculated that such anomalous behavior might have their origin as a magnetic effect. In addition, although  $C'$

was not softened with temperature increase as suggested by Hasegawa [15], an inflexion point can nevertheless be discerned, in good agreement with the experiment curve. From the differences between the respective results from the DD potential, the Ackland potential and experiments, one would expect that the SLD can reproduce better results if the DD potential is fitted to the experimental elastic constants at low temperatures. Although the Ackland potential also did not manage to reproduce the elastic constants, its trend is closer to experiment, i.e., without the sharp drop at low temperatures of  $C_{12}$  and  $C_{44}$  calculated from the DD potential.

From the SLD results of lattice constant and elastic constant, one may conclude that the inter-atomic interactions at 0K can be approximated by a function that depends only on the lattice configuration. However, at finite temperatures, the correlated behavior of the spin subsystem in the form of spin waves becomes important to the collective properties of the solid. Phase stability of the lattice is maintained by the combined action of two fluctuating forces, one arising from the scalar inter-atomic potential, and the other from the gradient of the exchange function in the Heisenberg spin-spin Hamiltonian. The temperature dependence of the first contribution comes from the anharmonicity of scalar inter-atomic forces *via* phonon-phonon interactions, whereas the second part comes from the spin fluctuations *via* phonon-magnon interactions.

## 7.6 Brief Conclusion

The dynamics of thermalization under NPT conditions was investigated,

where the system exchanges energy and angular momentum with an external thermal reservoir. The temperature dependence of the average magnetization of bulk bcc Fe obtained from our SLD simulations agrees with experimental observations within the limits imposed by classical statistical mechanics. The thermalization time is the longest near the Curie temperature, which may be understood as due to the competition between the order and disorder states. For a bcc Fe thin film, the increase of magnetism at low temperature is found to be due to the enhancement of the magnitude of magnetic moment at the surface, while the decrease of magnetism at relatively high temperature is due to the reduction of the degree of collinearity  $\xi_C$ . The current results explain the apparent contradiction between the *ab-initio* calculation and experimental results.

The dynamics of the spin degrees of freedom is also found to affect equilibrium properties of the system, such as the thermal expansion coefficient and the elastic constants. Experimentally observed anomaly of the elastic constants near the transition temperature can only be reproduced in SLD simulations, and does not occur in MD simulations. Comparison with experiments and MD simulations illustrates the significance of including the spin degrees of freedom in dynamical simulations of magnetic materials. Although only a few applications have been performed for ferromagnetic iron, these examples not only show us the feasibility, but also allow us a glimpse into the power of the Langevin Spin-Lattice Dynamics (SLD) simulation scheme designed and reported in this thesis.

## REFERENCES

- [1] W. Hübner and G. P. Zhang, *Phys. Rev. B* **58**, R5920 (1998)
- [2] W. F. Brown Jr., *Phys. Rev.* **130**, 1677 (1963)
- [3] J. L. García-Palacios and F. J. Lázaro, *Phys. Rev. B*, **58** 14937 (1998)
- [4] S. Chandrasekhar, *Rev. Mod. Phys.*, **15**, 1 (1943)
- [5] R. Kubo, *Rep. Prog. Phys.*, **29**, 255 (1966)
- [6] O. Šipr and M. Košuth and H. Ebert, *Phys. Rev. B* **70**, 174423 (2004)
- [7] M. Chakraborty, A. Mookerjee and A. K. Bhattacharya, *J. Magn. Magn. Mater.* **295**, 210 (2005)
- [8] P. Van Zwol, P. M. Derlet, H. Van Swygenhoven and S. L. Dudarev, *Surf. Sci.* **601**, 3512 (2007)
- [9] L. N. Liebermann, D. R. Fredkin and H. B. Shore, *Phys. Re. Lett.* **22**, 539 (1969)
- [10] J. C. Walker, R. Droste, G. Stern and J. Tyson, *J. Appl. Phys.* **55**, 2500 (1984)
- [11] J. Tyson, A. H. Owens and J. C. Walker, *J. Appl. Phys.* **52**, 2487 (1981)
- [12] H. Hasegawa *J. Phys. F.: Met. Phys.* **17**, 165 (1987)
- [13] H. Hasegawa and D. G. Pettifor, *Phys. Rev. Lett.*, **50**, 130 (1983)
- [14] M. Friák, M. Šob and V. Vitek, *Phys. Rev. B*, **63**, 052495 (2001)
- [15] H. Hasegawa, M. W. Finnis and D. G. Pettifor, *J. Phys.: Met. Phys.*, **15**, 19 (1985)
- [16] D. J. Dever, *J. Phys. Phys.*, **43**, 3293 (1972)
- [17] J. Crangle and G. M. Goodman, *Proc. Royal Soc. London Ser. A, Math. Phys. Sci.*, **321**, 477 (1971)
- [18] J. Hubbard, *Phys. Rev. B*, **19**, 2626 (1979); J. Hubbard, *Phys. Rev B*, **11**, 4584

(1979)

[19] J. H. Van Vleck, *Rev. Mod. Phys.* **17**, 27 (1945)

[20] S. L. Dudarev and P. M. Derlet, *J. Phys.: Condens. Matter*, **17**, 7097 (2005)

[21] G. J. Ackland, D. J. Bacon, A. F. Calder and T. Harry, *Phil. Mag. A*, **75**, 713

(1997)

[22] F. C. Nix and D. MacNair, *Phys. Rev.*, **60**, 597 (1941)

## Chapter 8: Summary and Conclusion

Computer simulation of the Spin-Lattice Dynamics (SLD) for itinerant ferromagnets at finite temperatures is developed, in which each atom is considered as a classical particle with an intrinsic angular momentum and an associated magnetic moment. The set of SLD equations of motion, on which the simulation is based, is derived from a Hamiltonian expressed in terms of the magnetic interatomic potential and the Heisenberg spin-spin interaction with a coordinate-dependent pair-wise exchange function. The coupling between the dynamics of the spin and lattice subsystems is explicitly considered. Within the present scheme, simulations of both isolated and non-isolated systems can be performed. In the former case, constraints on the dynamics and energetics of the system due to the conservation of energy and angular momentum must be taken into account in the design of the simulation and the interpretation of the results. In the latter case, energy exchange between the reservoir and the spin subsystem is realized *via* the spin temperature, which is introduced *via* the fluctuation-dissipation theorem (FDT).

To control numerical errors accumulated over tens of millions of time steps during the integration of a set of highly coupled equations of motion is not a trivial task. In the present scheme, the integration is performed using the 2<sup>nd</sup> order Suzuki-Trotter decomposition (STD) scheme which, for a proper decomposition of the evolution operator, is symplectic. Its usage may avoid numerical energy dissipation, despite the trajectory and machine error. The SLD scheme, together

with the parallel algorithm, exhibits good stability as a simulation method. The numerical scheme has been tested for accuracy and is suitable for simulating systems containing many ( $\sim 10^6$ ) atoms over relatively long intervals of time ( $> 1$  ns). The computational resources required for the implementation of the algorithm are only twice those needed for conventional MD. In this regard, besides being able to include many-body effects due to the excitation of phonons and magnons and their interactions in the simulation, the present scheme is capable of simulating the dynamical behavior of systems. This capability is well beyond the reach of any electronic structure-based spin dynamics approach.

The scheme is firstly validated in the simulation of adiabatic relaxation of a periodic array of  $180^\circ$  domain-walls in ferromagnetic bcc iron. Magnons are initially created near the magnetic boundary. The relaxation of the domain boundary proceeds initially through the creation of magnons that almost immediately redistributes, destroying  $\sim 90\%$  the initial collinearity throughout the simulation region within a few tenths of a picosecond. Relaxation of the magnon system *via* magnon-magnon interaction (spin-spin relaxation) starts to re-establishes the collinearity quickly. Over 60% of the collinearity is recovered within about 1-2 ps. After that, spin-lattice interaction starts to become effective. The excitation of phonons that caused by the magnons helps re-establish the phonon-magnon equilibrium and produces further relaxation by energy transfer from the spin subsystem to the lattice subsystem, producing further recovery of the collinearity. Due to the mismatch between the timescales of evolution of the spin and lattice vibrations, the magnon-phonon coupling is relatively weak, resulting in a much longer total relaxation time with half-life  $\sim 0.25$  ns. The simulation scheme

is shown to enable the energy flow from spin to lattice subsystem or vice versa.

Applications to simulate the dynamics of thermalization under NPT conditions and the related effects have also been investigated. The average magnetization obtained from this simulation as a function of temperature agrees very well with the mean-field theory as well as experimental observations. The order/disorder ferro/paramagnetic transition is successfully reproduced. The thermalization time is the longest near the Curie temperature, which may be due to the competition between the order and disorder states.

For bcc Fe thin films, an increase of magnetism on the film surfaces at low temperature is due to the enhancement of the average of magnetic moment caused by the reduction of electron density on the surface. The decrease of magnetism at higher temperatures is due to the decrease of collinearity, which explains the contradiction between the *ab-initio* calculation and experimental results.

Simulations of magneto-mechanical effects are also performed. Equilibrium properties e.g. the thermal expansion coefficient and the elastic constants are found to be affected by the magnetization. Experimentally observed anomalies of the elastic constants near the transition temperature are reproduced in our SLD simulations, but not in the corresponding MD simulations. This illustrates the importance of including the spin degrees of freedom in dynamical simulations of magnetic materials.

In conclusion, a SLD simulation scheme for ferromagnetic iron has been designed and reported in this thesis, and its feasibility and applicability have been

shown. This scheme may be potentially useful as a basis for generalization to more extensive applicability. Several applications have been performed and the results are found to agree well with experimental results, illustrating the importance of including the spin degrees of freedom in dynamical simulations of magnetic materials.